Department of Chemical Engineering

Catalysis Institute

Novel empowered supports for iron-based Fischer- Tropsch in a power-to-liquids process

---

Oaitse Percy Ketlogetswe

BSc (Chemical Engineering), UCT

Supervisors:

Associate Professor Nico Fischer

Professor Michael Claeys

Key words: Fischer-Tropsch, iron-based catalyst, perovskites, lanthanum-based perovskites, slurry reactor, secondary *α*

Thesis submitted to the University of Cape Town in partial fulfilment of the academic requirement for the degree of **Master of Science in Chemical Engineering**

February 2023

“For I know the plans I have for you, declares the Lord, plans for peace and not for evil, to give you hope and a future.”

Jeremiah 29:11

Declaration

I, Oaitse Percy Ketlogetswe, know the meaning of plagiarism and declare that all the work in the document, save for that which is properly acknowledged, is my own. This thesis/dissertation has been submitted to the Turnitin module (or equivalent similarity and originality checking software) and I confirm that my supervisor has seen my report and any concerns revealed by such have been resolved with my supervisor.

Signed by candidate

Oaitse Percy Ketlogetswe 10/02/2023

Acknowledgements

First and foremost, I would like to express my deepest gratitude to my supervisors, Associate Professor Nico Fischer, and Professor Michael Claeys for giving me the opportunity to work on this project. My sincere appreciation goes to Associate Professor Nico Fischer for his unwavering support and guidance throughout this research. His expertise and valuable insights have been invaluable to me, and I am incredibly grateful for the opportunity to work with such a patient, knowledgeable and supportive mentor.

I would also like to thank DSI-NRF Centre of Excellence in Catalysis C*Change, The Catalysis Institute – University of Cape Town, for their financial support for this research. Without their financial support, this work would not have been possible.

I am grateful to my colleagues at the Catalysis Institute, Rachel Cupido, Chantal Le Roux, and Waldo Koorts at the Analytical Laboratory, Mohamed Jaffer and Miranda Waldron at the Electron Microscope Units for their support and assistance with data analysis. A big thank you to Dr Mohamed Fadlalla for his help and assistance with the laboratory experiments, and his availability and flexibility in working with my schedule. His selflessness, patience and expertise allowed me to learn a lot throughout this journey.

Thank you to my research group for their support both in and outside the laboratories, and for fostering a productive and enjoyable atmosphere that made me excited to go to the labs every day. Grateful to my seniors Dr Motlokoa Khasu, Dr Shaine Raseale and Dr Wijnand Marquart for assisting me with my laboratory experiments and analyzing the results. Their guidance and advice have been invaluable to me. To Kin de Kock, whom I began this journey together, thank you for the friendship and support throughout this journey, and I am grateful to have had such a supportive friend by my side. I would also like to thank Lindokuhle Ngema, whom I always worked with in the labs on weekends and early evenings, for their camaraderie and support.

Finally, I would like to thank my family and friends for their love and support during this process. My heartfelt gratitude to Lee Ngakaagae for his unwavering support and encouragement throughout this journey. I am especially grateful for Lee for holding me accountable and keeping me on track when I needed it most. His encouragement and belief in me were invaluable, and I cannot thank him enough for his friendship and support.

Synopsis

Fischer-Tropsch (FT) synthesis is a process that converts carbon monoxide and hydrogen into liquid hydrocarbons [1]. In the past, FT synthesis has been used to produce gasoline and diesel from coal and natural gas. However, with increasing demand for renewable and sustainable energy sources, there has been renewed interest in using FT to produce clean fuels [2]. The FT synthesis process takes place in the presence of a catalyst, at moderate temperatures and pressures. Iron-based catalysts are frequently used in commercial FT as they are quite useful in hydrogen lean synthesis gas because of their high water-gas shift activity. Nevertheless, these catalysts often need to be promoted to optimize their performance and they are prone to deactivation under FT conditions [3]. Promotion with potassium is often done to shift the FT performance and selectivities, while manganese and copper are often added to stir catalyst reduction [4].

Potassium is often used to modify iron-based catalysts to improve their performance. It has been suggested that potassium can impact the rate at which carbon is formed during FT by facilitating CO dissociation on the catalyst surface. Potassium also inhibits hydrogen chemisorption resulting in more carbon on the catalyst surface, longer chain products and higher olefin production [4,5]. The large ionic radius of potassium, however, has been reported to prevent its incorporation into iron oxide during synthesis, resulting in its mobility at the catalyst surface. The potassium mobility during FT results in enrichment of carbon on the catalyst surface and consequently catalyst deactivation [6]. In this study, we explored the possibility of using perovskites materials as support structures for the iron catalyst, and potassium incorporated within their structures. The perovskites allowed for better dispersion of the catalysts and improved control over the contact between the iron catalyst and potassium promoter. This in turn suppressed the movement of the promoter species, leading to improved catalytic performance.

Two lanthanum-based perovskites were examined: $LaAlO_{3-\delta}$ and $LaTiO_{3-\delta}$. The $LaAlO_{3-\delta}$ catalysts were modified by substituting potassium to the A site and substituting 20 atom-% manganese to the B site. A range of materials with varying amounts of potassium, $La_{1-x}K_xAl_{0.8}Mn_{0.2}O_{3-\delta}$, ($x$ = 0, 2, 4, 6, 8, 10 atom-%) were prepared via the citrate method [7]. The $LaTiO_{3-\delta}$ catalysts were only modified by substituting potassium on the A site. A series of potassium substituted $La_{1-x}K_xTiO_{3-\delta}$ perovskites (x = 0, 5, 10, 15, 20 and 30 atom-%) were prepared using a wet chemical technique [8]. Iron nanoparticles prepared using the co-precipitation method [9], were deposited onto these supports as catalyst for FT synthesis

process. The effect of potassium promotion on the properties and performance of these catalysts were evaluated. These catalysts were activated under H_2 flow at 80 ml/min at 450 °C for 15 hours. Fischer-Tropsch synthesis was conducted in a 600 ml continuously stirred reactor tank at 240 °C, 15 bar with synthesis gas ratio of 2 (H_2/CO = 2) and a space velocity of 2.4L/(h.$g_{catalyst}$). The catalysts performance was evaluated over a 48-hour period using online GC-TCD and offline GC-FID.

In this study, the Fe-$La_{1-x}K_xAl_{0.8}Mn_{0.2}O_{3-\delta}$ catalysts with potassium promotion showed higher catalytic activity than the unpromoted catalyst. The activity of the catalysts increased with increasing potassium loading until a maximum was reached at 8 atom-% potassium loading. The higher activity of the potassium promoted catalysts was attributed to the enhanced formation of iron carbide phases, which have been shown to be active in FT synthesis. Potassium promotion also led to lower methane selectivity, which was not dependent on the amount of potassium added. The results were ascribed to the water-gas shift activity of the iron catalyst. There was also a decrease in selectivity of C_2 – C_4 hydrocarbons and increased selectivity of C_{5+} hydrocarbons, while reducing the selectivity of oxygenates.

Potassium promotion on the Fe-$La_{1-x}K_xTiO_{3-\delta}$ catalysts resulted in structural change from orthorhombic at low potassium promotion to cubic structures at higher potassium promotion. The *in situ* XRD results revealed that potassium results in reduced onset reduction temperature from Fe_3O_4 to wüstite (FeO) and retards the reduction process from the FeO to metallic Fe. Nonetheless, it enhanced the initial formation of carbides through its influence on CO and H_2 chemisorption. There was improved catalytic activity of the catalysts until a maximum at 10 atom-% potassium loading. On the other hand, this promotion led to a decrease in methane selectivity over time. The water-gas shift activity was higher on the promoted catalysts with no clear trend on the effect of amount of potassium added. Furthermore, potassium promotion resulted in a decrease in the selectivity of C_2 – C_4 hydrocarbons, slight increase in C_{5+} hydrocarbons selectivity and little impact on the productivity of the oxygenates.

These developed catalysts had shown stability under FT reaction conditions as there was no observed structural change after FT synthesis. Due to their demonstrated stability at higher temperatures, these materials may be suitable for use in other catalytic processes such as reverse water-gas-shift reaction. Additionally, the lanthanum titanate perovskites could be promoted with manganese to investigate their reducibility and potentially improve their performance.

Table of Contents

List of figures

List of tables

Nomenclature

Abbreviations

ASF	Anderson-Schulz-Flory
BET	Brunauer-Emmett-Teller
BTL	Biomass-to-liquids
CFB	Circulating fluidized bed
CNT	Carbon nanotubes
CTL	Coal-to-liquids
FFB	Fixed fluidized bed
FT	Fischer-Tropsch
GC-FID	Gas chromatography flame ionization detector
GC-TCD	Gas chromatography thermal conductivity detector
GTL	Gas-to-liquid
HAADF	High-angle annular dark-field
HTFT	Hight temperature Fischer-Tropsch
ICP-OES	Inductively Coupled Plasma-Optical Emission Spectroscopy
LTFT	Low temperature Fischer-Tropsch
MTFT	Middle temperature Fischer-Tropsch
O/P	Olefins to paraffins ratio
PtX	Power-to-X
SBR	Slurry bed reactor
SEM-EDS	Scanning electron microscopy – energy dispersive spectroscopy
TEM	Transmission electron microscopy
TFBR	Tubular fixed bed reactor
TOS	Time on stream
WGS	Water gas shift
XRD	X-ray diffraction

Notations

α	Chain growth probability
A_i	Response area of component I in chromatogram
Å	Ångstrom
$C_2 - C_4$	Selectivity of hydrocarbons with a chain length $2 \leq n \leq 4$
C_{5+}	Selectivity of hydrocarbons with a chain length $n \geq 5$
f	Response factor
KI	Kovats Index
n_i	Molar flow rate of component i
$S_{i,C}$	Selectivity of component i
Xi,c	Conversion of component i
$Y_{i,C}$	Yield of component i

Chemicals

$(CH_2OH)_2$	Ethylene glycol
Al	Aluminium
$Al(NO_3)_3 \cdot 9H_2O$	Aluminium nitrate nonahydrate
Al_2O_3	Aluminium oxide
Ar	Argon
C	Carbon
$C_{12}H_{28}O_4Ti$	Titanium (IV) isopropoxide
$C_6H_8O_7.H_2O$	Citric acid
CH_3	Alkyl group
CH_4	Methane
CO	Carbon monoxide
Co	Cobalt
CO_2	Carbon dioxide
Cu	Copper
DME	Dimethyl ether
$Fe(NO_3)_3.9H_2O$	Iron (III) nitrate nonahydrate
Fe_3O_4	Magnetite
$FeCl_2.4H_2O$	Iron (II) chloride tetrahydrate
Fe_xC	Iron carbide
H_2	Hydrogen
H_2SO_4	Sulphuric acid
H_3BO_3	Boric acid
HCl	Hydrochloric acid
HF	Hydrofluoric acid
HNO_3	Nitric acid
K	Potassium
KNO_3	Potassium nitrate
$La(NO_3)_3.6H_2O$	Lanthanum nitrate hexahydrate
MgO	Magnesium oxide
Mn	Manganese
$Mn(NO_3)_2 \cdot 4H_2O$	Manganese (II) nitrate tetrahydrate
N_2	Nitrogen
Na	Sodium
$NaOH$	Sodium hydroxide
Ni	Nickel
Ru	Ruthenium
SiO_2	Silica
TiO_2	Titania
$\alpha\text{-}Fe$	Metallic iron
$\alpha\text{-}Fe_2O_3$	Hematite
$\gamma\text{-}Fe_2O_3$	Maghemite
$\varepsilon\text{-}Fe_xC$	Epsilon iron carbides
$\theta\text{-}Fe_3C$	Cementite
$\chi\text{-}Fe_5C_2$	Hägg carbide

CHAPTER 1: INTRODUCTION

Amid the need for economic growth, Africa faces key challenges pertaining to the lack of expertise and infrastructure development. These challenges are intensified by the fact that African economies continue to be heavily natural resource based. With its economy expected to quadruple in size and a near doubling of the population by 2040, the energy demand of this region is expected to increase by approximately 80 % [10]. Despite the continued urbanization, about 50 % of the population is predicted to inhabit rural environments. Lack of development in these areas coupled with insufficient infrastructure exacerbates the challenge of supplying electricity using conventional large-scale fossil fuel-based technologies given the potential harsh impacts of climate change due to greenhouse gas emissions [11].

Renewable energy sources can significantly reduce the over-reliance on the finite and environmentally unfriendly coal resources in South Africa. Furthermore, the development of the renewable energy sector in the country has the potential to create new job opportunities, thus improving the South African economy. Due to the geographical location and human capital of South Africa, several renewable energy sources such as solar and wind have significant potential in the country. However, renewable energy sources would need to be connected to storage devices, either through batteries or by converting the energy into chemical form using energy carriers like hydrogen (H_2), ammonia, methanol, or fuel. Without a well-developed distribution network, the need for energy conversion for storage is even greater.

While countries in the global north, like Germany, can reach their targets from reducing emissions and shifting away from fossil fuels independently, the energy sector's major transformation will lead to a new global trade in renewable energy [12]. This presents a significant opportunity for countries with substantial renewable energy potential, such as South Africa, Australia, and Chile. Amongst these, South Africa possesses several key advantages. While there are various pathways for producing "Power-to-X" (PtX), with X standing for different energy carriers such as gases (PtG: hydrogen, synthetic natural gas) or liquids (PtL: methanol or liquid hydrocarbons), all these pathways require the production of green hydrogen through water electrolysis, photocatalytic or thermal water splitting [12]. In the South African context, the PtL concept is the best option to store the excess renewable energy in the form of liquid fuels that can be used for transportation or industrial purposes. This could help

address the temporal and spatial mismatch between the availability of renewable energy and demand for it.

The PtL concept is based on the conversion of renewable energy to liquid fuels and chemicals such as dimethyl ether (DME), methanol, and Fischer-Tropsch (FT) synthesis products [13]. Amongst these, the FT synthesis route is generally considered the best drop in solution for the existing South African infrastructure, especially for long-haul transportation and aviation fuels, due to the superior volumetric and gravimetric energy density of hydrocarbons [14]. With more than 70 years of experience with FT synthesis technology, it is likely that South African developments in this field will be based on the FT rather than the methanol pathway.

While the traditional FT process converts CO and H_2 from fossil sources into hydrocarbons, in the PtL envelope, an FT synthesis process would need to convert carbon dioxide (CO_2) (initially from point sources, later potentially from direct air capture) and renewable H_2 into fuels. CO_2 can be activated through the thermodynamically limited reverse water-gas-shift (RWGS) reaction to produce CO and water over a catalyst (Figure 1.1) [15].

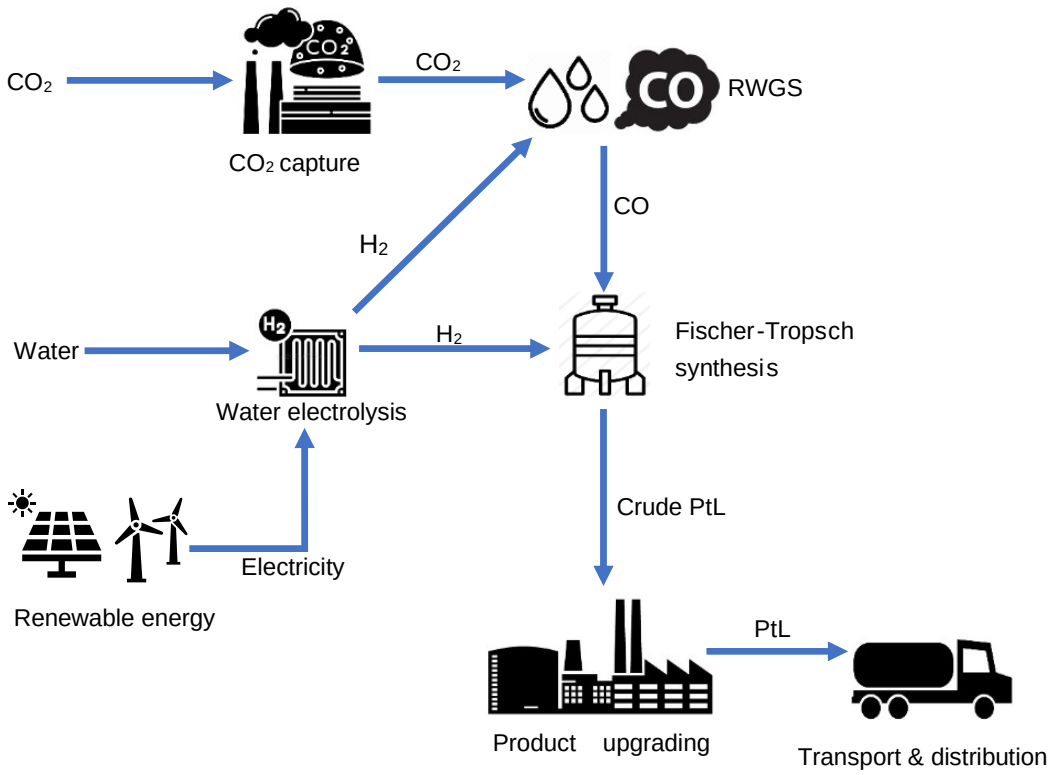

Figure 1. 1: Schematic PtL process via the Fischer-Tropsch pathway.

The main challenge in transforming the FT process from a large-scale consumer of H_2 and CO to small, distributed plants that convert green H_2 and CO, mostly relate to the complexity of the process and the stability of the currently available industrial catalysts based on iron and cobalt. Amongst FT catalysts, iron-based catalysts are particularly advantageous when H_2 lean syngas is used (ratio of H_2/CO is less than 2) due to their potential activity for WGS reactions. However, the challenge for the commercially existing iron-based FT catalysts is the stability of the active phases under high FT conversion conditions (elevated temperatures and pressures). Under these conditions, the metallic *α* iron phase is unstable and transforms into a metastable mixture of oxides and carbides resulting in rapid catalyst deactivation and requiring additional catalyst input [3,16]. As such, these catalysts are often promoted to improve catalyst reduction, stability, and catalyst activity. Potassium (K), sodium (Na), manganese (Mn) and copper (Cu) are commonly used as promoters. The presence of these materials stirs catalyst reduction/formation and performance by increasing the adsorption energy of CO and weakening the strength of the C-O bond, helping disperse and reduce the iron species within the catalysts, consequently leading to improved catalytic activity [17].

Potassium promotion is thought to make it easier for carbon to form on the catalyst surface and react with hydrogen forming the CH_2- monomer for hydrocarbon chain growth or supporting the conversion into iron carbide [18]. Figure 1.2 below presents a proposed mechanism explaining the role of alkali as promoter in FT synthesis on iron.

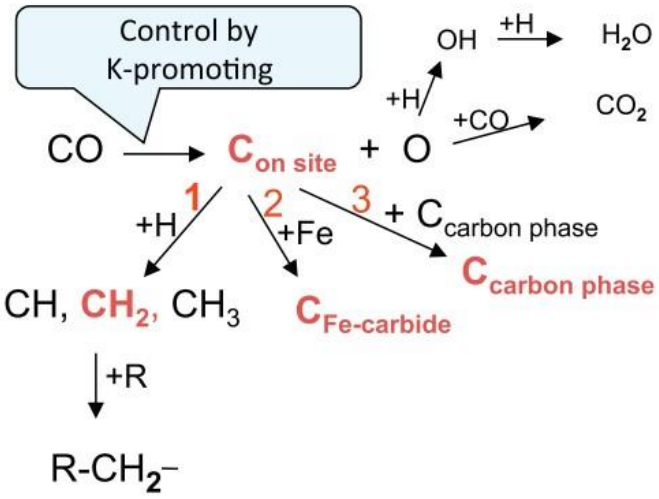

Figure 1. 2: Proposed mechanism of alkali promotion in Fischer-Tropsch synthesis on iron catalysts [18].

If there is too much K present, the carbon formation rate becomes too fast, and a carbon phase is formed. This can lead to carbon accumulation on the catalyst, which eventually leads

to active sites blockage, and consequently catalyst deactivation [18]. Therefore, promoters usually have an optimum concentration above which an increase in concentration is detrimental to the catalyst performance [19].

Furthermore, potassium is often considered a facilitator of electron transfer. Its large ionic radius hinders its incorporation into magnetite during synthesis. This property allows them to be mobile on the surface of the surface of the catalysts under reaction conditions [6]. The large ionic radius of potassium has been proposed to prevent its incorporation into iron oxides during synthesis, resulting in its localization at the catalyst surface. In the present study, the possibility of developing novel support structures based on perovskites materials that can provide the necessary classical support properties while also providing promoting capabilities was explored.

The use of perovskites potentially opens new promoter concentration windows previously unattainable whilst suppressing mobility and associated loss of active surface area even under harsh reaction conditions. Perovskites are not commonly used as catalysts supports in thermocatalytic processes due to their generally low surface area. However, our laboratory [20] successfully synthesized perovskites incorporating the promoting elements, Mn and K, within their structures to fulfil the classical support functionality together with promoting functionalities. The iron active phase was deposited on the catalyst surface. These structures not only provided the necessary support for enhanced dispersion of the catalyst, but also allowed for a better control of Fe/promoter contact and suppressed movement of the promoter species.

The study presented herein investigated lanthanum-based perovskite structures that stabilize the active iron phase and inhibit sintering through physical separation, while providing the promoting functionality using Mn and K within its structure. The effect of K promotion at constant Mn loading on lanthanum aluminates, and the effect of K promotion on lanthanum titanate iron-based catalysts was investigated. Thorough characterization of the synthesized materials was carried out using the various analytical techniques like powder X-ray diffraction (XRD), transmission electron microscopy (TEM),Inductively Coupled Plasma Optical Emission Spectroscopy (ICP-OES) and surface area measurements via N_2 adsorption.

CHAPTER 2: LITERATURE REVIEW

2.1 Fischer-Tropsch Synthesis

The Fischer-Tropsch (FT) synthesis is a chemical reaction that converts carbon monoxide (CO) and hydrogen (H_2) into liquid hydrocarbons. It was first discovered in the early 1920s by German chemists Franz Fischer and Hans Tropsch [1]. They were looking for ways to make synthetic fuels from coal to replace diminishing oil reserves. This process was later developed and used extensively in Germany during World War II to produce military fuel [21,22]. After World War II, the FT process was largely abandoned in favour of more traditional methods of producing fuels, such as refining oil. However, interest in the process was revived in the 1970s when oil prices rose dramatically and there was a renewed economic pressure to find alternative ways to produce fuels. In the 1950s, the Fischer-Tropsch process was developed and used extensively in South Africa to produce transportation fuels from coal [2]. The abundance of coal reserves and limited access to oil made FT process an attractive option in fuel production. Today, South Africa is home to one of the world's largest commercial scale Fischer-Tropsch plants, which produces over 150 000 barrels of oil per day [23].

FT synthesis is a technology historically known to produce gasoline and diesel from coal and natural gas. Today, because of the increased world population, there has been a high demand for renewable and sustainable energy resources instead of fossil fuels [2]. Still the FT synthesis can play a significant role. Apart from coal (coal-to-liquid, CTL process) and natural gas (gas-to-liquid, GTL process), it can be used to produce a wide range of hydrocarbons from for example biomass (biomass-to-liquid, BTL process) [24].

2.1.1 Chemical reactions in the Fischer-Tropsch synthesis

The FT synthesis converts synthesis gas (H_2 and CO) into a range of hydrocarbons, like gasoline, diesel, waxes, and oxygenates. The reaction occurs in the presence of a catalysts, typically a metal, at moderate temperatures and pressures [2]. The hydrocarbon production from synthesis gas is exothermic. Heat release increases with increasing chain length and hence heat removal is an important factor in the process. During the FT reaction, more than one reaction is facilitated on the catalyst surface [25]. Once upgraded, the formed hydrocarbons can be used to make high-quality fuels, lubricants, waxes and chemicals [19].

The FT synthesis product spectrum consists of a complex multicomponent mixture of linear and branched hydrocarbons and oxygenated products [25]. The main products of the Fischer-Tropsch synthesis, *α*-olefins and linear paraffins, are given by:

n-paraffins:

$$(2\mathrm{n} + 1)H_2 + \mathrm{n}CO \longrightarrow C_nH_{2n+2} + \mathrm{n}H_2O \qquad \textit{Equation 2. 1}$$

n-olefins:

$$2\mathrm{n}H_2 + \mathrm{n}CO \longrightarrow C_nH_{2n} + \mathrm{n}H_2O \qquad \textit{Equation 2. 2}$$

Where *n* is an integer. For paraffins, when *n* = 1, the reaction represents the production of methane, which is considered an undesired by-product in most FT applications. To control its formation, operating conditions are usually selected to maximize the formation of higher molecular weight hydrocarbons, which are high-value products [25].

The other important reaction that occurs in the FT process is the water gas shift (WGS) reaction which produces water and carbon dioxide (CO_2).This reaction plays a significant role especially in the iron-based FT synthesis [25]. The H_2O produced in the formation of olefins and paraffins (Equation 2.1 and 2.2) is converted into H_2 in the WGS reaction (Equation 2.3). This allows for hydrogen lean synthesis gas mixtures, such as the ones obtained from coal gasification, to be used directly as the H_2/CO ratio is increased on the catalyst surface.

$$H_2\mathrm{O} + CO \longleftrightarrow CO_2 + H_2 \qquad \textit{Equation 2. 3}$$

The FT process also involves some further side reactions. Apart from formation of olefins and paraffins, the chemical reaction between CO and H_2 can also result in the formation of alcohols, aldehydes, ketones and acids (Equation 2.4) [26].

$$2nH_2 + nCO \longrightarrow C_nH_{2n+2}\mathrm{O} + (n-1)H_2O \qquad \textit{Equation 2. 4}$$

The Boudouard reaction (Equation 2.5) competes with the main reactions for catalytically active sites, to produce carbonaceous deposits, which can block the active sites and eventually lead to catalyst deactivation (see Section 2.2.4) [26].

$$2CO \longrightarrow CO_2 + C \qquad \text{Equation 2. 5}$$

Beside Boudouard reaction, during the FT reaction and/or during catalyst activation, further conversions can occur on the catalytically active sites. These reactions tend to modify the catalyst [27]. During catalyst reduction, if H_2 or synthesis gas are used as the activating gas, the metal oxide reacts with the H_2 from synthesis gas forming H_2O and its metallic phase (Equation 2.6a). On the other hand, if CO is used for catalyst activation, the metal oxide reacts with the CO to form CO_2 and the metallic phase (Equation 2.6b). Furthermore, during catalyst activation with synthesis gas or CO, and during FT, the metal oxide phase transitions into the metallic phase and carbides (Equation 2.7) (See Section 2.2.3).

Catalyst reduction:

$$a)\ M_xO_y + yH_2 \longleftrightarrow yH_2O + xM \qquad \text{Equation 2. 6}$$

$$b)\ M_xO_y + yCO \longleftrightarrow yCO_2 + xM$$

Bulk carbide formation

$$yC + xM \longleftrightarrow M_xC_y \qquad \text{Equation 2. 7}$$

2.1.2 Reaction mechanisms in the Fischer-Tropsch synthesis

The Fischer-Tropsch synthesis can be described as a process that uses H_2 and CO to create hydrocarbon molecules, specifically aliphatic molecules which are made up of chains of carbon atoms. These hydrocarbons are produced *in situ* in a stepwise polymerization like reaction [28,29]. Since the introduction of the FT process, researchers have proposed several mechanisms to explain the formation of hydrocarbons on the surface of the catalyst. Owing to the complexity and wide range of carbon numbers of FT products, they have not reached a general agreement on the mechanism [28–32]. However, as summarized by Claeys and van Steen [33], all reaction pathways proposed in literature will have the following distinct reaction steps:

i. Generation of the chain initiator
ii. Chain growth or propagation
iii. Chain growth termination or desorption

It is generally believed that during the FT synthesis, several parallel reaction pathways exist on the catalyst surface. Numerous pathways have been proposed for the FT synthesis mechanisms to explain the product distribution. However, the four most popular mechanisms are the **alkyl, alkenyl, enol,** and **CO-insertion** mechanisms, (Figure 2.1) [33].

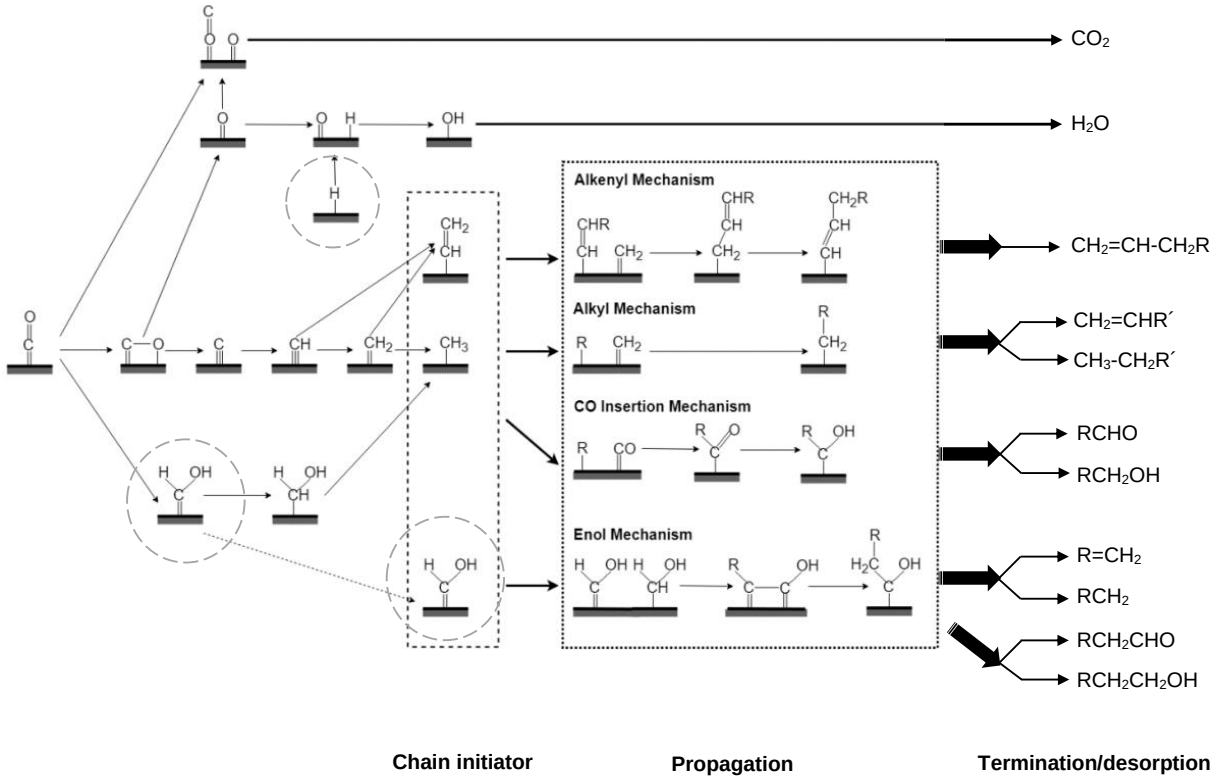

Figure 2. 1: Overview of Fischer-Tropsch mechanisms [34].

Alkyl mechanism

The alkyl mechanism involves the formation of alkyl intermediates on the surface of the catalyst [33]. In this mechanism, chain initiation takes place via dissociative CO chemisorption and surface C and O species are generated. Surface oxygen is removed from the catalyst via reaction with the adsorbed hydrogen producing H_2O, or with adsorbed CO to produce CO_2. Surface C is subsequently hydrogenated producing, in a consecutive reaction, methylidyne (CH), methylene (CH_2) and methyl (CH_3) surface species. The chain initiator in this mechanism is the formed CH_3 surface species, and the CH_2 surface species is the monomer. It is assumed that chain growth takes place by successive incorporation of the monomer. As described in the work of Claeys and van Steen [33], product formation takes place by either the removal of *β*-hydrogen or hydrogen addition to form longer hydrocarbon chains such as alkanes and

alkenes. This can occur through a variety of mechanisms, including oligomerization of alkyl intermediates and insertion of alkyl intermediates into growing hydrocarbon chains.

Alkenyl mechanism

Maitlis and colleagues proposed a pathway for the formation of olefins in the Fischer-Tropsch synthesis [35]. The activation of CO and its transformation into CH_x surface species is the same as in the alkyl mechanism. However, the first C-C bond is formed by the coupling of CH and CH_2 to form a vinyl surface species ($CH=CH_2$), which serves as the starting point for the chain. Chain propagation in this process involves adding a CH_2 species to a surface alkenyl species (vinyl species, CH=CHR) to produce a surface allyl species ($CH_2CH=CHR$). This is followed by an allyl-vinyl isomerization to form an alkenyl species ($CH=CHCH_2R$). Product desorption occurs through the addition of hydrogen to an alkenyl species, resulting in the production of alpha-olefins (Figure 2.1).

Enol mechanism

Proposed by Anderson et al. [36], the enol mechanism predicts that chemisorbed CO is hydrogenated to form an enol (oxygen containing) surface species. Chain growth occurs by condensation reactions between enol species with elimination of H_2O. The formation of branched hydrocarbons is thought to involve CHROH surface species. Termination of the chain growth process or desorption of the products produces oxygenates (aldehydes and alcohols) and α-olefins. As per this this mechanism, n-paraffins are formed in a secondary reaction from the hydrogenation of primary olefins. A different reaction pathway is required for the primary formation of n-paraffins. It has been suggested that acid formation in the Fischer-Tropsch synthesis is a secondary reaction of primary aldehydes via the Cannizzaro reaction, with acids reacting with alcohols giving esters [36].

CO-insertion mechanism

The CO-insertion mechanism was originally proposed by Sternberg and Wender [37] and further developed by Pichler and Schulz [38]. In this mechanism, chemisorbed CO serves as the monomer, and the chain initiator is thought to be a surface methyl species. The pathway

leading to the formation of the surface methyl species differs from the alkyl mechanism at the point of oxygen elimination from the surface species. Chain growth occurs through the CO-insertion into a metal-alkyl bond, resulting in the formation of a surface acyl species. This reaction step is well-known in homogeneous catalysis [39]. Oxygen is eliminated from the surface species to form an enlarged alkyl species. There are several proposed pathways for product desorption. The steps leading to the formation of n-paraffins, and α-olefins are the same as those proposed in the alkyl mechanism, involving hydrogen addition and β-hydrogen elimination. Chain termination reactions may also involve oxygen-containing surface species, resulting in the formation of aldehydes and alcohols. Aldehyde formation can occur through hydrogen addition to an acyl species or through β-hydrogen elimination of an RCHOH species, which quickly isomerizes to an aldehyde in the absence of a catalyst. Alcohol formation can take place through hydrogen addition to an RCHOH surface species, and ketones can be formed through the addition of a surface alky group to an acyl species. The CO-insertion mechanism is widely considered to be the main pathway for the formation of oxygenates [33].

2.1.3 Product distribution and selectivity

Regardless of the catalyst used, the four primary classifications of FT hydrocarbon products are n-olefins, n-paraffins, *trans*-2-olefins, and *cis*-2-olefins [29]. A minor fraction of the FT distribution is made up of oxygenates (alcohols, aldehydes, acids, and ketones), which according to the enol mechanism, are formed via termination of a chain containing an O atom. Figure 2.2 below illustrates a typical FT product spectrum for iron-based catalysts.

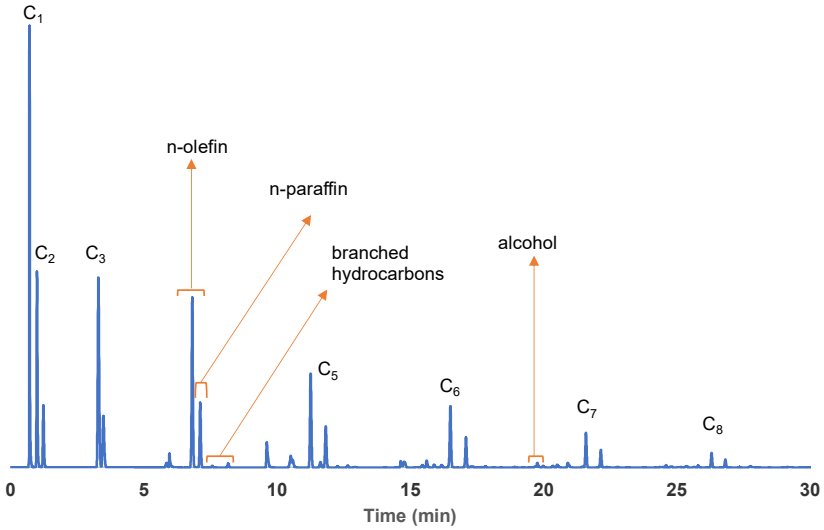

Figure 2. 2: FT product spectrum obtained using off-line FID analysis, for iron-based catalyst.

The Anderson-Schulz-Flory (ASF) distribution, which is often used to explain the formation of FT products, suggests that the products formed follow a process where C_1 units are added one after another to a growing chain on the catalyst surface [40]. The molar amount of the sums of products with the same carbon number decreases exponentially with C number [33]. This behaviour is indicative of a polymerization reaction that proceeds via stepwise addition of a C_1 monomer. A simplified growth scheme of this polymerization on the catalyst surface is given in Figure 2.3 below, assuming the formation of only one product class [33].

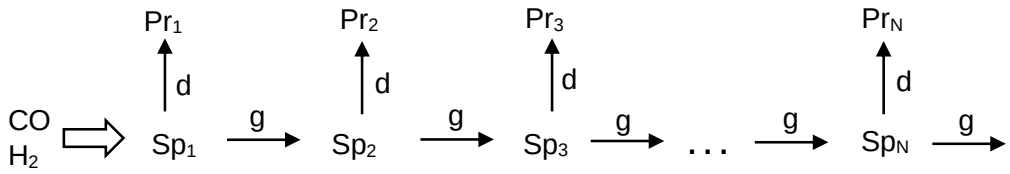

Figure 2. 3: Ideal chain growth assuming formation of one product class [33].

Under this growth scheme, CO and H_2 are adsorbed onto the catalyst surface. When they dissociate, they form monomers and chain starters (C_1 surface species, Sp_1). These monomers and chain starters can either desorb (d), forming the C_1 product molecule (Pr_1) or grow (g) via combination with other monomers to create a longer chain [33].

The actual product distribution from FT reactions often differs from the ideal distribution based on ASF model. Compared to the growth process in Figure 2.3, the FT product distribution include several compounds such as paraffins, olefins and oxygenates that are often studied separately as they exhibit different behaviour when they are desorbed from the catalyst surface. For instance, it is widely reported that primary α-olefins that are formed can re-adsorb on the catalyst surface based on their carbon number [41,42], and result in the formation of secondary products through chain growth, hydrogenation, or double bond shift. Similarly, the primarily formed oxygenates (mainly 1-alcohols and aldehydes) can also re-adsorb and undergo further reaction [43–45]. By incorporating these reactions and their dependency on chain length (see Figure 2.4) into the proposed chain growth mechanism (noting that the model does not consider the formation of branched hydrocarbons or the possibility of different surface species and active sites), the model can explain some of the deviations from the ideal ASF distribution observed in experiments.

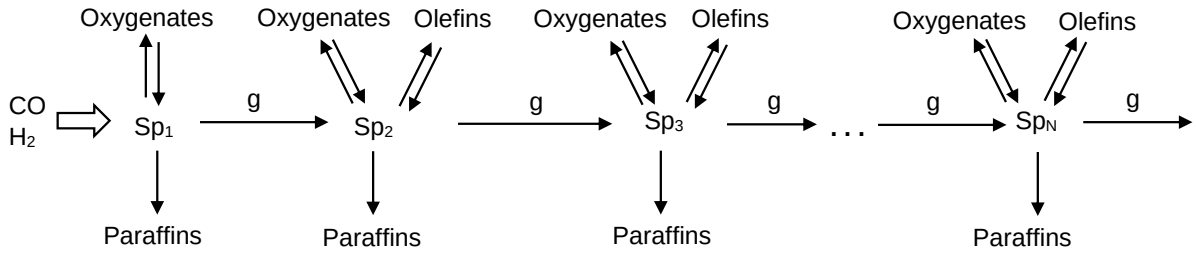

Figure 2. 4: Chain growth mechanism with oxygenates, olefins and paraffins as product classes and one class of surface species (Sp) (N: carbon number, g: growth) [33].

The likelihood of chain growth, also known as chain growth probability (*α*), is used in FT as a key indicator of the product distribution. It is typically calculated as the ratio of the rate of carbon chain propagation (R_p) to the sum of the rate of carbon chain propagation and termination (R_t) (Equation 2.8):

$$\alpha = \frac{R_p}{R_p + R_t}$$ *Equation 2. 8*

Based on the work of Dry [46], typical ranges of α on Ru, Co and Fe are 0.85 – 0.95, 0.70 – 0.80, and 0.50 – 0.70 respectively.

The ASF model assumes that the mass fraction of the hydrocarbon product with a carbon number is only dependent on the chain growth probability, which is a function of the rates of chain growth and termination. It provides a linear relationship between molar product fractions as function of carbon number and the carbon number (Equation 2.9). The chain growth probability can be determined from the slope of this relationship (Equation 10).

$$M_n = (1 - \alpha)\alpha^{n-1}$$ *Equation 2. 9*

$$log\left(\frac{M_n}{n}\right) = n \cdot log\alpha + log\left(\frac{1-\alpha}{\alpha}\right)$$ *Equation 2. 10*

Where M_n is the mass fraction of a hydrocarbon of a certain carbon number in the total product, n is the carbon number and α is the chain growth probability.

The *α* value plays a role in determining the average chain length of the hydrocarbon product obtained in FT synthesis. Methane is the only product in the FT synthesis which may have a 100 % selectivity when *α* is at 0 (Figure 2.5). The middle distillate products cannot be obtained with high selectivity. The gasoline product fraction has a maximum selectivity (48 wt.%) at an *α* of around 0.7 and diesel is produced as the main component for *α* of around 0.9 at a selectivity of about 39 wt.%.

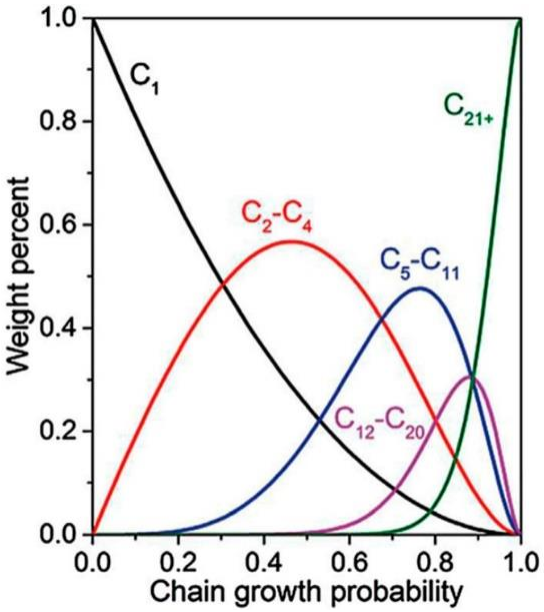

Figure 2. 5: Hydrocarbon selectivity as function of chain growth probability [47].

Deviations from ASF distribution

As noted by van der Laan and Beenackers [26], significant deviations from the ASF distribution have been reported in literature. A real FT product distribution deviates from the ideal ASF model in three key aspects. These are a higher methane yield, a lower C_2 concentration, and a secondary higher *α* value at higher carbon numbers. Kuipers et al. [48], suggested that secondary reactions including hydrogenation, reinsertion, hydrogenolysis, and isomerisation are the most likely explanation for deviations from the ASF distribution.

There are several factors that have been linked to the high methane yields, including heat and mass transfer. Dry [46], reported that mass-transfer limitations can lead to an increase in thermodynamically favoured products, which is methane. Additionally, the presence of hot spots, may result in a decrease of the chain growth probability. As stated by van der Laan and Beenackers [26], it is difficult to single out a process that consistently leads to higher methane

production. However, under certain circumstances such as the absence of mass and heat transfer limitations, the increased methane yield may be due to increased surface mobility of the methane precursor. Furthermore, the conversion of synthesis gas into methane is considered a simpler reaction as it requires a less complex site on the catalytic surface. This can result in a higher production rate of methane compared to other FT products [49,50].

Researchers have made possible explanations for the anomalies in C_2 products during FT, including secondary reactions such as the incorporation of ethene in growing chains, rapid readsorption of ethene, and hydrogenolysis of ethene [51–54]. If ethene is used as a monomer, an oscillating product distribution should be observed with a maximum at even carbon numbers. However, as described in the work of Glebov and Kliger [55] this behaviour has not been reported. Therefore, it is unlikely that ethene is incorporated as a chain starter. Secondary reactions, including the readsorption of ethene, can lead to a decrease in ethene yield and increase in ethane and higher hydrocarbons [54].

At carbon numbers above approximately 10, it has been observed that the slope of the semilogarithmic mole fractions of hydrocarbons against carbon number increases [56–58]. Two alpha values have been widely reported in iron-based FT. It has been suggested that the increased chain growth probability or two alpha values is due to the occurrence of different catalytic sites [57,58] or the existence of different chain termination reactions [49,50]. Attempts to model the hydrocarbon distribution using two different alpha values have been reported, but a closer analysis of the product distribution revealed that the distribution of paraffins follows a curved shape, instead of a linear distribution of olefins [55,59]. It is reported that the fractions of heavier hydrocarbons are in some cases lower than expected based on ASF model, but in most cases they are higher [26,49,57,60].

Product selectivity

Chain growth probability depends on several reaction variables including the reactor type, catalysts, and reaction conditions (temperature, pressure, space velocity, synthesis gas ratio) [26]. Diffusion limitations, olefin re-adsorption and vapor-liquid equilibrium have also been reported to affect FT product distribution. Increasing the operating temperature results in a shift towards lighter hydrocarbons including methane. Therefore, when targeting long chain products, it is best to operate at low temperatures. Higher partial pressures of the reactants, H_2 and CO, results in increased FT activity and a shift towards production of heavier hydrocarbons and alcohols. Higher space velocity leads to low conversions and more olefins

as the contact time between the reactants and the catalyst is shorter. High H_2/CO ratios yield more methane as the catalyst surface will have more dissociated H atoms. Furthermore, less olefins and alcohols are observed due to increased hydrogenation of these products. Alkali content in iron-based catalysts tends to increase the catalytic activity and promote chain growth while suppressing methane formation. Additionally, olefin and alcohol content in the product also increase [26]. Table 2.1 summarizes the effect of reaction conditions: temperature, pressures, feed composition and catalyst promotion, on the selectivity of FT products.

Table 2. 1: Influence of process conditions on the selectivity [26].

Parameter	Catalytic activity	Chain growth probability	Methane selectivity	Olefins selectivity	Alcohol selectivity
Temperature	+	-	+	*	-
Pressure	+	+	-	*	+
Space velocity	-	*	-	+	+
H_2/CO	*	-	+	-	-
Alkali content in iron-based catalyst	+	+	-	+	+

+ Increase with increasing parameter
- Decrease with increasing parameter
* No clear effect

2.1.4 Fischer-Tropsch catalysts

The design of the reactor depends on the type of catalyst, its activity and selectivity. Based on the data presented by Subramanian et al. [19], since atomic hydrogen is the key to the hydrogenation reaction, the catalyst should be able to dissociate hydrogen. CO can undergo dissociative or non-dissociative adsorption to produce different products. The group VIII transition metals iron (Fe), cobalt (Co), nickel (Ni) and ruthenium (Ru) are the only metals with sufficiently high hydrogenation activity to warrant application in the FT synthesis [28,61–66]. Additionally, for a non-dissociative incorporation of CO in methanol synthesis, copper catalysts are often used [67].

Among these four catalysts, Ni tends to promote methanation. The other hindrance to its industrial application is the formation of volatile and toxic carbonyl compounds, which leads to catalyst deactivation and loss of active phase. At high operating temperatures and partial pressures, Ni catalysts also suffer from thermal sintering [3,19]. Ru catalysts are very versatile in

that at high temperatures, they are active for methanation whereas at low temperatures, they produce large amounts of waxes in the low polyethene range. The waxes produced are free of oxygenated products and are essentially paraffinic. At low conversion levels, however, the lighter products contain both olefins and oxygenates [3]. Although Ru catalysts exhibits high FT activity, they are expensive, and the limited availability renders them unsuitable for large scale commercial operation. Therefore, Fe and Co are the only industrially attractive catalysts currently used commercially in FT [3].

Iron catalysts

Iron is a common choice as FT catalyst due to its low cost and high activity, which allows it to facilitate the reactions at lower temperatures and pressures compared to other catalysts. They are particularly preferred in conversion of low value feedstocks, (H_2/CO of less than 2), such as obtained from the gasification of coal due to their activity for the WGS reaction [3]. Iron-based catalysts are suitable for both the high and low temperature FT synthesis although their preparation varies significantly with the target operation temperature. There are two types of iron catalyst used in FT: precipitated and fused iron catalysts. The precipitated iron catalysts are made via precipitation of the iron compounds from aqueous solutions, resulting in high surface area catalysts. On the other hand, fused iron catalysts are made by fusing iron oxide with metal oxides, usually aluminium oxides, resulting in lower surface area but higher iron content catalysts. Fused iron catalysts are known to be more robust and resistant to deactivation than precipitated catalysts, and they are also less sensitive to changes in operating conditions. The precipitated Fe catalysts are used in fixed bed or slurry reactors for the production of waxes, while fused iron catalysts are used in fluidized bed applications [68]. As small particle sizes are prone to sintering, the catalysts used in slurry reactors and fixed beds are usually structurally promoted iron catalysts. Iron catalysts have a higher tolerance for poisoning (Sulphur from synthesis gas). However, their main drawback is they tend to deactivate quickly, requiring additional catalyst input. In addition, iron-based FT are not as selective as some other catalysts, which may result in the formation of unwanted by-products such as methane and oxygenates, that may require additional processing to remove [3].

Cobalt catalysts

Cobalt-based catalysts are interesting from the commercial point of view due to their higher activity and selectivity to linear hydrocarbons. They have high CO conversion rates and limited

tendency to WGS [69]. In the findings of Dry [3], the synthesis gas should have a H_2/CO ratio of 2.15 to ensure a high conversion. Co-based catalysts are only considered for LTFT operating mode as at higher temperatures, they produce excess methane. They have been reported to have higher resistance to attrition in slurry bubble column reactors. As cobalt is more expensive than iron, it is desirable to increase the surface metal exposure and therefore, the Co-based catalysts are mostly provided as nanoparticles supported on high surface area supports such as Al_2O_3, TiO_2, SiO_2 or zeolites [70]. Sie et al. [71] reported that the potential disadvantage of using Co as an FT catalyst is that they are more sensitive to poisoning by Sulphur-containing compounds than Fe catalysts.

2.1.5 Fischer-Tropsch reactors

The FT process is a highly exothermic reaction. Therefore, effective heat dissipation is the basis for preventing hotspots and temperature runaway. Hotspots within the reactors can lead to sintering and fouling, which will subsequently lead to catalyst deactivation and deterioration of selectivity [72]. On the other hand, temperature runaway can be a safety concern. As presented by Steynberg et al. [73], the design of these reactors is influenced by amongst other, the desired per pass conversion and inlet gas velocity. These affect product selectivity, transport and distribution, catalyst durability and stability.

High Temperature Fischer-Tropsch (HTFT) Reactors

The HTFT synthesis is based on converting synthesis gas into low molecular weight olefins and liquid products, mainly in the gasoline and diesel range. These reactors operate at 300 °C to 350 °C and a pressure in the range of 20 – 40 bar [64,74]. In the research by Saeidi et al. [74], the two HTFT reactor designs are the circulating fluidized bed reactor (CFB) and the fixed fluidized bed reactor (FFB). Temperature management is important in regulating the selectivity of the product, which affect the extent of fluidization, as such, fluidized beds cannot be used for wax production, as this will cause catalyst agglomeration [64].

<u>Circulating fluidized bed reactors</u>

In a circulating fluidized bed reactor (CFB), a gas or liquid is passed through a bed of solid particles which are suspended and agitated by the flow of the fluid (Figure 2.6). This

fluidization causes the solid particles to behave like a fluid, allowing them to mix and react with one another and with the gas or liquid flowing through the bed. The advantage of these reactors is that they have high heat and mass transfer rates, homogenous reactor temperatures and extended gas-catalyst contact time [75]. Additionally, CFB's can continuously regenerate catalysts. This is typically done by separating the spent catalyst from the fluidizing gas using a cyclone and then reintroducing fresh catalysts into the reactor [76]. This process is particularly important in maintaining the efficiency and performance of the CFD reactor over time. When this reactor is operated at high temperatures, carbon is deposited on the catalyst particles, which reduces the bulk density of the catalyst, thereby reducing the pressure difference on the vertical pipe [77]. Therefore, it is impossible to increase the catalyst load in the reaction section to compensate for the normal deactivation of the catalyst in the stream over time.

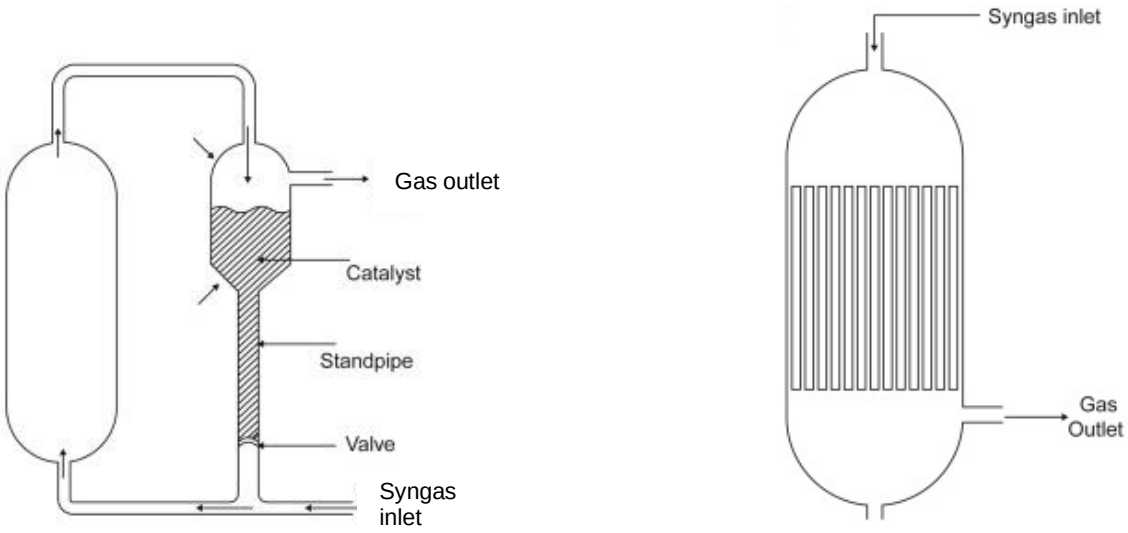

Figure 2. 6: High temperature FT reactors: circulating fluidized bed reactor (L) and fixed-bed reactor (R) [78].

Fixed fluidized bed reactors

On the other hand, the fixed fluidized bed (FFB) operates as a dense phase turbulent bed reactor and the FT reaction happens inside of the fluid mixture of catalyst (Figure 2.6). The main advantages of the fixed fluidized reactors are their lower operating costs and higher capacities [77]. Because of the wider reaction section in FFB, more cooling coils can be installed, thus increasing their capacity due to the more isothermal behaviour. FFB offers high yields of the products and high throughput because at any moment, all the charged catalyst particles in the reactor participate in the reaction. It is easier to control the temperature of the FFB, and they have lower pressure drop compared to the CFB [77].

Low Temperature Fischer Tropsch (LTFT) Reactors

These reactors are characterized by a heavier product spectrum, which is mainly composed of wax, and is liquid under reaction conditions, leading to a three-phase gas-liquid-solid system inside the reactors [72]. Different types of reactors have been used to carry out low temperature FT, and the two commonly used types of LTFT reactors industry are the multi-tubular fixed bed reactor (TFBR) and the slurry bed reactor (SBR) (Figure 2.7). Microchannel reactors are also employed at industry scale [79].

A microchannel reactor is a small device used for chemical reactions where at least one of the sides of the reaction chamber is less than 1 mm in size. This small, confined space is where the FT reaction takes place [80]. The use of these micro reactors has several advantages over the traditional reactor systems. These microreactors support an increased reaction rate and yield, resulting from a higher catalyst utilization, due to high surface-to-volume ratio [80]. These reactors can be designed to have high heat transfer coefficients, which can help maintain a stable temperature during FT synthesis. They are also reported to have good mixing properties which can be beneficial for the FT synthesis as it is a multistep process involving formation of intermediates. Nevertheless, the use of these microreactors also presents some challenges such as difficulty in effectively removing products from the reactor and increased pumping power required due to high pressure drops along the microchannels [80].

Multi-tubular fixed bed reactors

In these reactors, the FT reaction occurs inside tubes or vessels packed with the catalyst and the synthesis gas is passed through the reactor (Figure 2.7). Water circulates in-between the tubes to regulate the reactor temperature as liquid hydrocarbons and gaseous products exit through the bottom of the reactor [73]. Heat is transferred from the interior of the reactor to the outer shell via the tube walls, resulting in the production of steam. This in turn yield a temperature distributions along both radial and axial directions within the reactor [81]. The periodic replacement of the catalyst in these reactors is cumbersome and labour intensive, and it causes disturbances in the operation of the plant. However, these reactors are less expensive to operate and relatively easy to separate the catalyst from the hydrocarbon products [73].

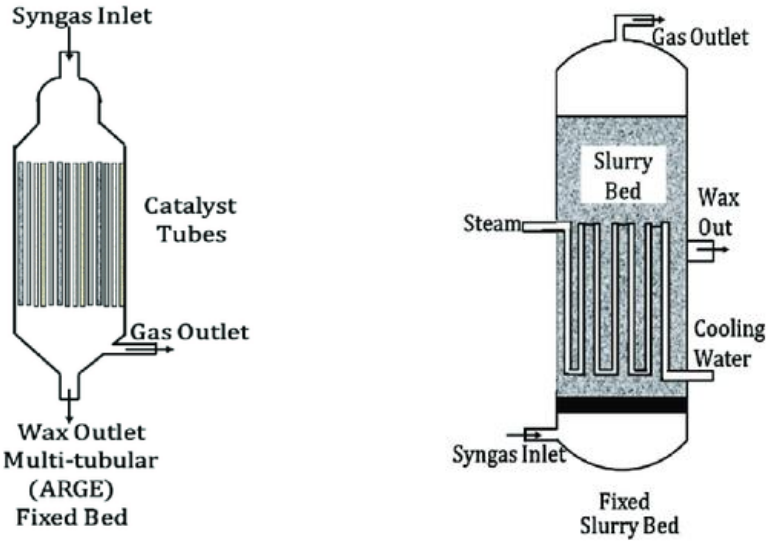

Figure 2. 7: Low temperature Fischer-Tropsch reactors: multi-tubular fixed bed reactor (L) and slurry bed reactor (R) [82].

Slurry bubble bed reactors

In a slurry bed reactor, the FT catalyst is suspended in liquid hydrocarbon product and the synthesis gas is bubbled through the reactor (Figure 2.7). The benefits of using a slurry bed reactor for FT are that, amongst others, high conversion rates, low pressure drop and good heat transfer [73]. As these reactors can be operated at a higher temperature, a higher average conversion rate can be achieved. In industry, these reactors often have bubblers that release a stream of gas into the bottom of the reactor, generating bubbles that rise through the slurry. The movement of the bubbles creates turbulence and mixing, and this helps in dissipating the heat generated during the reaction, preventing overheating and improving the stability of the reactor [83]. The liquid medium used in these reactors helps reduce the pressure drop across the reactor, making the process more energy efficient. The major drawbacks for these reactors are they are more complex to operate and maintain and the liquid medium used makes it more difficult to separate the catalyst from the products [73,84].

In laboratory settings, continuous stirred tank reactors (CSTR) and monolithic reactors are often employed [79]. CSTR are a type of reactor in which reactants are continuously fed into the reactor and mixed by an impeller or other mixing device. They have several advantages for FT synthesis. For example, CSTR are relatively simple and easy to operate, and can be used to maintain a contain reaction temperature and pressure. Additionally, they allow for easy

removal of the products. Monolithic reactors are those filled with structures called monoliths, which are made of either porous catalytic materials or an inert monolithic support with catalytic material deposited within the channels [85].

2.2 Iron-based Catalysts

In the FT synthesis, the commonly used iron catalysts are precipitated or fused. Dry [3] reported that the precipitated Fe catalysts are used in fixed bed or slurry reactors for the production of waxes, while fused iron catalysts are used in fluidized bed applications. Despite being among the most widely studied systems in heterogenous catalysts, the understanding of the complex and dynamic chemistry of iron-based FT catalysts and their rapid deactivation under FT conditions is still a developing field. The main challenges in the design of iron-based catalysts for the FT synthesis remain the high deactivation rates, and the lack of understanding regarding the structure and role of the different iron phases during FT [86].

2.2.1 Size dependency in the FT synthesis

It is well understood that catalytic performance is governed by the electronic structure of the catalyst, and as FT is a well-known structure sensitive reaction, researchers have focused on developing novel catalysts with optimum particle sizes for high FT activity and selectivity [87–92]. Several researchers have studied the effects of varying crystalline size on carbon-supported and alumina-supported FT iron catalysts in a fixed-bed reactor [89–92]. In investigating the size dependency of iron-based FT catalysts, Pour et al. [89] noted that nanoparticles have superior catalytic properties because of their increased surface-to-volume ratio and modified chemical potentials, making them preferrable over their bulk counterparts. The studies conducted by Mabaso et al. [90], Park et al. [91], and Liu et al. [92], have shown that FT activity is lower in catalysts with small crystallites. The authors ascribed the low activity to preferred oxidation of small crystallites intrinsic effects. Catalysts with small Fe nanoparticles (< 7 – 9 nm for Mabaso et al. [90], < 2 – 6.1 nm for Park et al. [91]) are reported to have a lower TOF and a higher methane selectivity, while the olefin selectivity was not affected by catalyst particle size. Additionally, Liu et al. [92] reported that smaller iron particle catalyst led to lighter olefins, and added that the olefin to paraffin (O/P) ratio of the $C_2 – C_4$ hydrocarbons was more sensitive to the catalyst pore size due to suppression of isomerization.

Interestingly, the group of de Jong [93,94] studied the conversion of synthesis gas to light olefins over supported Fe on carbon nano fibres (CNT) with and without Na and S promoters in a micro fixed bed reactor. They found a different Fe particle size effect compared to previous reports [90,91]. Different Fe size ranges of 2 – 17 nm [93] or 3 – 9 nm [94] were investigated. It is reported that after catalyst activation under H_2 flow, the TOF of CO to hydrocarbons decreased from 0.1 to 0.06/s with increasing iron carbide crystallite size from 2 – 7 nm. The same trend was also observed at low pressure, however, the CO conversion remained nearly unchanged for the unpromoted Fe/CN catalyst. The authors also reported higher CH_4 selectivity on smaller Fe particles, which is consistent with the study of Park et al. [91], but contrary to the work of Bartholomew et al. [95].

2.2.2 Catalyst promotion

Iron-based FT catalysts are usually promoted to facilitate reduction and to improve its selectivity and activity. Examples of promoters used are, potassium (K), Lithium (Li), Sodium (Na), Magnesium (Mg), Calcium (Ca), Copper (Cu), and Manganese (Mn) amongst others. Typical iron-based catalysts also contain structural promoters to facilitate the dispersion and stability of the catalysts under reaction conditions.

Chemical promoters

Several alkali and alkaline earth metals (Li, Na, K, Rb, Cs, Fr, Ba, Ca, Mg) have been used as additives to influence the catalytic performance of iron-based FT catalysts by increasing their basicity. It has been reported that the addition of alkaline metals in iron-based catalysts can enhance CO dissociative adsorption on the Fe surface and enhances the carburization of these catalysts [96–99]. At the same time the dissociative adsorption of hydrogen is suppressed. Studies have shown that the effectiveness of the alkali metals on iron-based FT activity decreased in the order of Rb > K > Na > Li. The most widely studied alkali promoter is potassium since Rb is more expensive [4].

The effect of potassium on iron catalyst behaviour have been extensively studied and is well established. Kölbel [100] have shown that potassium promotion increases CO chemisorption and decreases H_2 chemisorption on the iron catalyst surface. As reported by these authors, this is due to potassium donating electrons to iron, making it easier for CO to form a bond with iron while weakening the bond between iron and H_2. This leads to a stronger Fe-C bond and a

weaker Fe-H and C-O bonds. These findings have been supported by multiple studies on various types of iron surfaces [101–104]. Some researchers have found that the activity of the FT process can either increase or decrease as the amount of potassium added to the catalyst increases. Other studies have suggested that there is a maximum FT activity at a specific potassium loading, or that there is no clear relationship between potassium loading and FT activity. The lower melting points of alkali compared to iron oxides, carbides, and other phases in the catalysts, results in an increased mobility of alkalis on the surface of the catalysts potentially leading to the blockage of the active catalytic sites.

Farias et al. [97] investigated the effect of K promoter on the structure and catalytic behaviour of supported iron-based catalyst in FT. Three levels of K loading in the catalysts, 100Fe/5Cu/*x*K/139SiO_2, (*x* = 6, 12 and 18 on molar basis), were studied. It is reported that the addition of K resulted in a decrease in both the BET surface area and total pore volume of the catalyst. The authors postulated that the decrease in the BET surface may have been caused by the formation of larger hematite crystallites. The catalysts were reduced *in situ* with pure CO at 280 °C and 8 bar for 8 hours. H_2-TPR profiles showed two reduction peaks: one at lower temperatures, and one at a higher temperature. The authors attributed the first peak to the reduction of Fe_2O_3 and the second peak to the reduction of Fe_3O_4 and concluded that addition of K lowered the reduction temperature. FT testing was carried out in a continuously stirred tank reactor at 240 – 270 °C, 20 – 30 bar and H_2/CO = 1. It is reported that the increase in K content decreased the mass fraction of C_1 and C_2 especially at lower temperature and pressure. More higher hydrocarbons were formed with an increase in K content, at lower synthesis gas conversion. Farias et al. [97] reported that the formation of higher hydrocarbons is slower compared to formation of methane, this might have led to lower total synthesis gas conversion.

Pendyala et al. [5], studied the effect of potassium promoter loading (0, 0.5, 1.0 and 2.0 atomic ratio) on the performance of precipitated iron catalysts during FT synthesis using a continuously stirred tank reactor. Characterisation results showed that the surface area for the potassium promoted catalysts were lower than the unpromoted catalyst and dropped with increasing potassium loading. The authors ascribed these results to the pore blockage in the promoted catalysts and to a possibility of the promoter oxide clusters blocking a fraction of pores from the adsorbing gas (N_2). The stability of the catalysts is reported to have increased significantly with the addition of potassium promoter, passing through a maximum at a potassium content of 0.5 %. Addition of potassium beyond this point led to a decrease in activity and stability of the catalyst with time on stream. Potassium promotion resulted in suppressed methane and enhanced selectivity to olefins. The selectivity of the catalysts to

higher hydrocarbons increased with increasing potassium loading, and the authors again attributed this to enhancement of CO adsorption and suppression of H_2 surface adsorption. Similarly, Lohitharn and Goodwin [105] reported that promotion of iron catalyst with small amount of potassium improved their catalysts. However, as the amount of potassium loading increases beyond a certain point, the activity of the catalysts decreases.

The group of Li [98] also investigated the impact of K promoter on the performance of a precipitated iron-manganese catalyst for the FT synthesis. The K content in the Fe/Mn/K was set between 0 and 3 wt.%. It is reported that for more K content, the catalyst had larger pore diameters and lower BET surface areas and pore volumes. The authors ascribed these results to the fact that K improved the agglomeration of the FeOOH precursor and enlarged the crystallite size of α-Fe_2O_3 after calcination, which would result in the observed decrease in surface area [98]. The catalysts were reduced with synthesis gas (H_2/CO = 2) at 250 °C and 10 bars for 32 hours. Contrary to the work of Farias et al. [97], XRD analysis showed an increase in peak intensity of α-Fe_2O_3 and decrease of that of Fe_3O_4 with increasing K content, demonstrating that addition of K restrained the reduction of the catalysts. The authors ascribed these results to the strong interaction between potassium oxide and the unreduced iron oxides. FT experiments were carried out at 250 °C, 25 bar and H_2/CO = 2. A maximum catalytic activity was obtained at a particular level of K content (12KFe), after which CO conversion and WGS activity declined. Formation of methane was restrained with K content and a shift to higher molecular weight hydrocarbons was reported. Olefin hydrogenation was suppressed with K content, which led to increase in the olefin to paraffin ratio in the products. The authors reported a decrease in oxygenates selectivity with increase in K loading, that passed through a minimum at 0.7 wt.%, after which it increased with increasing K content.

In addition to potassium promotion, the effect of Mn as a promoter for iron-based FT catalysts have been widely explored. It is reported that Mn promotion leads to reduced methane formation and higher selectivity to higher hydrocarbons and more olefins. Manganese is also reported to improve the dispersion of the active species of iron. The studies by Zhang et al. [106], Tao et al. [99] and Li et al. [107] examined the effects manganese oxide on the catalytic activity of iron-based FT catalysts. The studies found that the addition of Mn promoter to the catalysts improves the olefin and middle distillation cut selectivity, increases the catalysts surface basicity, and improves the dispersion of the active catalysts.

Structural promoters

Unlike the chemical promoters, the structural promoters do not affect the intrinsic activity of the catalyst, but they modify the catalyst texture, enhance iron dispersion, and improve the catalyst stability. They act as stable surfaces over which the active component is dispersed in such a way that sintering (see Section 2.2.4) is reduced. As such, the support itself must be able to withstand even higher temperature, thus, high melting point or at least higher than the active component [108]. As per the findings of Bukur et al. [108], porosity is also a necessity for high surface area within the catalyst, but pore shape and size distribution are important secondary factors when diffusion resistance is present. The most direct influence of the support is reported to be on the active phase dispersion and morphology [109]. Examples of structural promoters are metal oxides (TiO_2, SiO_2, and MgO), carbons and zeolites [110].

It has been reported that even though supported iron-based catalysts show better activity stability due to improved resistance towards attrition and sintering, there is a strong interaction between the Fe^{2+} species and the support, resulting in the formation of iron-support species [86]. As reported by Smit and Weckhuysen [86], the dissociated metal ions from the support can easily replace iron cations and Fe can occupy vacancies in the defect support structure during activation and FT. Consequently, this metal-support interactions can affect the reducibility and carburization of the supported catalyst, resulting in lower FT activity.

Studies on the effect of different support structures on the catalytic activity of iron-based catalysts were carried out by Torres et al. [111] and Bukur and Sivaraj [112]. Torres et al. [111] investigated the effect of support properties on the catalytic activity of an iron-based catalyst supported on carbon nanofiber (CNT), *β*-silicon carbide (*β*-SiC), *α*-alumina (*α*-Al_2O_3), conventional high surface area SiO_2 and *γ*-Al_2O_3 and three bulk iron catalysts (Bulk Fe, Fe-Ti-Zn-K, Fe-Cu-K-SiO_2). The results showed that the catalysts supported on *γ*-Al_2O_3 and SiO_2 had the lowest activity, while catalysts supported on CNT and *α*-Al_2O_3 showed high conversion, high selectivity to light olefins and low methane selectivity. The authors concluded that catalysts with weak metal-support interaction showed high activity and selectivity to light olefins. Similarly, Bukur and Sivaraj [112] found that alumina suppressed the reduction of iron, while the reduction behaviour of silica-supported catalyst was similar to the unsupported iron catalysts. The authors reported that the silica supported catalysts showed higher selectivity for lower olefin content compared to alumina-supported catalyst. They attributed these results to the interaction between the potassium with the supports, leading to a reduction in the effectiveness of potassium as a promoter [112].

Reduction promoters

Even though the presence of alumina can prevent the activated iron from sintering, it is reported that structural promoters restrain the reducibility and decrease the FT activity due to the metal-support interaction [108]. For iron catalysts, the as prepared catalysts are usually in their oxidic form and need to be exposed to reducing environment in either H_2 and/or CO to activate the catalysts and form the active phase. The reduction process of iron-based FT catalyst includes the removal of oxygen atoms from the metal oxides and carburization of the reduced surface.

As reduction process is usually performed at high temperatures, the risk of particle sintering increases which can lead to loss of active surface area. Cu is often used to improve the catalyst performance and offset the disadvantages of structure promoters. The addition of these promoters in iron-based catalyst has been reported to result in higher BET surface area indicating that the presence of the promoters improves the reduction rate of the catalyst and restricts the aggregation of the Fe crystallites, resulting in greater BET surface area and smaller crystal particles [106]. In a study by Peña et al. [113], it was reported that an increase in Cu loading on iron based catalyst favoured the fragmentation and carburization of Fe_3O_4 into smaller Fe_5C_2 nanoparticles during FT. Additionally, the study revealed that Cu promotion enhances iron dispersion and reducibility via the H_2/CO spillover effect, and weakens the interactions between iron and alumina support which facilitates iron carburization and improves catalytic performance. The study found that an increase in Cu loading led to an increase in CO conversion, an increase in WGS activity and a decrease in O/P ratios due to an increased hydrogenation activity [113].

2.2.3 Catalyst activation

The oxide precursors of the iron-based FT catalysts are inactive for the reaction, as such, the oxides are subjected to an activation treatment where they are reduced and transformed into the active phase. Unlike other FT catalysts, (Ru, Co, Ni), which are activated mainly through H_2 treatment and remain in the metallic state during FT, iron-based catalysts are activated in H_2, CO or synthesis gas [114,115]. During the activation and under FT conditions, iron-based catalysts undergo several phase transformations. However, irrespective of the activation used, iron oxide will initially transform from hematite (α-Fe_2O_3) to magnetite (Fe_3O_4) [114].

Iron catalysts transform into many different phases during catalyst activation and FT, depending on the chosen reaction condition (Figure 2.8). The phase transformation from α- Fe_2O_3 to Fe_3O_4 happens rapidly in the presence of the activation gases and increased temperature. Fe_3O_4 is subsequently converted to metallic iron (α-Fe) or various iron carbides (Fe_xC).

Activation gases used in catalysts for FT process include H_2 and/or CO. Studies have shown that the type of iron carbide phase formed depends on the temperature and synthesis gas ratio [88]. Under activation with CO and H_2/CO, the Fe_2O_3 transforms to Fe_3O_4 and Fe_3O_4 is converted into various iron carbides [116–118]. It is reported that at high temperature and high H_2/CO ratio, cementite (θ-Fe_3C) is the preferred carbide. At low H_2/CO ratio and moderate temperature, Hägg carbide (χ-Fe_5C_2) is the dominant phase, and at lower temperatures and low H_2/CO ratio, epsilon carbides (ε-Fe_2C, $\acute{\varepsilon}$-$Fe_{2.2}C$, ε-Fe_3C) are preferentially formed. Of these carbides, χ-Fe_5C_2 is reported to be more active. H_2 activation of iron catalysts transforms the formed Fe_3O_4 into α-Fe [117].

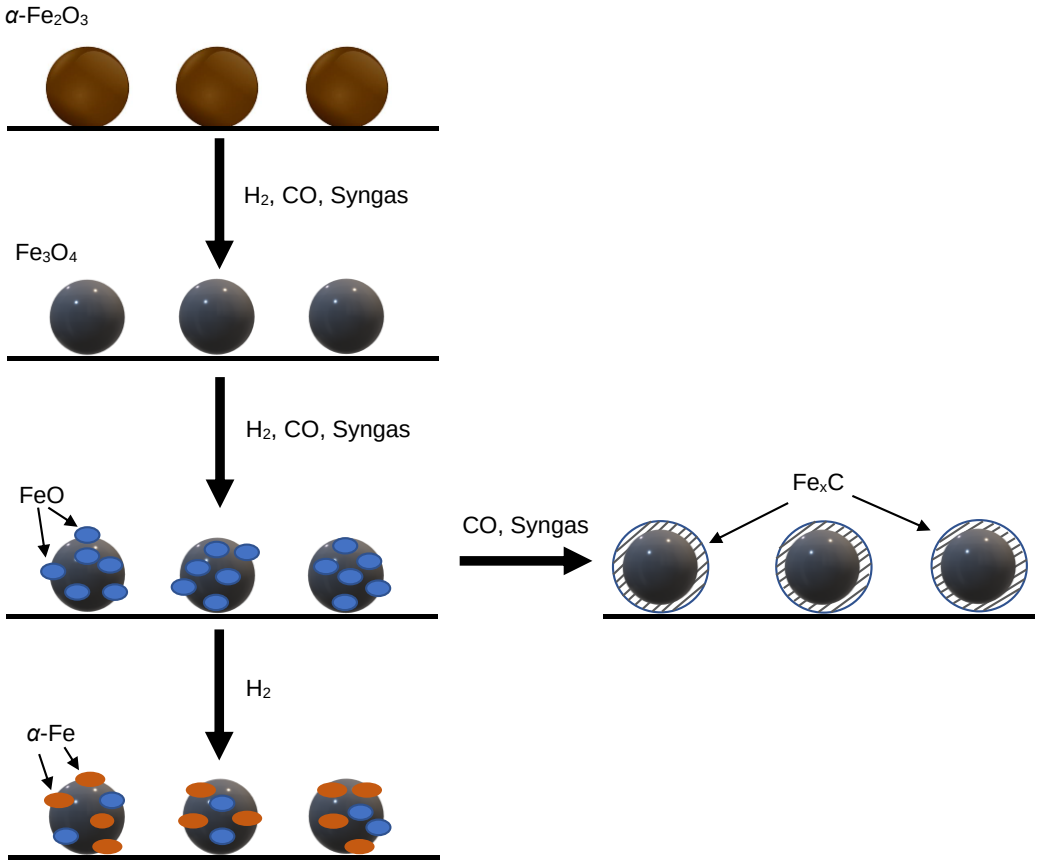

Figure 2. 8: Phase transformation of bulk α-Fe_2O_3 under different gas pre-treatment [119].

Potassium is reported to promote the formation of active carbides phases which are required for high FT activity. On CO activated catalysts, potassium promotion leads to higher initial FT activity and low methane and light hydrocarbons selectivity [116–118]. On the other hand, on H_2 activated catalysts, potassium promotion resulted in constant or even gradually increasing activity during FT. The WGS is reportedly higher with potassium promoted, H_2 activated catalysts compared to CO activated catalysts. Additionally, it was found that potassium promotion on iron-based catalysts resulted in low carbide formation on synthesis gas activated catalysts [86,88]. It is reported that activation in CO and synthesis gas led to higher initial FT activity and low methane and light hydrocarbon selectivity, while H_2 activation resulted in constant or increasing activity during FT and favoured the production of heavier hydrocarbons [117,120].

2.2.4 Catalyst deactivation

Heterogenous catalysts are faced with the problem of loss of catalytic activity over time. Catalyst deactivation increases operational costs as the catalyst must be replaced regularly. Time periods of catalyst deactivation vary, depending on factors like catalyst design, process equipment, and operating conditions. While catalyst deactivation is inevitable for most processes, some of its immediate, drastic consequences can be avoided, postponed, or reversed [121]. There are many mechanisms resulting in heterogenous catalyst decay, but for the purpose of this study, we will focus on the mechanisms relevant to iron-based FT catalyst deactivation.

While there is much debate on the main causes of catalyst deactivation for the iron-based FT catalysts, four main mechanisms of deactivation have been widely described in literature [86,121,122]:

1. Deactivation through phase change
2. Deactivation through deposition of inactive carbonaceous compounds
3. Deactivation through sintering of the active phase
4. Deactivation through poisoning

Deactivation through phase changes

It is well known that among the FT catalysts, Fe easily oxidizes and that Fe_3O_4 is found under operating conditions. Phase transformation of the iron catalyst from Fe_2O_3 to α-Fe in the case

of H_2 activation or Fe_xC under CO activation is crucial in that it determines the structural integrity or attrition resistance of the catalysts [96]. It is believed that the oxidation of the *α*-Fe and Fe_xC in the presence of water (Equation 2.11) and CO_2 (Equation 2.12) formed as by- products of FT, is one cause for catalysts deactivation [123]. Smith and Weckhuysen [86] described the deactivation by oxidation as follows:

$$xFe + yH_2O \longrightarrow Fe_xO_y + yH_2 \qquad \textit{Equation 2. 11}$$

$$xFe + yCO_2 \longrightarrow Fe_xO_y + yCO \qquad \textit{Equation 2. 12}$$

Most researchers also believe that the active phase of FT is gradually oxidized to Fe_3O_4 which is inactive for FT [122–124]. This route was summed up by Smith and Weckhuysen [86] using reaction equations to show the carbide decomposition as follows, where *C** is carbon deposit:

$$xFeC_y + yH_2O \longleftrightarrow Fe_xO_y + yH_2 + yC^* \qquad \textit{Equation 2. 13}$$

$$xFeC_y + yCO_2 \longleftrightarrow Fe_xO_y + yCO + yC^* \qquad \textit{Equation 2. 14}$$

Figure 2.9 below illustrates the change in composition of iron catalysts during FT reaction as described by Dry [3]. At time 0, the catalyst is purely metallic Fe. As synthesis gas is fed to the reactor, the metallic Fe is converted to a mixture of carbides [3]. In the early stages of the FT reaction, some of metallic Fe oxidizes to Fe_3O_4 after which, the rate of further oxidation decreases. Based on the findings of Dry [3], the initial carbide formed, *θ*-Fe_3C, is unstable and is converted to *χ*-Fe_5C_2 and eventually Fe_7C_3.

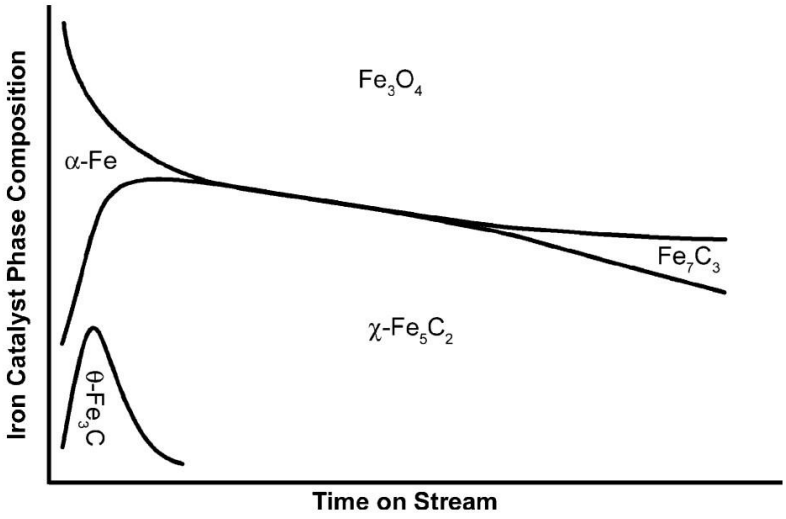

Figure 2. 9: Bulk composition changes of a pre-reduced iron catalyst during FT [3].

Water formed during the FT synthesis acts as an enabler for catalyst deactivation. With increasing conversion and along the reactor axis for fixed bed reactors, more water and CO_2 are formed. Consequently, oxidation of the active phases becomes feasible. As presented by Smith and Weckhuysen [86], iron carbides are considerably more resistant to oxidation by water than the metallic Fe and different catalysts particle sizes are affected by oxidation differently. It has been reported that smaller catalysts particles carburize rapidly and are not oxidized during FT, while larger particles are easily oxidized.

In their experimental work on twice promoted precipitated iron-based FT catalysts (100Fe:0.3Cu:0.8K), Bukur et al. [123] found that the activity of the CO or synthesis gas activated catalyst decreased with TOS while the H_2 activated catalysts showed no deactivation. The authors suggested that the higher surface concentration of H_2 on the catalyst surface after activation stabilized the catalyst activity. They ascribed the deactivation of the CO and synthesis gas pre-treated catalysts to the conversion of χ-Fe_5C_2 to Fe_3O_4. This claim was supported by Mössbauer and XRD characterization of the spent catalyst showing that χ-Fe_5C_2 was largely transformed to Fe_3O_4, $\acute{\varepsilon}$-$Fe_{2.2}C$ and siderite ($Fe(CO_3)$). χ-Fe_5C_2 might have been oxidised to Fe_3O_4 in the oxidising atmosphere near the reactor outlet, after which it could have been carburized to $\acute{\varepsilon}$-$Fe_{2.2}C$. The group linked the formation of $Fe(CO_3)$ to CO_2 produced in the WGS reaction.

Catalyst deactivation through phase change was also reported by Gormley et al. [124]. Investigating the effect of liquid wax in a slurry phase FT synthesis, the authors reported that the partial pressures of H_2O and CO_2 were responsible for the oxidation and/or sintering of the catalyst. The results showed great deactivation rates for FT in heavier wax which the authors ascribed to increased secondary reactions. The heavier products could build up over time and restrict the diffusion of hydrocarbon products and water vapor formed by WGS reaction out of the catalyst pores. The higher partial pressures of water vapor could then irreversibly oxidise the catalyst.

Deactivation through deposition of inactive carbonaceous compounds

This mechanism is commonly known as fouling, where carbonaceous or any foreign material is deposited on the catalyst's surface resulting in deactivation by loss of active surface area [86,122]. Active surface sites of the iron-based FT catalyst can be fouled and become blocked by surface poisons. Under FT operating conditions, the liquid waxes and insoluble carbonaceous compounds are formed and can block the active sites over time. The liquid waxes retard the

rate of diffusion of the reactants by partially filling the catalyst pore. On the other hand, the insoluble carbonaceous compounds permanently block active surface sites resulting in decrease in activity and high methane formation rates [86]. Additionally, over-promotion of the catalysts also results in blockage of active sites, and subsequently reduced catalyst activity. It is reported that if less K is present in the iron catalysts, the Fe carbides tend to oxidise with TOS while in excessive K loading, carbon deposition/site blocking becomes a problem.

A common way to describe the deposition of the insoluble carbonaceous compounds during FT reaction was described by Smith and Weckhuysen [86] as follows:

$$C^* + 2CO \longrightarrow C - C^* + CO_2 \qquad \textit{Equation 2. 15}$$

$$C^* + CO + H_2 \longrightarrow C - C^* + H_2O \qquad \textit{Equation 2. 16}$$

Depending on the operating temperatures, amorphous carbon (< 280 °C), or graphitic carbon is formed. The deactivated catalyst can be reactivated by hydrogen treatments at elevated temperatures (> 350 °C) or by using steam assisted catalyst regeneration [86].

On the twice promoted precipitated iron catalyst, (100Fe/0.3Cu/0.8K), Bukur et al. [123] observed catalyst deactivation with TOS. The authors ascribed this observation to the conversion of Hagg carbide to inactive (or less active) phases such as magnetite and/or siderite. Also, the catalyst deactivation is reported to be partly due to the blockage of active sites by carbonaceous deposits. In the research of Bukur et al. [123], the high conversion rates on CO and synthesis gas pre-treated catalysts implies high consumption of the surface H_2 species. As a result, the rate of removal of surface C, in potassium promoted catalysts by hydrogenation is lower than the rate of CO dissociation. Subsequently some of the C_s* forms a carbonaceous deposit which eventually converts into inactive graphitic carbon which blocks H_2 chemisorption sites resulting in catalyst deactivation. Formation of inactive carbon deposits on the surface of iron-based FT catalysts, especially on potassium promoted catalysts, has been reported as the major cause of catalysts deactivation by some researchers. Iron carbides have been postulated as the crucial phase in FT synthesis. However, the conversion of iron carbide species during the process may lead to the deactivation of the catalyst. The different species of iron carbides have different catalytic abilities, and it has been hypothesized that the deactivation of the catalyst may occur through the transformation of the active iron carbide phases into inactive or less active phases [5,125].

The observation that the iron catalyst deactivate during FT run is consistent with the findings of Niemantsverdriet et al. [126]. On investigating the behaviour of unsupported and supported metallic Fe catalysts they found that during FT at 240 °C, the rate of hydrocarbon formation was initially low, increased with TOS and eventually decreased. The conversion of *α*-Fe into iron carbides is reported to have started at a high rate and decreased rapidly. XRD and Mossbauer spectroscopy characterisation revealed that after 6.5 hours of FT reaction, there was more carbon on the catalyst. The authors postulated that the deactivation of the *α*-Fe was caused by the formation of an excessive amount of inactive carbon at the catalyst surface [126].

Deactivation through sintering of the active phase

Sintering is the loss of catalytic surface area due to migration and coalescence (Figure 2.10a) or Ostwald ripening (Figure 2.10b) of the iron phase. Particle migration and coalescence refers to the movement and merging of small particles to form larger ones. On the other hand, in Ostwald ripening, smaller crystals within the material grow at the expense of larger ones. This process is driven by the minimization of the total surface energy of the particles, which causes the smaller crystals to absorb atoms from the larger ones and grow. These processes can have a significant impact on the properties of the catalyst such as its stability and morphology.

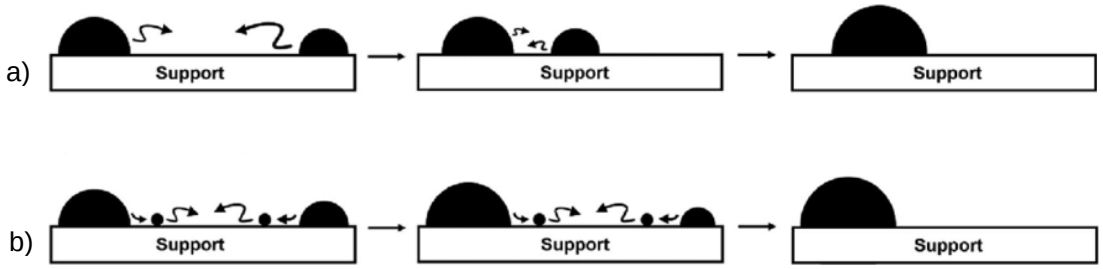

Figure 2. 10: Catalyst deactivation through particle migration coalescence (a) and Ostwald ripening (b) [127].

The loss of the catalytic surface area results in the structural modification of the catalyst. Literature describes this phenomenon using Tamman temperature, which is defined as half of the bulk melting point. Above the temperature the atoms on the surface of crystallites become mobile and as a result crystallites can sinter. For iron, this temperature is 633 °C. Even though this temperature is higher than the typical FT operating temperatures (200 – 350 °C), it is possible that the local temperature of the crystallites is much higher due to the heat released from the exothermic FT reaction.

Based on the data presented by Smit and Weckhuysen [86], sintering in iron FT catalyst is often reported in the context of reduction rather than during the FT reaction. The authors noted that during reduction, the porous structure of the Fe_2O_3 is lost as metallic Fe sinters, resulting in a decrease in surface area and pore volume. To prevent this, transition metal catalysts could be directly converted to carbides without a separate reduction step. The higher Tamman temperatures of iron carbides reduce the extent of sintering. Catalysts deactivation via this mechanism can be prevented by using catalysts supports or catalyst binders locking the active species in place supressing particle migration and to some extent ripening mechanisms.

Deactivation through poisoning

Poisoning has been described in literature as the strong chemisorption of reactants, products, or impurities on the catalytically active sites. As such, poisoning has operational meaning; that is, whether a species acts as a poison depends on its adsorption strength relative to the other species competing for the active sites [86]. Well known poisons are the electronegative elements like Cl, O, B, and sulphur compounds (H_2S, COS, CH_3SH, C_2H_5SH) [128]. Sulphur effects on iron-based FT catalysts have been widely explored. If present in high concentrations (~ 10 ppm), sulphur is reported to decrease the catalyst activity, while at lower concentrations (~ 0.5 ppm), it is reported to increase catalyst reducibility and improve olefin selectivity [129]. Since sulphur poisoned catalysts are not readily reactivated, sulphur poisoning is a significant problem for industrial FT.

Madon and Taylor [130] investigated the effect of sulphur on alkali promoted Fe-Cu in the FT synthesis. The authors reported that the presence of sulphur had little effect on the CO conversion or product selectivity. The O/P ratio was not greatly affected either. Even though the sulphided portion of the catalyst was inactive, there was sufficient remaining catalyst to allow for CO conversion, hence lack of catalyst deactivation.

Chaffee et al. [131] studied the effect of sulphur poisoning on Fe/Mn catalysts in a fixed bed reactor. They found that most of the catalyst were more sulphur tolerant at a low synthesis gas ratio ($H_2/CO = 0.5$) compared to a high synthesis gas ratio ($H_2/CO = 2$). The authors reported a significant a drop in CO conversion with H_2S addition to synthesis gas. However, the Fe-Mn coprecipitated catalyst was reported to be more resistant to S poisoning and the authors claimed that this was due to the formation of MnOS compounds that protected the iron phase from deactivation. Analytical data supported the claim that the sulphur was

removed rapidly from the gas stream such that Fe remained unexposed to it until Mn was stoichiometrically saturated.

2.3 Perovskites

There exist several material classes with the perovskite structure, and the ABO_3 type is the most studied one amongst the oxidic perovskites. Where A usually stands for an alkaline-earth or rare-earth metal cation, occupying the 12-fold coordinated cubo-octahedral cages and B designates a transition-metal cation, surrounded by six anionic oxides in an octahedral coordination (Figure 2.11). The oxidic perovskites are classified as mixed oxides and over the last decades, they have been proposed as redox catalysts [132]. The ideal crystal unit cell of the perovskites is cubic in the *Pm-3m* space group [133].

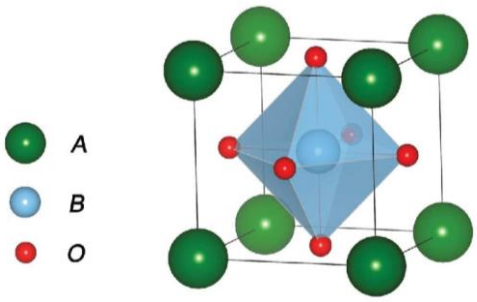

Figure 2. 11: ABO_3 perovskite structure [134].

Considering the valences on the A and B cations, and the need to achieve electroneutrality within the perovskites structure, different charge distributions between cations A and B are encountered [133]. The transition metal in B site can adopt one or multiple oxidation states, e.g., the Mn in $LaMnO_{3+\delta}$ is present in both Mn^{3+} and Mn^{4+} oxidation states.

Carrier et al. [133] reported that the stability of the perovskite structure for a desired composition is governed by two main geometric parameters. The authors postulated that first, the B^{n+} ionic radius should be larger than 0.51 Å to yield a stable BO_6 octahedron. Secondly, the Goldschmidt tolerance factor *t*, which is defined as a function of the ionic radii of A, B, and O must be between 0.8 and 1.

$$t = \frac{r_A + r_O}{\sqrt{2} \times (r_B + r_O)}$$ *Equation 2. 17*

Where *t* is the tolerance factor, r_A, r_B, and r_O are the Shannon ionic radii of the A, B, and O ions respectively. From the equation, the tolerance factors of most perovskite structures can be determined. If t > 1, the A cations have a large radius and the B cations are small, so that B ions have more room to move. For t < 1, the B cations have a larger size, and the A cations are smaller. For an ideal cubic perovskite *t* equals to 1. When *t* deviates from 1, the perovskite structure is deformed, and the symmetry is lowered resulting in orthorhombic or rhombohedral structures [135].

One significant advantage of perovskite structures is the possibility to substitute the A or B cations [133]. Peña and Fierro [136] reported that the A site is often substituted for a trivalent cation (e.g., La^{3+}) resulting in stabilized anionic or cationic vacancies. This is reported to cause significant modification of the B cation reducibility and consequently the surface and bulk oxygen mobility with direct impact on the catalytic activity [137]. The B site is often substituted with a second transition metal to stabilize the second active element in the structure [138]. As indicated by Carrier et al. [133], cation substitution might increase the resistance of the active phase against sintering during reaction, since the substitution significantly decreases the mobility of the ions on the catalyst surface.

Distortion in perovskites

Most perovskites have the BO_6 octahedra tilted in various ways to give different types of coordination of the A atoms than the cuboctahedra in the ideal cubic structure [139]. The reduced symmetry in distorted perovskites is of great importance for their magnetic and electric properties. Three main factors have been identified as being responsible for the distortion in perovskites: i) size effects, ii) deviations from the ideal composition and iii) the Jahn-Teller effect. It is rare that the distortion of a perovskite can be linked to only one of these mechanisms, in most cases several factors play a role.

i) <u>Size effects</u>

A distortion can occur because of a smaller A cation. In the ideal cubic case, A, is geometrically related to the ionic radii (r) and is defined as:

$$a = \sqrt{2}(r_A + r_O) = 2(r_B + r_O) \qquad \textit{Equation 2. 18}$$

The ratio of these two expressions for the cell length is the Goldschmidt *tolerance factor t* (Equation 2.17) and it allows estimation of the degree of distortion. In the ideal cubic perovskite of $SrTiO_3$, $t = 1$, $r_A = 1.44$ Å, $r_B = 0.605$ Å and $r_O = 1.40$ Å. If the A ion is smaller, then t becomes smaller than 1 resulting in the BO_6 octahedra tilting to fill space [139]. However, it is believed that the cubic structure occurs if $0.89 < t < 1$ [140,141]. Lower values of t lower the symmetry of the crystal structure. On the other hand, if A is larger or B is small (making t larger than 1) then the hexagonal variants of the perovskite structure are stable. Johnson and Lemmens [139] reported that in this case, the close packed layers are stacked in a hexagonal manner in contrast to the cubic one found in $SrTiO_3$ leading to face sharing of the BO_6 octahedra.

ii) Deviations from the ideal composition

The family of compounds $SrFeO_x$ ($2.5 \leq x \leq 3$) is an example of how changing the composition of the ideal ABO_3 influences the crystal structure. The valency of the Fe ions can be changed by heating a sample in either an oxidizing or a reducing environment and as a result the oxygen content can vary between 2.5 and 3 [139]. For the oxygen deficient $SrFeO_{2.875}$, some Fe ions can be assigned to the oxidation state Fe^{3+} and others to Fe^{4+}. The oxygen vacancies order to form FeO_5 square pyramids This change in ideal composition can lead to the tilting or rotation of the unit cell, which can have a significant impact on its physical properties.

iii) Jahn-Teller effect

Another mechanism for distortion is the Jahn-Teller effect. Jahn-Teller distortions describe the orbital-ordering arrangement that occur to minimize the elastic energy [142]. In some perovskites, the distortion of the structure is assigned to Jahn-Teller active ions at the B position [139]. For example, in $LnMnO_3$ (Ln = La, Pr or Nd) with Mn^{3+} ions the $3d^4$ electrons divide up into 3 t_g electrons and 1 e_g electron. The odd number of electrons in the e_g orbital causes an elongation of the MnO_6 octahedron [139].

A summary of the perovskite distortion mechanisms is illustrated in Figure 2.12, with an illustration of an ideal cubic structure for comparison.

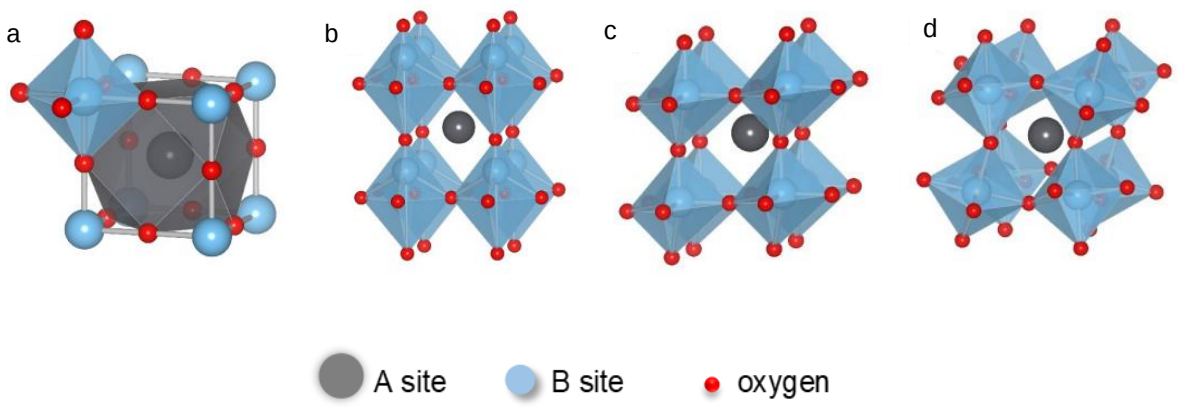

Figure 2. 12: Perovskite structure distortions mechanisms a) ideal cubic structure, b) size effect c) deviations from ideal compositions d) Jahn-Teller effect [143].

2.3.1 $LaAlO_{3-\delta}$ perovskites

Lanthanum aluminate ($LaAlO_{3-\delta}$) is a ceramic compound. At room temperature, bulk $LaAlO_{3-\delta}$ has a rhombohedral structure with the space group *R-3c* [144]. Above 540 °C, $LaAlO_{3-\delta}$ transitions from a rhombohedral to a cubic (space group *Pm-3m*) structure [145]. Figure 2.13 shows the crystal structure of the rhombohedral and cubic $LaAlO_{3-\delta}$. La^{3+} is a cation on the A site, while Al^{3+} is a cation on the B site of the perovskite structure.

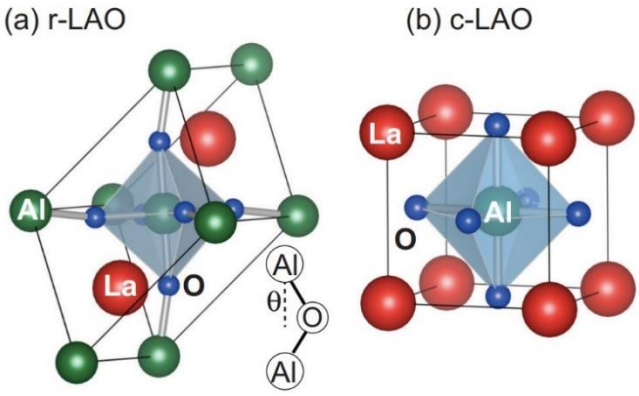

Figure 2. 13: Crystal structure of a) rhombohedral and b) cubic $LaAlO_{3-\delta}$ [144].

Lanthanum aluminate has excellent stability at high temperature, low toxicity, and high chemical resistance. It also offers a wide versatility to the substitution of the La^{3+} and Al^{3+}. $LaAlO_{3-\delta}$ has gained importance due to its possible application as a catalytic, electronic, optic, and luminescent material [146]. Quite a handful of researchers have considered $LaAlO_{3-\delta}$ as ideal for heterogenous catalysis. It has been used as a catalyst for methane combustion and CO

oxidation [147], used as a support for Ni-based catalyst for methane dry reforming [148] and for the oxidative coupling of methane [149].

A recent study on the structural and morphological properties of $LaAlO_{3-\delta}$ by Silveira et al. [150] has shown that $LaAlO_{3-\delta}$ is a good host for +3 cations as long as these have an ionic radii similar to that of the La^{3+} ion. Furthermore, the B site occupied by Al^{3+} can be substituted with transition metal ions. According to literature, $LaAlO_{3-\delta}$ perovskites have been doped on either the A or B site with rare earth ions such as Sm^{3+} and Nd^{3+} as well as noble metal ions like Ru^{3+}, Ir^{3+}, Rh^{3+} and Pd^{2+}, or with Ni^{2+}, Co^{2+}, Mn^{2+} and Fe^{3+} amongst others [146].

2.3.2 $LaTiO_{3-\delta}$ perovskites

Based on its crystal structure, lanthanum titanate ($LaTiO_{3-\delta}$) belongs to the weakly distorted cubic perovskites of the general formula RMO_3 (R = Y or rare-earth ion; M = Ti, V, Mn or other *3d* metal) [151]. $LaTiO_{3-\delta}$ has an orthorhombic structure in the space group *Pn-ma*. It is reported that the electronic state of the Ti^{3+} ion with one electron in the 3d shell is strongly degenerate; as such, it can be assumed that the $LaTiO_{3-\delta}$ is characterized by a strong electron-lattice coupling [151]. The orthorhombic phase is formed from the cubic phase of an ideal perovskite due to distortions in the environment of the Ti^{3+} ion.

The crystal structure of $LaTiO_{3-\delta}$ is comprised of six O^{2-} ions forming the octahedral environment of the Ti^{3+} ion, with eight La^{3+} ions located at the corners of the cube as shown in Figure 2.14.

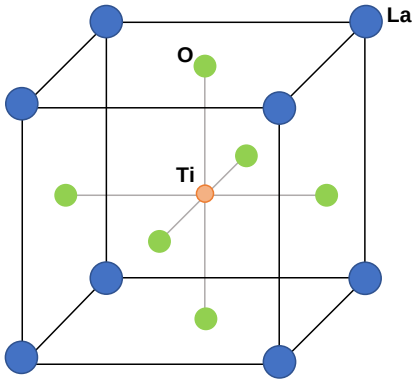

Figure 2. 14: Crystal structure of the $LaTiO_{3-\delta}$ compound.

The phase diagram of bulk $LaTiO_{3-\delta}$ has been widely studied, and it is well known that the physical properties of the $LaTiO_{x-\delta}$ for ($3 \leq x \leq 3.5$) are very sensitive to the exact oxygen

content [152]. $LaTiO_{3-\delta}$ exhibits different phases such as metallic, semiconducting, and ferroelectric insulator at room temperature. Lichtenberg et al. [152] reported that the lattice parameters in the bulk $LaTiO_{x-\delta}$ also change with oxygen content. Research has shown that $LaTiO_{3-\delta}$ is a Mott insulator containing Ti^{3+}, and slight introduction of extra oxygen in the lattice will transform the structure into metallic.

When the oxygen content in the structure reaches 3.5, thus $LaTiO_{3.5-\delta}$, the electronic properties evolve from Mott insulator (Ti^{3+}) to a band insulator (Ti^{4+}), $La_2Ti_2O_7$ [152]. Since Ti^{4+} is the energetically favoured valence, unintentional and uncontrolled overoxidation easily occurs. Unlike the Mott insulator, as an insulating oxide $La_2Ti_2O_7$ has a monoclinic structure and a stable ferroelectric phase. It is made up of perovskite slabs of distorted TiO_6 octahedra connected by La and containing eight formula units of $LaTiO_{3.5-\delta}$ per unit cell. Each slab is four octahedra thick and is linked to a neighbouring slab by A cations lying near the boundary.
Literature has reported that the stoichiometric $LaTiO_{3-\delta}$ is difficult to grow because of the extremely reducing atmosphere that is required [153]. Based on findings presented by Ohtomo et al. [154], during the initial growth stage, the first few monolayers of $LaTiO_3$ can be formed due to a stabilizing effect of the epitaxial lattice strain, however, in thicker layers $La_2Ti_2O_7$ starts to form. Figure 2.15 below shows the structure of the $LaTiO_{3-\delta}$ and $La_2Ti_2O_7$ with corresponding configuration of Ti^{3+} and Ti^{4+}.

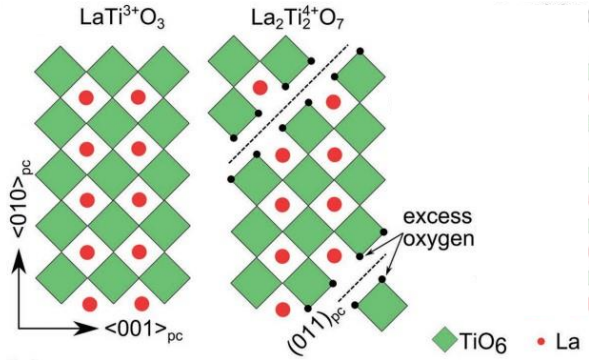

Figure 2. 15: Crystal structures of $LaTi^{3+}O_{3-\delta}$ and $La_2Ti_2^{4+}O_7$ [155].

The $LaTiO_{3-\delta}$ system and related d^1 metal perovskites have been of great interest because the oxidation to $LaTiO_{x-\delta}$ or $La_{1-x}TiO_{3-\delta}$ varies the Ti formal oxidation state and the properties with respect to the parent oxide [156]. For the La-deficient $La_{1-x}TiO_{3-\delta}$, a proportion of La^{3+} vacancies appear in the A sites, as a function of the *x* value, with the orthorhombic perovskite structure being retained. The oxidation state for titanium in these compounds is Ti^{4+}. Ruiz et al. [156] found out that the $La_{1-x}TiO_{3-\delta}$ exists for x values of $0 \leq x \leq 0.33$. It is generally accepted that when *x*

= 0.33, $La_{2/3}TiO_3$, the perovskite is unstable in its pure form due to the high content of vacant La sites in the structure [157]. Suvorov et al. [157] reported that $La_{2/3}TiO_3$ may be stabilised by incorporating 2^+ and 1^+ ions on the A sites of the perovskite structure. $La_{2/3}TiO_{3-\delta}$ is reported to be an insulator and there is a clear progression to metallic behaviour as Ti^{4+} is reduced.

Another way in which the structure and properties of these perovskites can be modified is through alkaline cation substitution into the structure to form a deformed perovskite type [156]. For example, the structure of $La_{2/3}TiO_{3-\delta}$ can be stabilized by low-level substitution of lithium cations [158–161]. Lithium cations occupy the vacant A-sites and replace some proportion of lanthanum to preserve the crystal electroneutrality, resulting in the series of perovskites $La_{1.33-x}Li_{3x}Ti_2O_6$ with tetragonal symmetry. Other alkali derivatives have been developed by substituting alkali cations into the structure: $La_{1.33-x}M_{3x}Ti_2O_6$ (M = Li, Na, K) [162]. These substitutions have been reported to induce crystallographic variation, which seems to depend on the ionic size of the alkaline cations as well as their proportion in the compound. Ruiz et al. [162] reported that the alkali cations can enter into the planes of vacancies in the perovskite structure without altering the basic symmetry, with exception of potassium. Lithium cations occupied most of the vacancies, whereas potassium is reported to occupy a limited number of cations in these planes of vacancies. The authors ascribed this limited incorporation of K^+ ions into the planes of vacancies to the larger ionic radii of K^+ compared to that of La^{3+}, which may result in a limited composition. On the other hand, the similar sizes of Na^+ and La^{3+} led to a disordered structure over the A sites.

In another work on potassium substituted $LaTiO_{3-\delta}$, Miao et al. [163] synthesized $La_{1-x}K_xTiO_{3-\delta}$ (x = 0.3, 0.35, 0.4, 0.45 and 0.5) at high temperatures and pressures. Contrary to the work of Ruiz et al. [162], the XRD analysis revealed that the x = 0.50 sample was a single phase with a cubic perovskite structure, while the other samples showed trace amount of La_2O_3 impurity despite maintaining a cubic symmetry. The authors noted that the average charge of the A site increased with an increase in K substitution. The cell volume of the substituted materials was found to be almost the same as x increased, which is in contrast to the findings of Yamamoto et al. [164]. The authors studied alkali substituted perovskites $La_{1-x}M_xTiO_{3-\delta}$ (M = Na, K: $0 \leq x \leq 0.4$) and XRD analysis showed that the orthorhombic perovskites were obtained when x = 0 and that pseudo-cubic or cubic phases were obtained when $x \geq 0$. The lattice parameters of the cubic phases in alkali substituted perovskites decreased with increase in x, which they linked to the small amounts of an impurity phase, $La_2Ti_2O_7$. Miao et al. [163] ascribed the variation in crystal structures observed between their study and Yamamoto et al. [164] to the use of different preparation methods and starting materials.

2.3.3 Perovskites in Fischer-Tropsch catalysts

Perovskite structures have been used in heterogenous catalysis as they allow for a variety of elements, active for different reactions, to be included in the structure and their high resistance to high temperature. They have also been studied in the FT synthesis as precursors of the FT catalysts and exsolution facilitators of these catalysts through doping. As Fe and Co are the commonly used metal catalysts for FT, researchers have in the past done experimental work in integrating them into a La-based perovskites to study their efficiency under FT conditions.

The group of Kiennemann have in the past focused on La(Co,Fe)O_3 perovskites as precursors to the FT [165]. A series of perovskites with varying Co and Fe loadings in the B site were synthesized via the decomposition of the Co and Fe propionates through boiling and evaporation, followed by calcination in air at temperature between 600 °C and 1000 °C. Characterisation results showed that the targeted concentrations were achieved and BET surface area was in the 3.9 to 8.8 m^2/g range with a linear decrease with decreasing Fe content within the structure [165]. XRD analysis confirmed a transition from orthorhombic to rhombohedral structure when the Co occupancy of the B site increased over 50 %. The results showed that in the absence of Co, reduction temperature was above 750 °C and as Co content increased, an increased low temperature reduction event was noted as supported by the TPR analysis. Perovskites calcined at 600 °C showed higher degrees of exsolution and in the sample with lowest Co content and lowest calcination temperature, some Fe also exsolutes forming a CoFe alloy. The authors reported that CO dissociation activity increased with increasing metallic Co content, with the CoFe alloy showing lower FT activity compared to pure Co. Under FT conditions at relatively low conversion (< 10 %), the group reported high olefin content. A high WGS activity and low oxygenates selectivity with increasing CO conversion, were observed.

In an attempt to increase the amount of exsoluted metal, Kiennemann et al. [166,167] introduced a La deficiency in the synthesis. The decrease in La content (up to 40 %) resulted in a cubic crystallographic structure and γ-Fe_2O_3 only visible in XRD at the lowest concentrations of La. The authors postulated that the cubic structure is a result of γ-Fe_2O_3 forming a core on which the perovskites crystallites grow epitaxially. During reduction, the γ-Fe_2O_3 cores reduce in part, and form an alloy with the exsoluted Co as another part replaces the cation vacancy left by the exsoluted Co resulting in a cubic Fe enriched perovskite. Compared with the non-La deficient catalysts, the group reported a higher activity in FT and a lower CO_2 selectivity at iso conversion. Higher oxygenates selectivity and higher O/P ratio in the short chain product were measured.

More work with $La(Fe,Co)O_3$ was done by Escalona et al. [168]. The group prepared catalysts with non-La deficiency and Co of ≤ 50 % on the B site via the citrate method. Characterisation of the calcined (at 700 °C) material showed BET surface areas of 12 – 15 m^2/g. In contrast to the studies by the group of Kiennemann [165], the researchers reported exsolution of the metallic Co only on the $LaCoO_3$ sample and partial oxidation in all the other samples. The group hypothesized that under FT (with biogas feed) reaction conditions, metallic Co was formed, although XRD analysis after reduction did not provide any evidence of a segregated Co^0 phase. The presence of rhombohedral species at Co concentrations as low as 0.3 was confirmed using FTIR. Escalona et al. [168] associated the presence of this crystal structure with the observed very low CO conversion levels. CO conversion increased with Co content on the orthorhombic perovskites (Co = 0, 0.1 and 0.2). The group reported that CO_2 selectivity decreased as the Co substitution decreased and Co = 0.1 had the highest CO_2 selectivity. They assumed that since CO_2 can only be formed on metallic Fe particles, there must have been small amount of Fe segregated, favouring the WGS reaction. There was decreasing selectivity towards CH_4 with increasing Co content and increasing selectivity to longer chain length with decreasing Co content. The group ascribed these observations to changes in the average particle size of Co segregates. More short chain hydrocarbons (C_8 – C_9) were formed with increase in Co particle size.

The group of Liu also worked with La based perovskites, $La(Co,Cu)O_3$, supported on mesoporous SiO_2 and ZrO_2 for the synthesis of higher alcohols [169–171]. The series of zirconia supported $LaCo_{1-x}Cu_xO_3$ (x = 0, 0.1, 0.2, 0.3) catalysts were prepared by impregnating ZrO_2 with a mixed solution composed of ions of Cu, Co and La and citric acid and calcined at 700 °C. The SiO_2 supported $LaCo_{0.7}Cu_{0.3}O_3$ catalyst were prepared via the incipient wetness impregnation method using the metal nitrates salts, dried and calcined at 600 °C. Characterisation showed that the targeted composition of $LaCo_{0.7}Cu_{0.3}O_3$ was achieved and no free Co or Cu species were observed. To force exsolution, the samples were exposed to H_2 treatment at 600 °C, resulting in monometallic phases of Co and Cu, and La_2O_3. The authors reported that a Cu shell around the Co core was formed when the sample was heated in inert before changing to H_2 treatment, and this was confirmed by HAADF-STEM-EDS analysis. Li et al. [170] reported that post heating in H_2, a Cu core with a Co shell is formed due to the higher reducibility of Cu. On the ZrO_2 support, no core shell structures but a uniform mixture of Co and Cu is reported [169]. On the silica supported catalyst, CO conversion and formation of C_xH_y increased with higher temperature, which the authors ascribed to the stronger ability of the dissociative adsorption of CO at higher temperatures. The selectivity of CO_2 is reported to have increased with the activity increase of the catalysts [170]. On the other

hand, catalytic performance investigations on the zirconia supported catalysts showed that CO conversion increased with the decrease in Cu content while the selectivities towards hydrocarbons and CO_2 increased with an increase in reaction temperature [169].

Focusing on the iron-based FT, Goldwasser et al. [172] synthesized $La_{1-x}K_xFe_{1-y}O_3$ (x = 0, 0.1, 0.2 and y = 0.1, 0.2) to produce short chain alkenes via the co-precipitation method. Characterisation results of the calcined catalysts (at 650 °C) revealed that BET surface areas were in the range of 3 – 37 m^2/g. The low K content observed for the K doped solids was ascribed to the volatility of K_2O at high temperature. Shifts in the IR bands indicated successful substitution in the B site [172]. The authors reported additional La oxide and hydroxide at increased levels of doping. Even though the doping metals had larger diameters, the cell volume of the perovskites decreased with doping, which the group ascribed to a Mn redox couple and/or oxygen vacancies. The catalysts were subjected to H_2 reduction at 450 °C to exsoluted the Fe followed by a carburisation in pure CO at 350 °C. The reducibility and carburisation of the catalysts was monitored using Mössbauer spectroscopy, and the results showed that in the absence of a dopant, only 11 % of the Fe exsolutes during reduction/carburisation/reaction and it was identified as Hägg carbide [172]. In the presence of Mn, no Fe was reduced. The presence of K resulted in the reduction of 26 % of the Fe phase which is subsequently carburised. The group postulated that during reaction, more Fe exsolutes and forms Fe_3O_4. Enhanced activity, but to a lowed extent, in the presence of both K and Mn was reported. With K doping, methane selectivity was reduced, WGS activity was suppressed and the selectivity to short alkenes was significantly enhanced [172].

As a potential catalyst for direct hydrogenation of CO_2 to fuels and chemicals, the team of Landau investigated $LaFeO_3$ [173]. The catalyst was prepared via combustion synthesis from the nitrates of the precursors and calcined at 600 °C. The as-synthesized matrix before activation was doped with 4 wt.% K as a promoter. To achieve the orthorhombic structure, the catalyst was activated at 900 °C under H_2 flow to exsolute some Fe before carburisation in a diluted 1:1 H_2/CO stream. The authors reported a mixture of wuestite, lanthanum oxide and iron carbide with some residual perovskite, after H_2 treatment. There was little chain growth activity and limited reverse WGS activity on the catalyst.

Most of the experimental work on perovskites for FT have focused on the facilitated exsolution of Co, Fe and/or Ni through doping, which in turn influences the crystal structure, rendering the material less stable during reduction. To the best of our knowledge, no attempts were found in the field for FT catalysis to increase the generally low surface area of the perovskite. In K promoted catalysts, studies that incorporate the K promoter into the perovskite structure

have been limited. To date, the work of Goldwasser et al. [172] and Khasu [20] are the only studies that have been identified that have incorporated K into the perovskite structure. In the study by Goldwasser et al. [172], Fe was also incorporated and exsoluted into the structure and from the structure during activation. However, the authors did not report on the effect of the change in phase/structure on the location and speciation of the K promoter.

To further understand the effects of incorporating K into the perovskite structure, lanthanum-based perovskites were developed and studied by Khasu [20]. In this study, the researcher prepared a series of $LaAlO_3$ perovskites catalysts by partially substituting the La with 10 atom-% K and varying amounts of Al with Mn (0, 10, 20, 60 and 100 atom-%). Potassium incorporation into the perovskite lowered the reduction temperature and accelerated the formation rate of Hägg carbide. It is reported that the perovskites with K and Mn incorporation showed an increase in CO conversion, beyond 70 %. They also showed comparable CH_4 selectivity with lower CO_2 formation, resulting in a lower overall undesired C_1 product fraction, suggesting a decoupling of the K enhancement of the FT activity versus the enhancement of the WGS reaction. These materials also showed good stability under FT reaction conditions, with no significant change in the perovskite structure post-reaction.

Patent literature

The earliest patent identified describing the use of perovskites in FT is a US application published in 2004 [174]. The use of $LaX_{0.5}Fe_{0.5}O_3$ is described as support for impregnated iron nitrate (20 wt.%) where x is Ti, V, Cr, Mn and Zr. The perovskite was prepared by mixing and heating the solid starting material to 900 °C over long periods of time. The obtained surface area can therefore be assumed to be very low. The catalysts were activated in H_2 at 500 °C and then exposed to FT conditions at 320 °C and 340 °C, 20 bar and H_2/CO ratio of 1. When compared to iron supported on La_2O_3 and $LaFeO_3$, the inventive catalyst compositions are reported to have a significantly increased CO conversion, but for the Mn loaded samples. The selectivity was reported to remain relatively stable with discrepancies in the alcohol fraction. No CO_2 formation was reported. It is reported that at 320 °C, the Mn containing sample showed a slightly reduced activity compared to the $LaFeO_3$ catalyst, but a significantly higher alcohol and lower methane selectivity. At 340 °C, the Mn containing sample was not tested, but the Cr sample displayed a significant increase in alcohol and a decrease in methane selectivity, all of which were not observed at 320 °C operating temperature. The authors did not report on the stability of the perovskites under reduction and FT conditions.

In 2008, a World Intellectual Property Organisation patent application by Shell was published which was found, by the reviewers, not novel nor inventive in 2009. Shell abandoned the patent application in 2010. While the authors claimed a wide variety of $X_aY_bO_c$ structures to act as support and/or precursors for Co-based FT catalysts, the actual examples only described stabilization of a common support, TiO_2, through incorporation of Co^{2+} ions to form a titanate [175]. These approaches had previously been reported several times in literature, to help avoid loss of active species through the uncontrolled formation of metal support compounds.

There are many other patents describing and claiming perovskites in FT synthesis, jointly published by the Fushun Research Institute of Petroleum and Petrochemicals and the China Petroleum and Chemical Corporation in 2014 [176–181]. While all applications seem to be granted in China, no submission to any other national patent office was made.

In the initial patent, an iron-based FT catalyst for a high per pass conversion with low CO_2 selectivity is claimed [176]. The ABO_3 perovskite structure, where A is mostly Ba, but it can be any other alkaline earth metal and B is 85 – 95 % Fe with the balance being Mn (but can be Pt, Co, Ni, Cu, Zn, Cr, V, Ti, Mo or Zr). Potassium (5 – 10 %) as a promoter was added outside the perovskite structure via the impregnation technique. The catalyst was reduced at 500 °C – 700 °C in H_2 or preferably in a mixture of $C_1 – C_3$ hydrocarbons. Under moderately temperature FT (MTFTS), (280 °C, 20 bar, $H_2/CO = 2$), after reduction at 650 °C at 10 bar in H_2 or ideally CH_4 flow, CO conversion of 70 – 83 % were achieved at CH_4 selectivity of below 4 % and a CO_2 selectivity between 10 – 23 %. The claim encompasses the catalyst composition and reduction process. The successive patent described the same process of catalyst preparation by replacing Ba in the A site with neodymium (Nd) and Mn with Ni [177]. Under MTFTS conditions (260 – 280 °C, 20 bar, $H_2/CO = 1.5 – 2$), CO conversion levels of 84 – 94 % were reported. CH_4 selectivity was between 4 – 6 %, while CO_2 selectivity was between 22 – 29 %.

A similar perovskite system, but Co based, was described with Ba or Ca in the A site and Co with 5 – 10 % Mo in the B site to optimize diesel fractions [178,179]. The catalysts were promoted by impregnation with K and reduced in H_2 at 300 and 450 °C and subsequently treated with CH_4 at temperatures between 500 and 700 °C. LTFT was conducted between 200 and 230 °C at 10 – 20 bar. CO conversions between 60 and 83 % resulted in low CH_4 methane selectivity with C_{5+} selectivity around 80 % and the $C_{12} – C_{18}$ (diesel) fractions of up to 62 % were reported. A Ce, La and Nd, Co perovskite with some displacement of the B site with Ti was also described. The patent claim additional promotion was achieved with Zn or Mo impregnation. Catalyst activation was done using H_2 and CH_4. $LaNi_{1-x}Co_xO_3$ [180] and $LaCu_{1-x}Co_xO_3$ [181] were

subsequently described. The group proposed reduction under H_2 atmosphere at 10 bar. Under LTFTS, (200 °C, 20 bar, H_2/CO = 2) at CO conversions of over 85 %, CH_4 selectivity of below 4 % and C_{5+} selectivity of over 85 % were reported.

The absence of reliable characterisation data makes evaluation of the patent literature challenging, as actual catalyst compositions/structures under FT conditions are not reported. However, the vast majority of publications rely on the perovskite structure as a catalyst precursor and use exsolution of Fe and/or Co to yield the active phase [165,168,172]. Promoters are sometimes incorporated in the perovskite structure, sometimes added externally. If promoters are fully incorporated in the perovskite structure, they are not expected to exsolute, and they can still provide the desired activity. The specification of the species after reduction is unavailable. However, no effort was apparent to increase to increase the surface areas of the perovskite structures.

CHAPTER 3: SCOPE

Iron-based catalysts are preferentially used commercially in the Fischer-Tropsch synthesis, even though companies like Sasol have demonstrated successful utilization of cobalt-based catalysts in low temperature Fischer-Tropsch synthesis. The significance and prevalent use of iron-based catalysts stems from their considerable advantages over cobalt-based catalysts, especially for hydrogen lean synthesis gas compositions. This preference is due to their activity for the WGS reactions increasing the H_2 concentration in situ [125]. However, for ideal performance, iron-based FT catalysts are commonly promoted to enhance reducibility, activity, and selectivity. At harsh reaction conditions, as is envisaged in the Power-to-Liquid scenario, conventional iron catalysts can be unstable. High concentrations of product water, lead to reoxidation and particle growth causing catalyst deactivation [182]. Promoter mobility also increases under these conditions further deteriorating the catalyst's performance [6].

The main goal of this research was to develop a novel perovskite-based catalyst support material encompassing both physical properties of common supports as well as promoting activity. In this study, iron nanoparticles in the form of Fe_3O_4 were deposited onto these 'empowered supports' to provide the active phase in the FT synthesis. The specific objectives of the project were to:

- Synthesize $LaAlO_{3-\delta}$ perovskite materials where La is replaced with K and Al with Mn and study their ability to stabilize the promoting elements investigated.
- Synthesize $LaTiO_{3-\delta}$ perovskite materials where the La site is substituted with K and study their ability to incorporate the promoter into the perovskite matrix without changing the perovskite structure.
- Deposit iron nanoparticles onto the developed perovskite supports and study their FT activity and selectivity in a slurry reactor.

The iron nanoparticles were synthesized using the co-precipitation method [9]. This method yields well-defined particles, and it is easy to control the particle size by altering synthesis conditions. Previous works on Fe-based catalyst for the FT synthesis concluded that catalysts containing Fe nanoparticles smaller than 7 – 9 nm are affected by structure sensitivity, showing reduced surface specific activity and unfavourable selectivity [90]. For this reason, we focused on synthesizing nanoparticles within the 7 – 9 nm range. The citrate method was used

to prepare the lanthanum-based perovskites [7]. This method was chosen for its relatively mild conditions in the calcination step, the ability to produce mildly porous materials and the ease of controlling the chemical composition of the materials [183].

The effectiveness of these synthesis methods was assessed by analysing the properties, composition, and stability of the synthesized materials using various characterisation techniques such as X-ray diffraction (XRD), transmission electron microscopy (TEM), inductively coupled plasma optical emission spectroscopy (ICP-OES), and surface area measurements via N_2 adsorption. The FT performance was tested in a laboratory continuously stirred tank reactor using a synthesis gas ratio of 2:1, at 240 °C and 15 bar. The stability of the developed catalysts was investigated by studying the spent catalysts after FT.

CHAPTER 4: EXPERIMENTAL METHODOLOGY

The overall goal of this research was to develop a novel support for the iron-based Fischer-Tropsch catalyst that incorporates the chemical and structural and functionalities within its structure. This chapter details the techniques used for the synthesis of iron oxide nanoparticles and lanthanum-based perovskite supports, together with the characterisation techniques and catalyst testing procedure.

4.1 Synthesis of unsupported iron nanoparticles

The co-precipitation method described by Fadlalla et al. [9] was used to prepare iron oxide nanoparticles. The synthesis of Fe_3O_4 was carried out using near boiling aqueous solutions of the iron precursors; 0.2 M of $Fe(NO_3)_3.9H_2O$ (Sigma-Aldrich, ACS Reagent ≥98%) and 0.1 M of $FeCl_2.4H_2O$ (Sigma-Aldrich, ReagentPlus®, 98%). 50 ml of each solution was quickly added to a near boiling solution of sodium hydroxide (35.35 g in a 1.3 L of deionized water) under constant heating and stirring. The addition of the metal precursors resulted in the immediate formation of a black precipitate. The resulting mixture was continuously stirred and held at 95 °C for 1 hour to allow sufficient time for the rearrangement of the hydroxide into the spinel structure. The mixture was then allowed to cool to room temperature overnight, permitting the precipitate to settle. The NaOH solution was siphoned off and the precipitate washed with deionized water until the filtrate reached a neutral pH. The product was air dried at room temperature and subsequently characterized.

4.2 Synthesis of support structures

4.2.1 Synthesis of $La_{1-x}K_xAl_{0.8}Mn_{0.2}O_{3-\delta}$

The citrate method was used to prepare lanthanum-based perovskites [7]. $LaAl_{0.8}Mn_{0.2}O_{3-\delta}$ was prepared via a polymeric precursor method using $La(NO_3)_3.6H_2O$, $Al(NO_3)_3 \cdot 9H_2O$, $Mn(NO_3)_2 \cdot 4H_2O$, $C_6H_8O_7 \cdot H_2O$, $(CH_2OH)_2$, (all Sigma-Aldrich 99 - 99.99 % purity), HNO_3 (ACS reagent, 70 %) and deionized water. The precursor solution was prepared by mixing the metal nitrates, citric acid, nitric acid, and deionized water together in a 250 ml round bottom flask. The solution was ultra-sonicated to achieve complete dissolution. The molar ratio of citric acid (Sigma – Aldrich, ACS reagent, ≥ 99.5 %) to the metal cations was 2:1. The solution was

stirred using a magnetic stirrer at 230 rpm and heated to 60 °C. Ethylene glycol (Sigma – Aldrich, anhydrous, 99.8 %) was added to the above solution in the molar ratio of 3:1 with respect to citric acid. The resulting solution was heated on a hot plate to about 90 °C for 1.5 hours and dried at 350 °C. The boiling solution undergoes dehydration to form a polymer complex, followed by decomposition with enormous swelling, producing a foam which auto combusts, to form a fine black powder. The precursor powder was well ground with an agate mortar and calcined at 800 °C for 6 hours in an oven (ramp rate to target temperature of 2 °C/min). The same synthesis method was followed for the preparation of potassium substituted materials, $La_{1-x}K_xAl_{0.8}Mn_{0.2}O_{3-\delta}$, where *x* is 2, 4, 6, 8 and 10 atom-%. For the synthesis of these materials, KNO_3 (Sigma Aldrich, ACS reagent, ≥ 99.0 %) was used as precursor for potassium.

4.2.2 Synthesis of $La_{1-x}K_xTiO_{3-\delta}$

Potassium substituted lanthanum titanate perovskites were prepared via a wet chemical technique [8]. The undoped $LaTiO_{3-\delta}$ gel was synthesized by dissolving 4.5 mmol of $La(NO_3)_3.6H_2O$ (Sigma-Aldrich, 99.999 %) and 4.5 mmol of $C_{12}H_{28}O_4Ti$ (Sigma-Aldrich, 97 %) in 50 ml of deionised water. After the formation of a clear solution, 26 mmol citric acid (Sigma – Aldrich, ≥ 99.5 %) and 5 mmol of ethylene glycol (Sigma – Aldrich, 99.8 %) were added and the solution was heated to 60 °C under continuous stirring at 230 rpm for 8 hours to obtain a gel. The gel was then placed in an oven at 120 °C for 24 hours for drying, yielding a brown porous solid. A similar method was followed for the A-site doping with potassium: 5, 10, 15, 20, 30 atom-%. For the synthesis of these materials, KNO_3 (Sigma Aldrich, ≥ 99.0 %) was used as precursor for potassium. The dried gel was finally calcined at 800 °C at a rate of 2 °C/min for 2 hours and subsequently characterised.

4.3 Supporting Fe_3O_4 nanoparticles

The prepared nanoparticles were loaded onto the synthesized supports via a physical mixing procedure targeting a 20 wt.% catalyst loading [184]. The mixture was suspended in deionised water for 1 hour and an ultrasonication bath was used to reduce the degree of agglomeration. The solution was then transferred into a conical flask and dried at 72 mbar at 60 °C, in a rotary evaporator. It was further dried in an oven at 60 °C for 2 hours to remove residual moisture.

4.4 Characterisation of model catalyst and support structures

Numerous characterization techniques were used to study the synthesized materials. When considered individually, these techniques do not provide sufficient information on properties such as morphology, porosity, or structure. As such, these techniques are often combined to provide valuable information about the synthesized material.

4.4.1 Powder X-Ray Diffraction (XRD)

This technique was used to determine the crystallographic structure of the synthesized materials. The iron oxide nanoparticles, perovskites materials and supported catalyst were characterized using a Bruker AXS D8 Advance X-ray laboratory diffractometer operated at 35 kV and 40 mA using a cobalt source and a LynxEye position sensitive detector (Bruker AXS). Analysis was performed with a scan range of 20 – 120 ° 2θ, a step-size of 0.01 ° and a scan rate of 0.025 °/s. The diffraction peaks of the samples obtained were analysed against the peak positions and intensities of reference patterns listed in the ICDD PDF-4 database. The XRD pattern of a particular component exhibits sharper peaks when the crystals of that component are larger. Therefore, the width of a peak in the XRD pattern can be used to determine the size of the crystals [185]. The Scherrer equation established a relationship between the breadth (B) of an XRD line at half-peak height corresponding to a specific crystal plane and the size (l) of the crystallites:

$$B = \frac{k\lambda}{l\cos\theta} \qquad \textit{Equation 4. 1}$$

Where λ is the X-ray wavelength, θ the diffraction angle and k a constant usually equal to 1. As the crystallite size increases, the line breadth B decreases. Using the above equation, the crystallite size can be estimated.

4.4.2 Transmission Electron Microscopy (TEM)

The as-synthesized perovskites, fresh and spent catalyst were characterized using transmission electron microscopy. A Tecnai F20 TEM equipped with a field emission gun operated at 200 kV was used to determine the size distribution and morphology of the prepared samples. For sample preparation, a small volume of solid was suspended in ethanol

using ultrasonication. A droplet of the supernatant was transferred onto a holey carbon-coated copper grid and dried in air for about 10 minutes before analysis. The obtained micrographs were analysed with the freeware ImageJ to obtain particle size distributions. For statistical relevance about 200 - 250 particles were counted for each sample.

4.4.3 Scanning Electron Microscopy with Energy Dispersive X-ray elemental mapping (SEM-EDX)

The distribution of K promoter on some selected samples was analysed using a scanning electron microscope with energy dispersive X-ray spectroscopy (SEM-EDX). The SEM used was a high-resolution field emission Nova NanoSEM 230 (FEI) with advanced features such as high resolution in-lens secondary, low voltage backscatter, STEM as well as Oxford X-Max silicon drift EDS detectors. The sample preparation process was like that used in TEM sample preparation: a small volume of solid was suspended in ethanol using ultrasonication then a droplet from the suspension transferred onto a carbon-coated copper grid and dried in air.

4.4.4 Surface area measurements via N_2 adsorption

The Brunauer-Emmett-Teller (BET) theory explains the physical adsorption of gas molecules on a solid surface and serves as the basis for an important analysis technique to obtain the specific surface area of materials. The specific surface area and pore size distribution of the support was determined using the BET method based on the physical adsorption and capillary condensation (Micromeritics TriStar 3000). The sample was cooled to liquid nitrogen temperature, followed by physical absorption (based on van der Waals interactions) of N_2 molecules from a known amount of gas onto the surface of the sample. From the amount of adsorbed gas, assuming monomolecular coverage, a surface area can be extracted.

4.4.5 Inductively Coupled Plasma Optical Emission Spectrometry (ICP – OES)

ICP-OES is a technique that is used to determine the composition of elements, both trace amounts and major concentrations. This technique uses dissolved samples, as such, the synthesized solid materials of the $La_{1-x}K_xAl_{0.8}Mn_{0.2}O_{3-\delta}$ were first digested. For microwave-assisted acid digestion, the sample was mixed with 5 ml HNO_3, 2 ml HCl, 3 ml H_2SO_4, and 1 ml Aqua Regia. The sample was ramped up to 220 °C in 30 minutes and this temperature was held for 1 hour. The digested sample was transferred accurately to a 50 ml volumetric flask

and filled to the mark with 2 wt.% HNO_3. Prior to the dilution the samples were filtered using a 0.2 µm filter. Thereafter 1 ml of the sample was pipetted into a 10 ml volumetric flask and filled to the mark with 2 wt.% HNO_3. 1 ml of the sample was pipetted into a 100 ml volumetric flask and filled to the mark with 2 wt.% HNO_3. The solution was injected into a Varian ES 730 ICP-OES Mars 6 Microwave Digester instrument as an aerosol where it was ionized as it passed through the plasma. Upon returning to the ground state, the atoms emit energy which the instrument records in wavelength and intensity. These were then interpreted based on the standards available and related to the concentration of the element.

Microwave-assisted acid digestion was also used for potassium substituted lanthanum titanates. The sample was digested using 5 ml HNO_3, 2 ml HCl, 5 ml H_2SO_4, 1 ml HF and 1 ml Aqua Regia. The sample was ramped up to 220 °C in 30 minutes and the temperature held for 30 minutes. The sample was then neutralized using 10 mL H_3BO_3 and heated up to 170 °C in 15 minutes and held for 10 minutes. The digested sample was then transferred to a 50 ml volumetric flask and topped-up with 2 wt.% HNO_3. Prior to the dilution the samples were filtered using a 0.2 µm filter. Thereafter 1 ml of the sample was pipetted into a 100 ml volumetric flask and filled to the mark with 2 wt.% HNO_3.

4.4.6 *In situ* X-ray diffraction

The *in situ* XRD experiments were performed using a Bruker D8 Advance laboratory X-ray diffractometer equipped with a molybdenum source ($\lambda_{K\alpha1}$= 0.7093 nm) and a position-sensitive detector (VANTEC-2000, Bruker AXS). The reduction and phase formation as well as FT synthesis process on the supported iron oxide nanoparticles were conducted using an *in situ* capillary XRD cell designed and developed at the University of Cape Town [186,187]. The catalyst reduction was performed in a continuous flow of H_2 at 5 ml/min while the temperature of the cell was increased to 450 °C at 2 °C/min and held for 15 hours to simulate the offline catalyst reduction. The samples were analysed with a scan range of 12° to 27° 2θ and total time per scan was 4 minutes (with 59 seconds delay between the scans). After reduction, the temperature was cooled down to 240 °C and the catalyst exposed to syngas (H_2/CO = 2). The capillary cell pressure was increased from atmospheric to 15 bar. The catalyst was exposed to these conditions for 24 hours, and the diffraction patterns obtained were compared to the reference patterns in the ICDD PDF-4 database.

4.5 Fischer-Tropsch synthesis experiments

4.5.1 Test unit set-up

The set-up of the test unit used in this project is shown schematically in Figure 4.1. The flow of the feed gases was controlled using mass flow controllers (Brooks 58505). Before each FT synthesis process, a 600 ml continuously stirred tank reactor (slurry reactor in Figure 4.2) was filled with wax pastilles from Sasol [188]. After which, the reduced catalyst was also added to the reactor, the reactor pressurized with Ar using a mass flow controller and heated up to 240 °C. The pressure was controlled using a back pressure regulator. Syngas with small amount of N_2 was fed to the reactor through mass flow controllers. The liquid products were collected as wax from a hot trap and product water and lower hydrocarbon liquids were collected in the cold trap. Gaseous samples were collected in pre-evacuated ampoules [189].

4.5.2 Catalyst activation

Before the FT reaction, the catalyst had to be activated to convert the iron particles into the metallic phase. This was achieved by reducing the supported catalysts in a dedicated fixed bed reduction setup. As summarized in Table 4.1, 5g of the supported catalyst was weighted out and transferred into a quartz reactor tube sealed at the bottom using quartz wool, after which the top of the catalyst was also covered with quartz wool to prevent catalyst loss during reduction. The catalyst was reduced at a temperature of 450 °C for 15 hours, (ramp rate to target temperature of 2 °C/min), under 80 ml/min of hydrogen flow. At the end of the reduction process, the reduced catalyst was cooled to room temperature and the hydrogen gas was replaced with Ar. At the same time, 20 g of Sasol H1 wax was melted in a beaker in an Ar atmosphere. The cooled catalyst was then carefully added to the molten wax, ensuring no contact with air. Once the wax was cooled to room temperature, a wax block with the reduced catalyst was formed.

Table 4. 1: Catalyst activation conditions.

Reduction conditions	
Mass of catalyst (supported Fe_3O_4)	5 g
Temperature	450 °C
Heating rate	2 °C/min
Holding time	15 hours
Pressure	Atmospheric
Activation gas	Hydrogen
Flow rate	80 ml/min

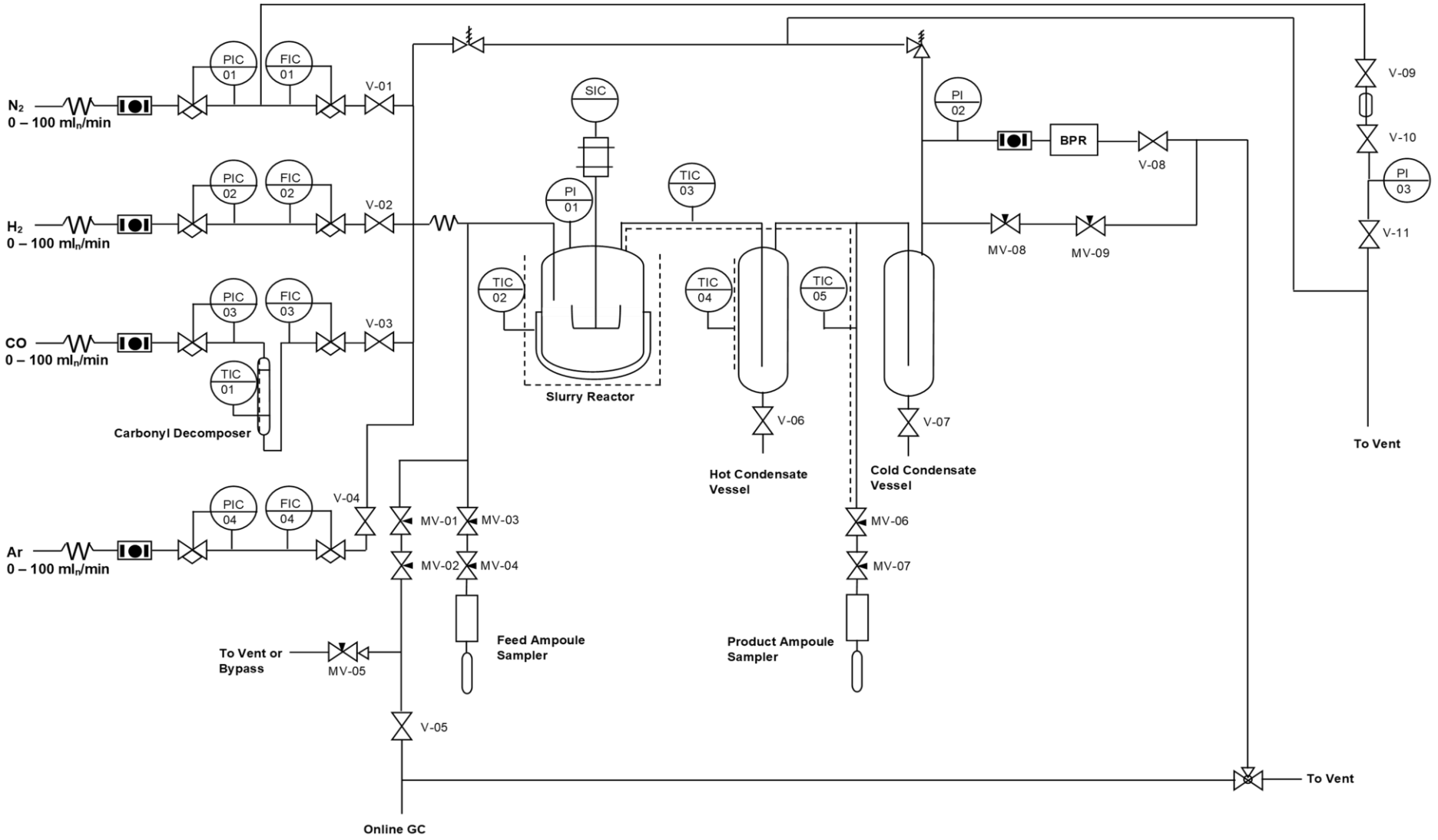

Figure 4. 1: Flowsheet of the FT slurry phase reactor.

4.5.3 Reactor start-up

The stainless steel 600 ml continuously stirred tank reactor (slurry reactor in Figure 4.2) was filled with 330 g of wax pastilles from Sasol as a slurry medium, and the wax was melted at 130 °C under Ar flow. The reduced catalyst block was added to the molten wax and the reactor sealed and gradually pressurized with Ar to 15 bar, while being heated to 240 °C and stirred at 150 revolutions per minute (rpm). Once the desired pressure and temperature were reached, the stirring speed was increased to 350 rpm and synthesis gas (H_2/CO = 2) with 10 vol.% N_2 as an internal standard for gas chromatography, was introduced to the reactor. The FT synthesis conditions are summarized in Table 4.2.

Table 4. 2: Fischer-Tropsch synthesis conditions.

Fischer-Tropsch synthesis conditions	
Mass of catalyst	5 g
H_2/CO ratio	2
Temperature	240 °C
Pressure	15 bar
Space velocity	2.4 L/(h.$g_{catalyst}$)
Nitrogen	10 vol.%

The gaseous products from the hot and cold traps were analysed in real time using a gas chromatograph that was fitted with a thermal conductivity detector (TCD). The purpose of the analysis was to determine the relative amounts of products and reactants in the gas product stream to calculate the CO conversion and the selectivity of CO_2 and CH_4. The GC-TCD was set to take a sample every 10 minutes for the duration of the FT run (see Table A.2 for operating conditions). Additionally, the gaseous products were collected in pre-evacuated ampoules after 24 and 48-hours' time on stream (TOS) [189]. These samples were analysed offline using a gas chromatograph equipped with a flame ionization detector (GC-FID).

4.5.4 Reactor shutdown

At the end of the FT run, the temperature of the reactor was cooled to 140 °C. The flow of H_2 and CO gases were closed, while the N_2 flow was maintained to prevent blockages of the feed inlet by the liquid wax. The stirring was also halted, and the catalyst was allowed to settle to the bottom of the reactor. The reactor pressure was reduced to 5 bar and the gases were

vented. The heating lines between the slurry reactor and the hot condensate vessel were raised to 180 °C to facilitate the sampling of heavy hydrocarbons. The outlet nozzle of the hot condensate vessel was heated using a butane torch, allowing for the collection of liquid wax. Subsequently, water and liquid product from the cold condensate vessel were collected. Following this, the reactor was fully depressurized, the temperatures of the lines lowered to 140 °C and N_2 gas flow closed. The liquid wax in the reactor was drained out to recover the catalyst that had settled at the bottom.

4.5.5 Spent catalyst recovery

The spent catalyst was recovered and separated from the wax using the solvent extraction method. About 3 g of crushed wax/catalyst mixture was heated up in 100 ml n-hexane and brought to boil. As n-hexane evaporated, the wax was also removed. This process was repeated until all wax was removed. The particles were left to dry for 3 hours in open air, and subsequently dried overnight at 60 °C to ensure minimal amounts of solvent in the sample. A schematic of the process is illustrated in Figure 4.2 below.

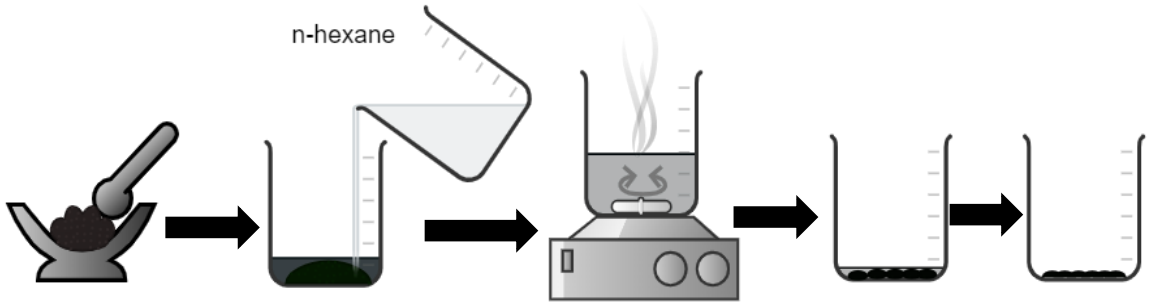

Figure 4. 2: Schematic representation of catalyst recovery process from wax.

4.6 Products analysis

4.6.1 Analysis of inorganic compound and methane

An Agilent Technologies 7820A gas chromatograph (GC) system equipped with a thermal conductivity detector (TCD) was used for analysing the permanent gases H_2, N_2, CO, CO_2, and CH_4. The software programme OpenLAB was used to analyse and calculate the peak areas. The operating conditions can be found in the Appendix (Table A.2)

The GC was first calibrated using a calibration gas cylinder with a gas mix of known compositions of N_2, Ar, CO_2, CH_4, CO and H_2 (Table A.1). Response factors were determined from the peak areas using N_2 as the reference. The peak area of each gas was related to the flow rate of each gas using equations:

$$f_i = \frac{A_{N_2}.n_{i,in}}{A_i.n_{N_{2,in}}} \quad \text{Equation 4. 2}$$

$$n_{i,out} = f_i.\frac{A_i.n_{N_{2,in}}}{A_{N_2}} \quad \text{Equation 4. 3}$$

Where $\boldsymbol{f_i}$ is the response factor of compound ***i***, $\boldsymbol{A_{N_2}}$ is the peak area of N_2 gas, $\boldsymbol{A_i}$ is the peak area of compound ***i***. $\boldsymbol{n_{N_{2,in}}}$ is the molar gas flow rate of N_2, and $\boldsymbol{n_{i,in}}$ is the molar gas flow rate of compound ***i***. $\boldsymbol{n_{i,out}}$ is the molar gas outlet flow rate of the outlet compound ***i***.

During FT synthesis, the catalyst activity (CO conversion) and yield of CH_4 and CO_2 were calculated as follows:

$$X_{CO}(\%) = \frac{n_{CO,in} - n_{CO,out}}{n_{CO,in}} \times 100 \quad \text{Equation 4. 4}$$

$$Y_{CH_4}(\%) = \frac{n_{CH_4,out}}{n_{CO,in}} \times 100 \quad \text{Equation 4. 5}$$

$$Y_{CO_2}(\%) = \frac{n_{CO_{2,out}}}{n_{CO,in}} \times 100 \quad \text{Equation 4. 6}$$

Where $n_{CO,in}$ and $n_{CH_4,in}$ are the molar gas flow rates in the feed of CO and CH_4 respectively and $n_{CO,out}$, $n_{CO_2,in}$ and $n_{CH_4,in}$ are the molar gas flow rates of CO, CO_2 and CH_4 in the reactor outlet flow.

The selectivity of gas compound ***i*** on a carbon basis was determined using the equation 4.7:

$$S_{i,C} = \frac{Y_{i,C}}{X_{CO} - Y_{CO_2}} \quad \text{Equation 4. 7}$$

While the selectivity of CO_2 on a carbon basic was calculated from:

$$S_{CO_2,C} = \frac{Y_{CO_2,C}}{X_{CO}} \qquad \textit{Equation 4. 8}$$

Where $Y_{i,C}$ is the yield of compound i, $S_{i,C}$ is the selectivity of compound i on a carbon basis, X_{CO} is the CO conversion and Y_{CO} is the yield of CO.

4.6.2 Analysis of hydrocarbons

The light hydrocarbons were sampled using an ampoule at the product ampoule sampler [189] (see Figure 4.1). The ampoules were analysed using a Varian GC 3900 gas chromatograph equipped with a flame ionization detector (FID) whose operating conditions are given in Table A.3 in the Appendix. To achieve effective separation of C_1 and C_2 species on the CP-Sil 5CB column, the GC oven was initially cooled to -55 °C using liquified CO_2 before heating gradually to 250 °C. The hydrocarbons elute at different retention times depending on their interactions with the stationary phase.

The strength of the signal of each hydrocarbon is related to the number of carbon atoms in the molecule and whether these atoms are bonded to an oxygen atom (oxygenates). There are published theoretical methods for calculating an increment in the response factors to account for the different oxygenates. Carbon atoms bonded only to the hydrogen or other carbon atoms were assigned an increment of 1. Carbon atoms with a single bond to oxygen were assigned an increment of 0.55 and carbon atoms with carbon and oxygen double bond do not give any response. From this, the response factor was then calculated for every compound of the FT product spectrum:

$$f_i = \frac{N_{c,i}}{N_{C(noO)} + 0.55 N_{C(CO)}} \qquad \textit{Equation 4. 9}$$

Where f_i is the response factor for a given compound **i**, $N_{c,i}$ is the total number is the carbon atoms in the compound i, $N_{C(noO)}$ is the number of carbon atoms not bonded to oxygen and $N_{C(CO)}$ is the number of carbon atoms with a single bond to an oxygen atom.

Identification of the different FT product species was conducted by comparing the eluted hydrocarbons with known product spectra and calculation of compound specific Kovats indices [190]. Kovats indices are specific for each compound in the FT product spectra. In essence, the n-paraffins start with a Kovats index of 100 for CH_4 (C_1), 200 for ethane (C_2) and 300 for propane (C_3) etc. [191]. Using the retention times of the n-paraffins in the product spectra, all other compounds' Kovats indices can be calculated, assuming isothermal chromatography:

$$KI = 100\left[n + (N-n)\frac{\log(RT_{unknown}) - \log(RT_n)}{\log(RT_N) - \log(RT_n)}\right] \qquad \textit{Equation 4. 10}$$

Where KI is the Kovats index, RT is the retention time of the unknown peak, n is the smaller carbon number and N is the larger carbon number (N = n+1) of the n-paraffin peak.

The molar flow rate of each compound could then be calculated using the CH_4 concentration obtained from GC-TCD, as an internal standard:

$$n_i = \left(\frac{N_{CH_4}}{N_i}\right).\left(\frac{f_i.A_i}{f_{standard}.A_{CH_4}}\right).n_{CH_4} \qquad \textit{Equation 4. 11}$$

Or based only on carbon:

$$n_{i,C} = N_{CH_4}.\left(\frac{f_i.A_i}{f_{standard}.A_{CH_4}}\right).n_{CH_4} \qquad \textit{Equation 4. 12}$$

Where n_i is the molar flow rate of the compound ***i***, N_{CH_4} is the number of carbon atoms in CH_4, f_i and A_i are the response factor and peak area for compound ***i*** respectively, $f_{standard}$ and A_{CH_4} are the response factor and peak area for CH_4 respectively, n_{CH_4} is the molar flow rate of CH_4, and $n_{i,c}$ is the flow rate of compound ***i*** on carbon basis. The results for the GC-TCD calibration and its operation conditions are as shown in Table A.1 and Table A.2 in the Appendix.

CHAPTER 5: RESULTS AND DISCUSSION

Potassium has been widely used as a promoter for iron-based FT catalysts [97,98,192,193]. Since the radius of the potassium atom is relatively big, it does not dissolve in the crystal lattice of the iron catalyst and remains on the catalyst's surface. If added in larger amounts and under certain reaction conditions, potassium species become mobile and can diffuse away from the active sites or block them [97]. In this study we developed novel perovskite-based support materials incorporating the K promoter up to 10 atom-% loading in lanthanum aluminates and up to 30 atom-% in lanthanum titanates, locking it in the crystal structure of the perovskites to suppress its mobility, and ensuring the K promoter is atomically dispersed. The iron phase was then deposited onto these empowered supports in form of oxidic nanoparticles.

This chapter details the observed characterisation results of the prepared iron catalyst, the promoted and unpromoted perovskites supports, as well as the effect of K promotion on Fe-based Fischer-Tropsch activity and selectivity and characterisation of the spent catalysts.

5.1 Characterization of fresh catalysts

A co-precipitation method was used to synthesize the iron oxide nanoparticles [9]. The potassium substituted lanthanum aluminate perovskites, $La_{1-x}K_xAl_{0.8}Mn_{0.2}O_{3-\delta}$, where *x* is 0, 2, 4, 6, 8 or 10 atom-%, were prepared via the modified citrate method. On the other hand, the $La_{1-x}K_xTiO_{3-\delta}$, where *x* is 0, 5, 10, 15, 20 or 30 atom-% were prepared via a wet chemical technique [8]. For details on the employed synthesis techniques see Chapter 4.

5.1.1 Iron oxide nanoparticles

The XRD patterns of the synthesized iron oxide nanoparticles (NPs) match the tabled reflexes of magnetite (ICDD PDF-2 entry 01-071-6336) as shown in Figure 5.1. The broadness of the diffraction reflexes show that Fe_3O_4 nanoparticles were formed in small crystallite sizes and using the Scherrer equation on the most intense reflexes, the volume based average crystalline size is estimated to be 8 nm. Similar results have been previously reported by Fadlalla et al. [9].

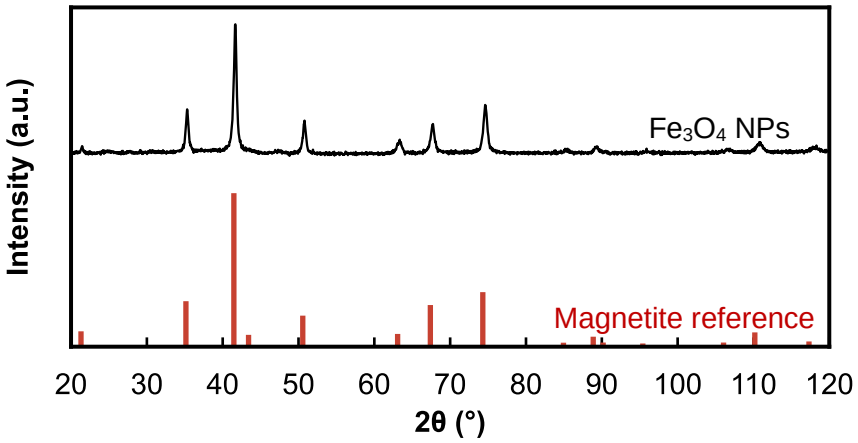

Figure 5. 1: XRD pattern of as-synthesized iron oxide nanoparticles.

TEM was used to determine the size distribution and morphology of the synthesized iron oxide nanoparticles. The size distribution of the nanoparticles was found to range from 5 to 11 nm, with an average particle size of 8 nm, as depicted in Figure 5.2 The nanoparticles exhibit a uniform spherical shape and no signs of agglomeration were observed. These observations are in agreement with the finding of Fadlalla et al. [9], who reported an average crystallite size of 7 nm for Fe_3O_4 nanoparticles determined by Rietveld refinement. This average particle size falls within the range in which excessive methanation due to the structure sensitivity of the FT process is not expected during the FT synthesis [89]. The theoretical surface area of the nanoparticles was calculated to be 174 m^2/g as detailed in Table A.4 in Appendix.

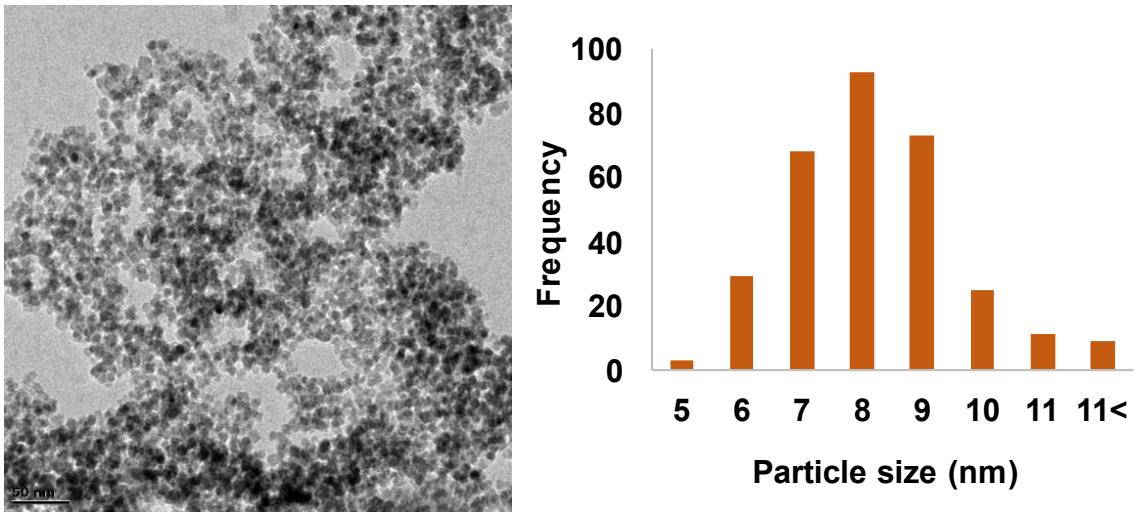

Figure 5. 2: TEM image and size distribution for Fe_3O_4 NP's.

5.1.2 $La_{1-x}K_xAl_{0.8}Mn_{0.2}O_{3-\delta}$ perovskites

XRD analysis on the potassium substituted lanthanum aluminates shows that all samples are perovskites-type solids and display the same diffraction patterns in XRD which match a reference pattern of $LaAlO_3$ perovskite structure (COD 8103607) (see Figure 5.3). All synthesized perovskites exhibit the same cubic lattice of the space group *Pm–3m* (221). The d-spacing of the (110) plane shifts to higher values with an increase in K content, an indication of an increase in the lattice volume due to the incorporation of potassium. Cimino et al. [147], reported similar diffraction patterns and concluded that the observed displacement towards lower 2θ angles corresponds to an expansion of the unit cell volume. Decreasing intensity and broadening of the reflexes with an increase in K content is also observed, suggesting a reduction in crystallite size.

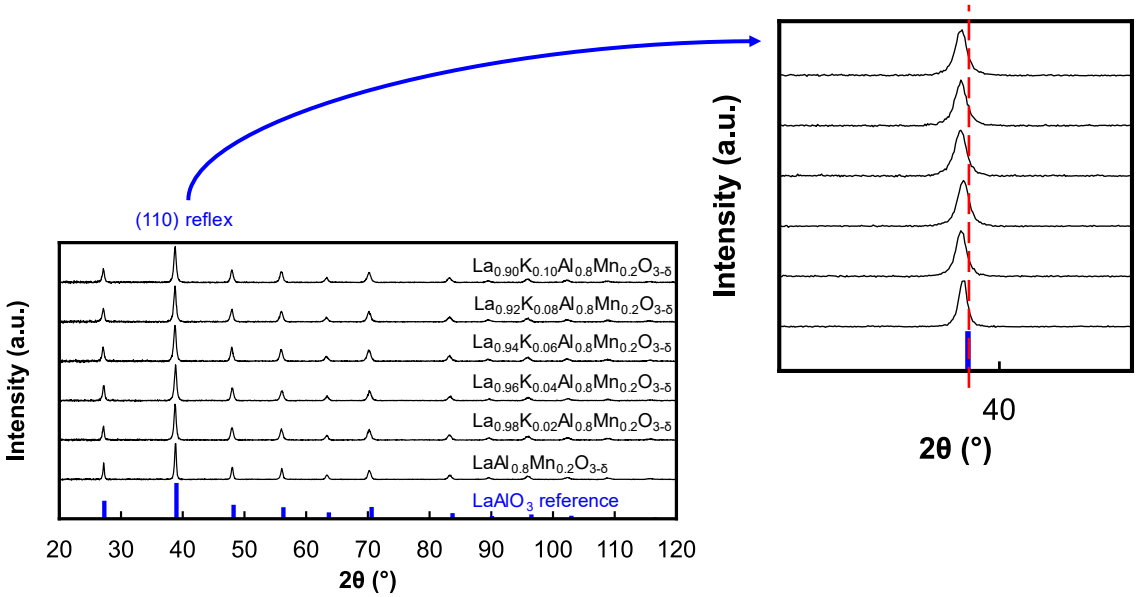

Figure 5. 3: XRD patterns of the $La_{1-x}K_xAl_{0.8}Mn_{0.2}O_{3-\delta}$ perovskites.

The surface morphology and structural details of these materials were analyzed using TEM and SEM. Figures 5.4A–F depict a porous material for the $LaAl_{0.8}Mn_{0.2}O_{3-\delta}$, $La_{0.94}K_{0.06}Al_{0.8}Mn_{0.2}O_{3-\delta}$ and $La_{0.9}K_{0.1}Al_{0.8}Mn_{0.2}O_{3-\delta}$ perovskites. These materials have uneven shapes and sizes, which Khasu [20] reported could have been due to the variations in temperature during the combustion process (see Chapter 4.2.1).

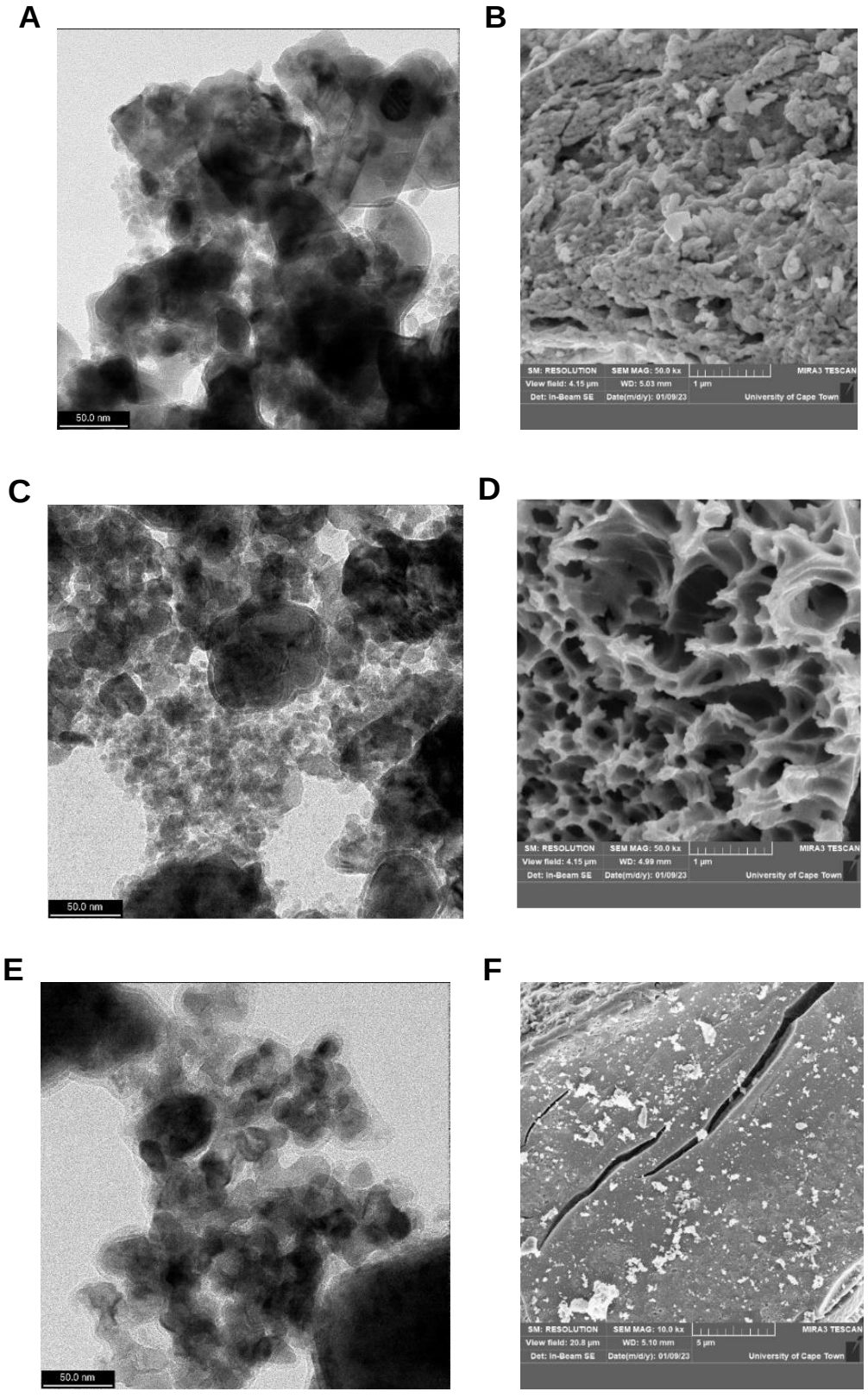

Figure 5. 4: TEM images and SEM images of $LaAl_{0.8}Mn_{0.2}O_{3-\delta}$ (A, B), $La_{0.94}K_{0.06}Al_{0.8}Mn_{0.2}O_{3-\delta}$ (C, D) and $La_{0.9}K_{0.1}Al_{0.8}Mn_{0.2}O_{3-\delta}$ (E, F).

The homogeneity of the elements in these samples was analyzed using SEM-EDX analysis. The maps revealed that the elements in the perovskite structures are evenly distributed (Figure 5.5A – C) with no visible enrichments.

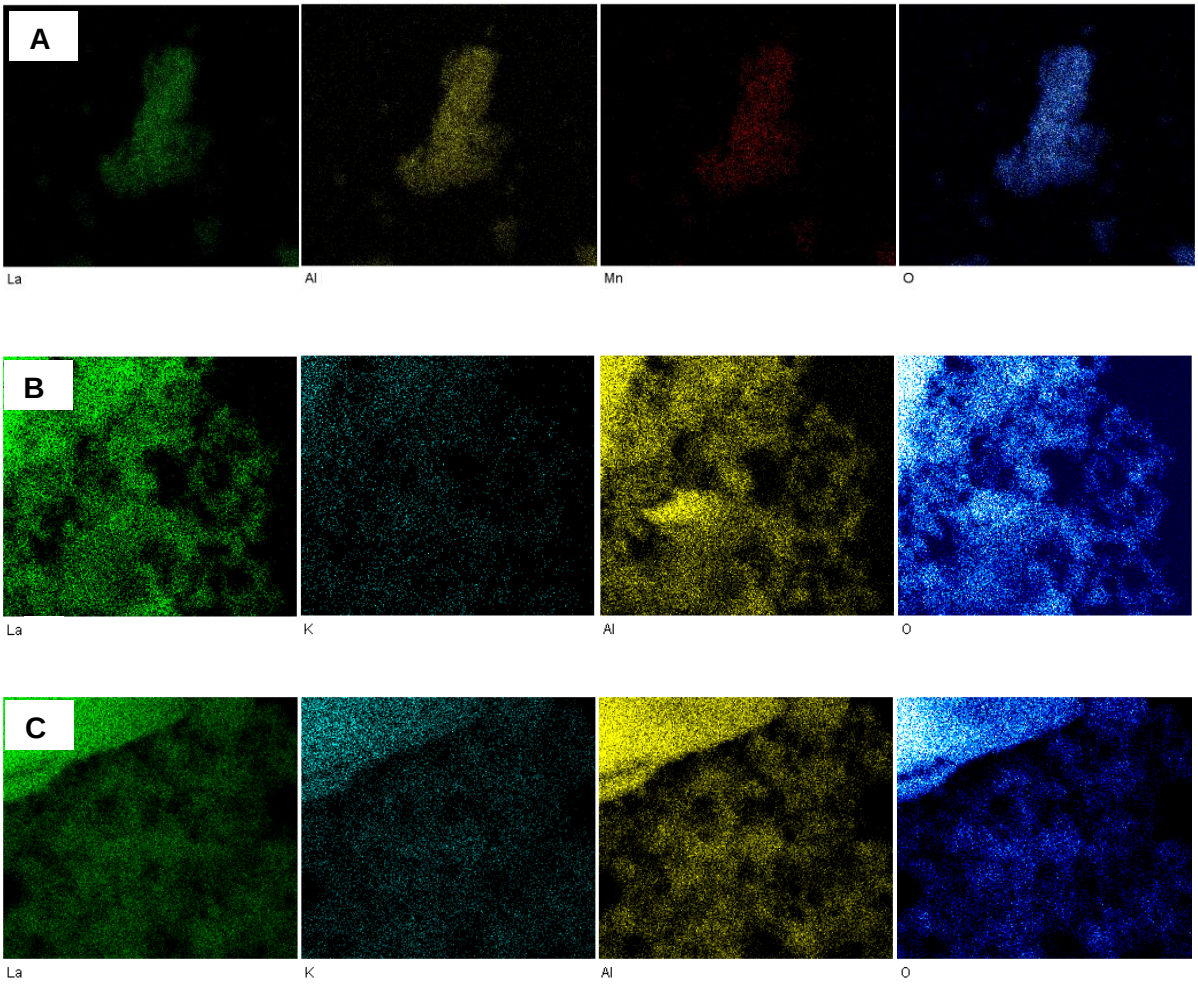

Figure 5. 5: SEM-EDX elemental mapping micrographs of $LaAl_{0.8}Mn_{0.2}O_{3-\delta}$ (A), $La_{0.94}K_{0.06}Al_{0.8}Mn_{0.2}O_{3-\delta}$ (B) and $La_{0.9}K_{0.1}Al_{0.8}Mn_{0.2}O_{3-\delta}$ (C).

The elemental composition of the perovskites was determined using ICP–OES. Table 5.1 below compares the expected composition of all the materials to the actual elemental compositions. The results show that the element compositions in the support structures are close to the target values, indicating the efficiency of the citrate method for catalyst preparation. In his work, Khasu [20] reported similar observations and credited that to the synthesis method that did not include any separation techniques such as crystallization or filtration.

Table 5. 1: Elemental composition analysis of the $La_{1-x}K_xAl_{0.8}Mn_{0.2}O_{3-\delta}$ perovskites.

Catalyst	Targeted wt.%				ICP-OES wt.%			
	La	K	Al	Mn	La	K	Al	Mn
$LaAl_{0.8}Mn_{0.2}O_{3-\delta}$	80.8	0.00	12.9	6.30	81.0	0.18	12.5	6.33
$La_{0.98}K_{0.02}Al_{0.8}Mn_{0.2}O_{3-\delta}$	80.3	0.46	12.8	6.42	79.5	0.66	13.3	6.56
$La_{0.96}K_{0.04}Al_{0.8}Mn_{0.2}O_{3-\delta}$	79.5	0.92	12.9	6.55	79.3	0.98	13.1	6.68
$La_{0.94}K_{0.06}Al_{0.8}Mn_{0.2}O_{3-\delta}$	78.9	1.42	13.0	6.61	78.6	1.42	13.2	6.80
$La_{0.92}K_{0.08}Al_{0.8}Mn_{0.2}O_{3-\delta}$	78.2	1.92	13.1	6.73	77.4	1.93	13.7	6.98
$La_{0.90}K_{0.10}Al_{0.8}Mn_{0.2}O_{3-\delta}$	77.4	2.43	13.4	6.83	76.6	2.38	13.7	7.29

BET surface area and pore volume of the materials were determined from N_2 adsorption-desorption isotherms. The synthesized perovskites materials yielded BET surface area of 12 – 31 m^2/g. The results indicated that incorporation of K influences the surface areas of the materials. The K substituted materials had a higher BET surface area compared to the material with no potassium. However, this increase does not appear to be linear but rather constant, within the error ±5 % of experimentation. The pore volume mirrors the trend of surface area (Table 5.2).

Table 5. 2: BET surface area of the synthesized $La_{1-x}K_xAl_{0.8}Mn_{0.2}O_{3-\delta}$ perovskites.

Catalyst	BET surface area (m^2/g)	Pore volume (cm^3/g)
$LaAl_{0.8}Mn_{0.2}O_{3-\delta}$	12	0.09
$La_{0.98}K_{0.02}Al_{0.8}Mn_{0.2}O_{3-\delta}$	24	0.12
$La_{0.96}K_{0.04}Al_{0.8}Mn_{0.2}O_{3-\delta}$	28	0.14
$La_{0.94}K_{0.06}Al_{0.8}Mn_{0.2}O_{3-\delta}$	31	0.13
$La_{0.92}K_{0.08}Al_{0.8}Mn_{0.2}O_{3-\delta}$	27	0.13
$La_{0.90}K_{0.10}Al_{0.8}Mn_{0.2}O_{3-\delta}$	26	0.15

The iron catalyst was deposited onto the $La_{1-x}K_xAl_{0.8}Mn_{0.2}O_{3-\delta}$ perovskites in the form of iron oxide nanoparticles with a targeted loading of 16 wt.% metallic Fe and subsequently characterized. As expected XRD analysis of the catalysts shows contributions of both the perovskites materials and the iron oxide phases. It was observed that there were no new phases or changes in the perovskite structure (Figure 5.6).

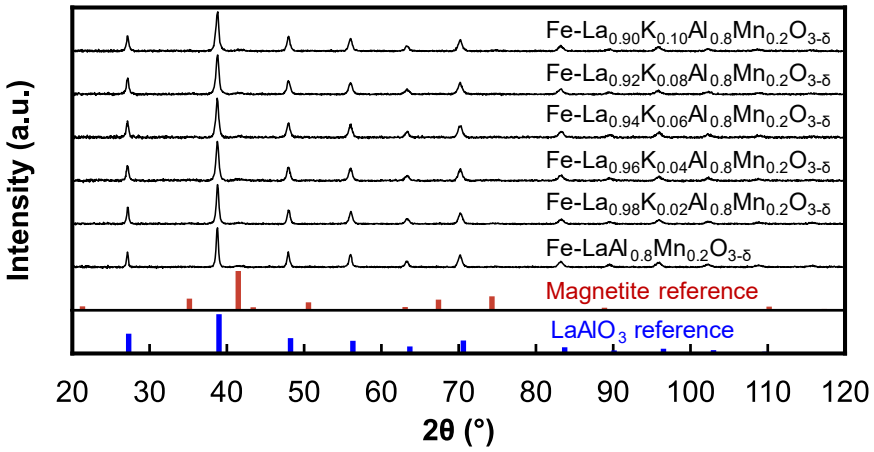

Figure 5. 6: XRD patterns of Fe_3O_4 supported $La_{1-x}K_xAl_{0.8}Mn_{0.2}O_{3-\delta}$ perovskites.

The porous characteristics of the perovskite materials after iron oxide nanoparticle deposition were evaluated using BET analysis. Addition of the nanoparticles results in an increase in these surface areas compared to the as prepared samples (Table 5.2) by 15 to 20 m^2/g (Table 5.3). As such, the surface of the iron oxide represents a significant fraction of the total surface area. The BET surface area was also calculated to compare with the experimental results, and results can be found in Appendix C.

Table 5. 3: Porous nature of the Fe_3O_4 supported $La_{1-x}K_xAl_{0.8}Mn_{0.2}O_{3-\delta}$ perovskites.

Catalyst	BET surface area (m^2/g)	Pore volume (cm^3/g)
$Fe\text{-}LaAl_{0.8}Mn_{0.2}O_{3-\delta}$	35	0.12
$Fe\text{-}La_{0.98}K_{0.02}Al_{0.8}Mn_{0.2}O_{3-\delta}$	43	0.14
$Fe\text{-}La_{0.96}K_{0.04}Al_{0.8}Mn_{0.2}O_{3-\delta}$	45	0.15
$Fe\text{-}La_{0.94}K_{0.06}Al_{0.8}Mn_{0.2}O_{3-\delta}$	46	0.15
$Fe\text{-}La_{0.92}K_{0.08}Al_{0.8}Mn_{0.2}O_{3-\delta}$	48	0.17
$Fe\text{-}La_{0.90}K_{0.10}Al_{0.8}Mn_{0.2}O_{3-\delta}$	47	0.19

The loading of the Fe_3O_4 nanoparticles onto the perovskites was studied by utilizing ICP-OES (see Table 5.4). The Fe loading was determined to be between 11 and 14 wt.%. The obtained values were lower than the targeted, and these deviations from the theoretical value may be attributed to experimental errors in the synthesis method: fluctuations of the balances during weighting of samples.

Table 5. 4: Iron loading in the different $La_{1-x}K_xAl_{0.8}Mn_{0.2}O_{3-\delta}$ perovskites.

Catalyst	Iron loading (wt.%)
Fe-$LaAl_{0.8}Mn_{0.2}O_{3-\delta}$	11
Fe-$La_{0.98}K_{0.02}Al_{0.8}Mn_{0.2}O_{3-\delta}$	13
Fe-$La_{0.96}K_{0.04}Al_{0.8}Mn_{0.2}O_{3-\delta}$	12
Fe-$La_{0.94}K_{0.06}Al_{0.8}Mn_{0.2}O_{3-\delta}$	14
Fe-$La_{0.92}K_{0.08}Al_{0.8}Mn_{0.2}O_{3-\delta}$	11
Fe-$La_{0.90}K_{0.10}Al_{0.8}Mn_{0.2}O_{3-\delta}$	12

The phase transformation and change in crystallite sizes of the supported materials were investigated after catalyst reduction in H_2. The reduction to the *α*-Fe phase is crucial during the catalyst activation as the iron carbide phases are formed from this phase. It is well documented in literature, that the reduction process of iron oxides under H_2 activation follows the phase transformation of *α*-Fe_2O_3 ⟶ Fe_3O_4 ⟶ FeO ⟶ *α*-Fe within a range of reduction temperatures and time on stream [194–197]. Before the FT reaction, 5 g of the supported catalysts were activated under 80 ml/min of H_2 flow at 450 °C for 15 hours, to convert the iron particles into the metallic phase.

The reduced catalysts were characterized using XRD and the results are presented in Figure 5.7. The activation of the catalysts under H_2 flow transformed the Fe_3O_4 phase into *α*-Fe, as evidenced by the presence of metallic Fe reflexes (PDF 04-007-9753) at 2θ values of 52°, 77° and 100° corresponding to the reduction steps of Fe_3O_4 ⟶ FeO ⟶ *α*-Fe. The intensity of these reflexes decreases with increasing potassium content, and this can be attributed to K restraining the reduction of the catalyst. These findings are consistent with previous research on potassium promoted iron catalysts reported in literature [98]. The observed trend may be caused by an interaction between potassium oxide and iron oxide that may inhibit the adsorption of the H_2 on the catalyst surface. This theory is supported by previous research conducted by Lund and Dumestic [198] and Rankin and Bartholomew [199].

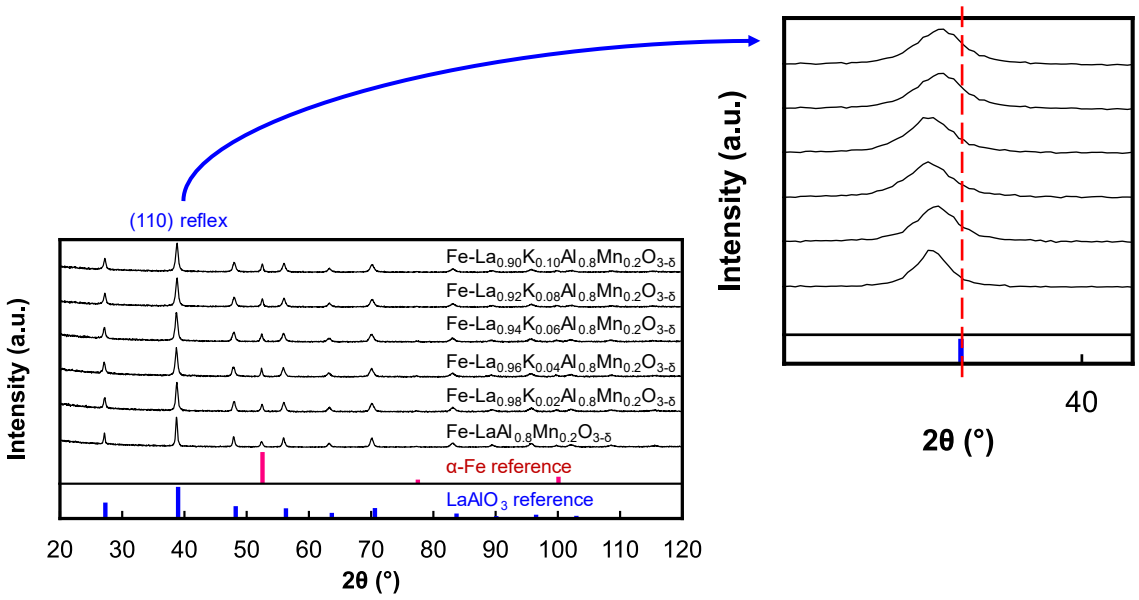

Figure 5. 7: XRD patterns of the activated Fe-$La_{1-x}K_xAl_{0.8}Mn_{0.2}O_{3-\delta}$ catalysts.

5.1.3 $La_{1-x}K_xTiO_{3-\delta}$ perovskites

The potassium substituted lanthanum titanate, $La_{1-x}K_xTiO_{3-\delta}$, where *x* is 0, 5, 10, 15, 20 and 30 atom-% were prepared via a wet chemical technique and calcined at 800 °C for 2 hours [8]. XRD analysis on the potassium doped lanthanum titanate perovskites shows different lanthanum titanate perovskites depending on the amount of K (see Figure 5.8 and 5.9). For the low K content perovskite samples (0, 5 and 10 atom-% K), the obtained XRD patterns show narrow reflexes which are characteristic of the orthorhombic lattice structure (space group, *Cmc21*) of the lanthanum titanium oxide $La_2Ti_2O_7$ (ICDD PDF-2 entry 04-021-8682).

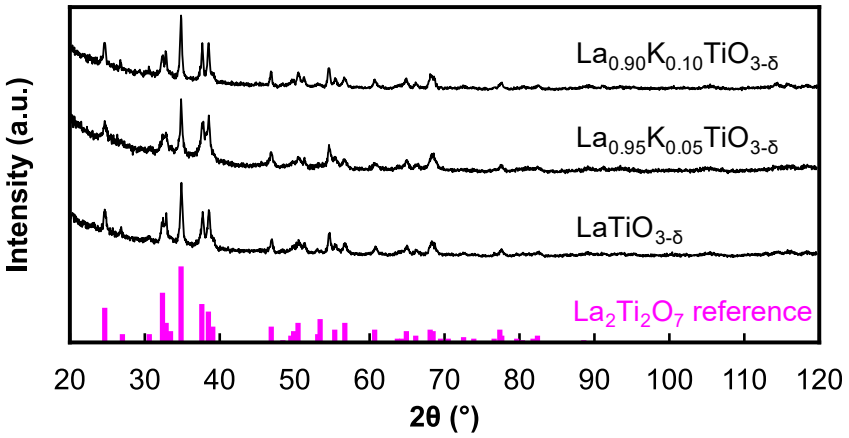

Figure 5. 8: XRD patterns of the low K content $La_{1-x}K_xTiO_{3-\delta}$ perovskites.

A change in crystal structure to cubic is observed upon an increase in K content (see Figure 5.9). At a K replacement level of 15 atom-% reflexes at 2θ values of 30° and 31° are observed in both the lower and the higher K content samples and probably residues of an incomplete phase transition. These observations are in accordance with the findings from the work of Ruiz et al. [162], who reported that alkali substitutions into the $La_{1.33-x}M_{3x}Ti_2O_6$ induce crystallographic variation, which seems to depend on the ionic size of the alkaline cations as well as their proportion in the compound. Due to the stability of Ti^{4+} as the preferred valence state, unintentional overoxidation often leads to the formation of $La_2Ti_2O_7$. Based on few works that investigated phase transitions with alkali doping in these materials, substituting alkaline cations into the structure can alleviate this issue as the alkali ions occupy the vacant A-sites and replace some of the La^{3+}, thus stabilizing the structure [157,163,200]. Ruiz et al. [162] reported that potassium substitution alters the basic symmetry of the materials and explained this phenomenon by the fact that La^{3+} ions (ionic radii 1.189 Å) are substituted by bigger K^+ ions (ionic radii 1.5 Å) in the perovskite framework [201].

The high K content materials exhibit the same space group, *Pm–3m* (221), as a reference pattern of a $La_{0.67}TiO_3$ (ICDD PDF-2 entry 04-005-5861). Increasing intensity and sharpening of the reflexes with an increase in K content is observed, which is in agreement with the work of Yamamoto et al. [164]. The authors reported that the lattice parameters of the alkali substituted perovskites decreased with an increase in alkali loading, which they linked to the small amounts of an impurity phase.

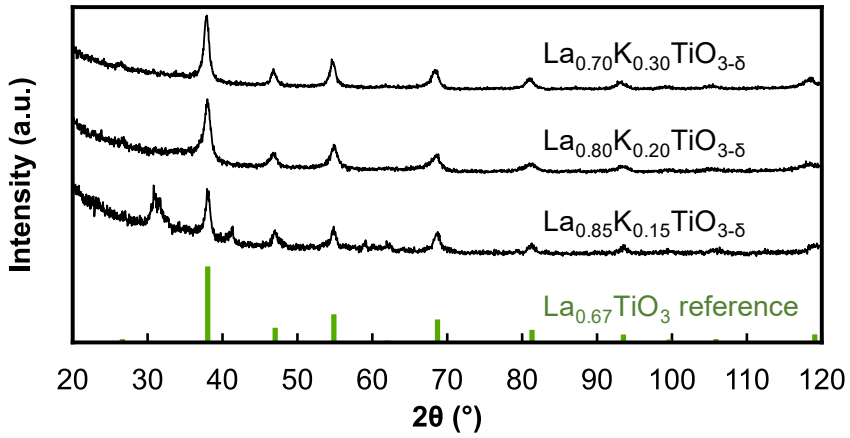

Figure 5. 9: XRD patterns of the high K content $La_{1-x}K_xTiO_{3-\delta}$ perovskites.

SEM-EDX mapping of these materials revealed that the elements (La, Ti, K and O) are evenly spread across the sample, with no significant variations in elemental composition observed.

The elements were identified, and their distribution is presented in the figures. The mapping results indicate a homogenous distribution of all elements in the samples; thus, potassium is largely trapped within the structure, restraining its mobility (Figures 5.10A – C).

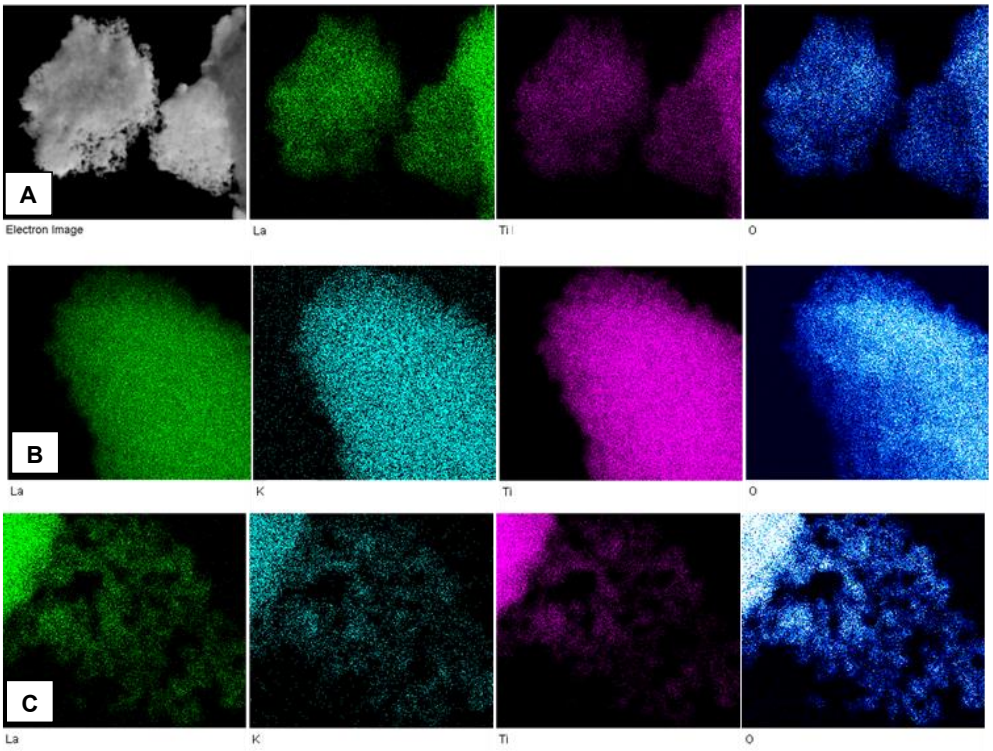

Figure 5. 10: SEM-EDX elemental mapping micrographs of $LaTiO_{3-\delta}$ (A), $La_{0.90}K_{0.10}TiO_{3-\delta}$ (B) and $La_{0.80}K_{0.20}TiO_{3-\delta}$ (C).

The elemental analysis results of the synthesized material are shown in Table 5.5 below. Similar to the citrate method used in preparing the $La_{1-x}K_xAl_{0.8}Mn_{0.2}O_{3-\delta}$ perovskites, the sol-gel method of catalyst preparation also resulted in elemental compositions in the support structures that were close to the desired values, suggesting that the sol-gel method is also a reliable method for catalyst synthesis.

Table 5. 5: Elemental composition analysis of the $La_{1-x}K_xTiO_{3-\delta}$ perovskites.

Catalyst	Targeted wt.%			ICP-OES wt.%		
	La	K	Ti	La	K	Ti
$LaTiO_{3-\delta}$	74.4	0.00	25.6	73.8	0.00	26.2
$La_{0.95}K_{0.05}TiO_{3-\delta}$	72.6	1.08	26.3	71.9	1.33	26.8
$La_{0.90}K_{0.10}TiO_{3-\delta}$	70.7	2.21	27.1	70.7	2.69	26.6
$La_{0.85}K_{0.15}TiO_{3-\delta}$	68.7	3.41	27.9	67.4	3.91	28.7
$La_{0.80}K_{0.20}TiO_{3-\delta}$	66.6	4.69	28.7	65.0	5.26	29.7
$La_{0.70}K_{0.30}TiO_{3-\delta}$	62.0	7.48	30.5	60.4	8.35	31.2

BET surface area results of the synthesized perovskites materials showed an increase in surface area with increase in potassium loading (Table 5.6). Notably, within the orthorhombic space group, the increase is small but seems to jump when shifted to cubic. The trend of the pore volume follows that of the BET surface area.

Table 5. 6: BET surface area of the synthesized $La_{1-x}K_xTiO_{3-\delta}$ perovskites.

Catalyst	BET surface area (m^2/g)	Pore volume (cm^3/g)
$LaTiO_{3-\delta}$	21	0.11
$La_{0.95}K_{0.05}TiO_{3-\delta}$	23	0.14
$La_{0.90}K_{0.10}TiO_{3-\delta}$	29	0.14
$La_{0.85}K_{0.15}TiO_{3-\delta}$	40	0.17
$La_{0.80}K_{0.20}TiO_{3-\delta}$	49	0.23
$La_{0.70}K_{0.30}TiO_{3-\delta}$	73	0.36

Iron oxide nanoparticles were supported on these perovskite structures, targeting a 16 wt.% metallic Fe loading. Results from the XRD analysis of the materials showed that within orthorhombic space group, the intensity of the reflexes decreases with an increase in K loading. There is a notable merging of the reflexes at 2θ values of 50° and 51° on the K = 10 atom- % promoted catalyst, the two reflexes on the as-synthesized materials at 2θ = 50° and 51° (Figure 5.11). The reflex at 2θ = 41° match that of the magnetite according to the database.

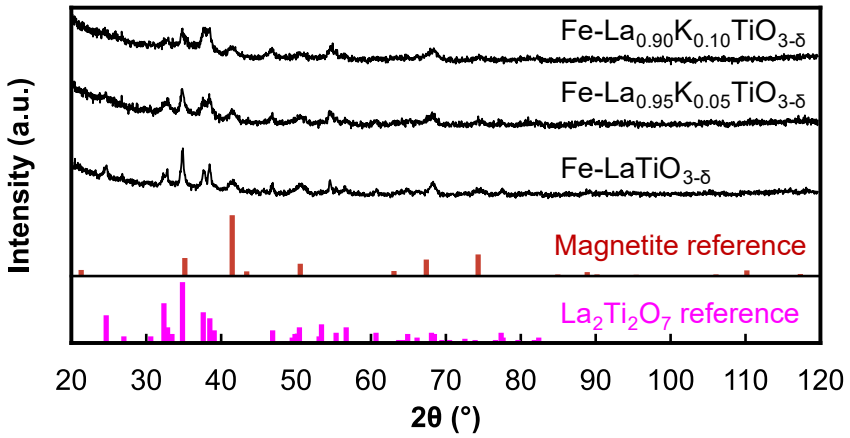

Figure 5. 11: XRD patterns of Fe_3O_4 supported low K content $La_{1-x}K_xTiO_{3-\delta}$ perovskites.

Contrary to the orthorhombic space group, within the cubic space group materials, there is a decrease in reflex intensity with increase in potassium loading (Figure 5.12).

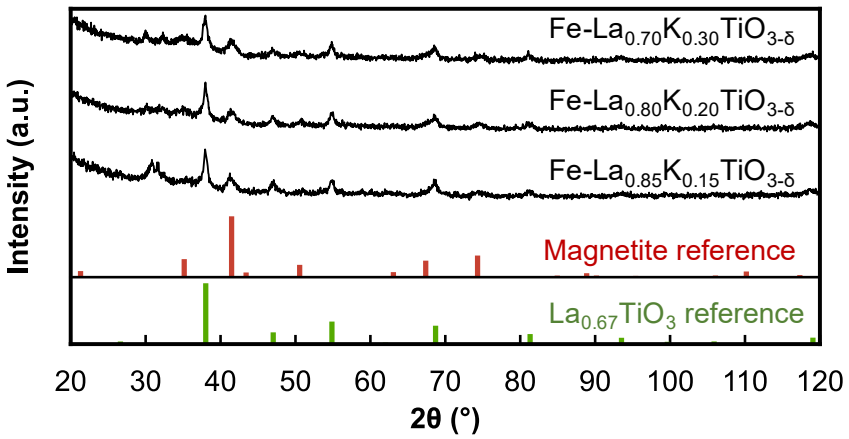

Figure 5. 12: XRD patterns of Fe_3O_4 supported high K content $La_{1-x}K_xTiO_{3-\delta}$ perovskites.

The trend in BET surface area of the materials after iron deposition shows an increase with increasing potassium content in the orthorhombic samples, similar to the $La_{1-x}K_xAl_{0.8}Mn_{0.2}O_{3-\delta}$ catalysts (Table 5.7). The increase in BET surface area is observed to be substantial, with a notable jump as potassium loading increases. Specifically, when comparing the results from lowest potassium content to those with higher potassium levels within the space groups. Pore volume shows the same trend. On the cubic samples, the surface area decreases in parallel with a decrease in pore volume, a possibility of pore blockage with Fe_3O_4 nanoparticles deposition because of different pore diameters of these structures.

Table 5. 7: Porous nature of the Fe_3O_4 supported $La_{1-x}K_xTiO_{3-\delta}$ perovskites.

Catalyst	BET surface area (m^2/g)	Pore volume (cm^3/g)
Fe-$LaTiO_{3-\delta}$	44	0.16
Fe-$La_{0.95}K_{0.05}TiO_{3-\delta}$	47	0.17
Fe-$La_{0.90}K_{0.10}TiO_{3-\delta}$	57	0.25
Fe-$La_{0.85}K_{0.15}TiO_{3-\delta}$	38	0.10
Fe-$La_{0.80}K_{0.20}TiO_{3-\delta}$	43	0.13
Fe-$La_{0.70}K_{0.30}TiO_{3-\delta}$	65	0.24

Iron oxide nanoparticle loading investigation on these revealed that the achieved metallic Fe loading was slightly lower than the targeted value of 16 wt.% metallic Fe (Table 5.8).

Table 5. 8: Iron loading in the different $La_{1-x}K_xTiO_{3-\delta}$ perovskites.

Catalyst	Iron loading (wt.%)
Fe-$LaTiO_{3-\delta}$	14
Fe-$La_{0.95}K_{0.05}TiO_{3-\delta}$	10
Fe-$La_{0.90}K_{0.10}TiO_{3-\delta}$	11
Fe-$La_{0.85}K_{0.15}TiO_{3-\delta}$	12
Fe-$La_{0.80}K_{0.20}TiO_{3-\delta}$	12
Fe-$La_{0.70}K_{0.30}TiO_{3-\delta}$	12

Activating the catalyst under H_2 flow transforms the Fe_3O_4 phase into *α*-Fe as evident from the metallic Fe reflexes (PDF 04-007-9753) at 2θ = 52°, 77° and 100° in Figure 5.13 below.

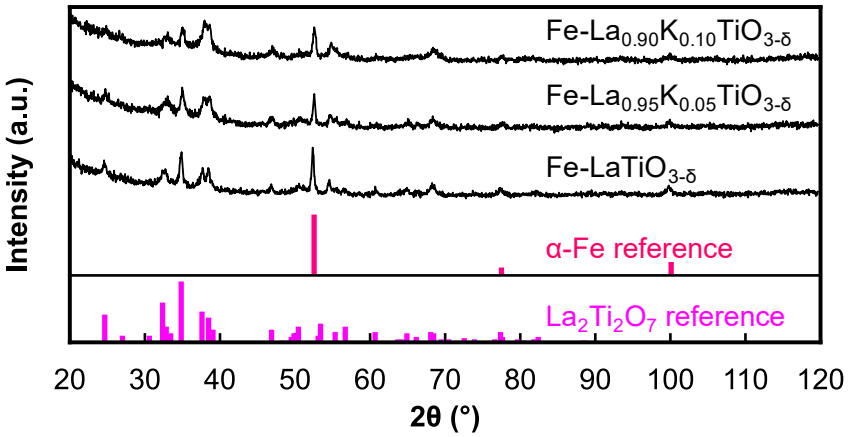

Figure 5. 13: XRD patterns of the activated low K content Fe-$La_{1-x}K_xTiO_{3-\delta}$ catalysts.

The XRD patterns of the Fe-$La_{0.85}K_{0.15}TiO_{3-\delta}$ material as shown in Figure 5.14 reveal the presence of a small amount of the oxide phase (reflex at 2θ = 41°). Despite the same reduction conditions applied for all samples, the Fe_3O_4 observed might have been a result of incomplete reduction of the nanoparticles.

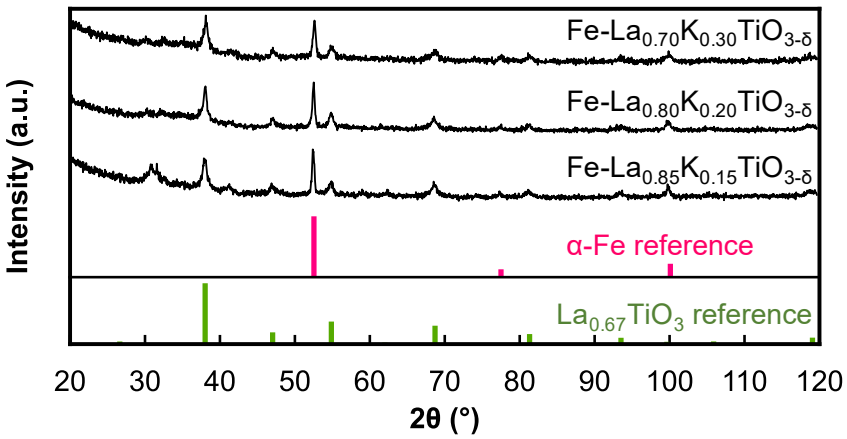

Figure 5. 14: XRD patterns of the activated high K content Fe-$La_{1-x}K_xTiO_{3-\delta}$ catalysts.

5.2 Characterization of spent catalysts

After 48 hours under FT conditions, about 3 g of the spent catalysts were obtained and separated from the wax using hexane. The samples were left to dry in the air at room temperature overnight. More information on the process can be found in Chapter 4.5.5.

5.2.1 Fe-$La_{1-x}K_xAl_{0.8}Mn_{0.2}O_{3-\delta}$ spent catalysts

XRD analysis of the Fe-$La_{1-x}K_xAl_{0.8}Mn_{0.2}O_{3-\delta}$ spent catalyst after FT synthesis indicated the XRD reflexes at 2θ values of 27°, 38°, 47°, 55°, 63°, 70° and 83° that correspond to the cubic $LaAlO_3$ perovskite structure (Figure 5.15). This observation indicated that the perovskite structure is stable under the FT reaction conditions. The reflexes around a 2θ of 52° are identified as the iron carbide phase (Fe_7C_3 PDF-00-017-0333) (Figure 5.11). Fe_3O_4 phase is also present, as indicated by the reflexes at 41°, supporting the claim that during FT synthesis, different forms of iron oxides and iron carbides may co-exist [202,203]. The authors reported that the iron carbides may oxidize in the presence of H_2O formed during FT, to form Fe_3O_4. In his work, Khasu [20] also reported observing these phases. The oxide phase may also had been formed post-run when the catalyst oxidized during catalyst recovery. Due to the reactor system we were working with, it was quite challenging to determine at what stage exactly did the oxide phase form.

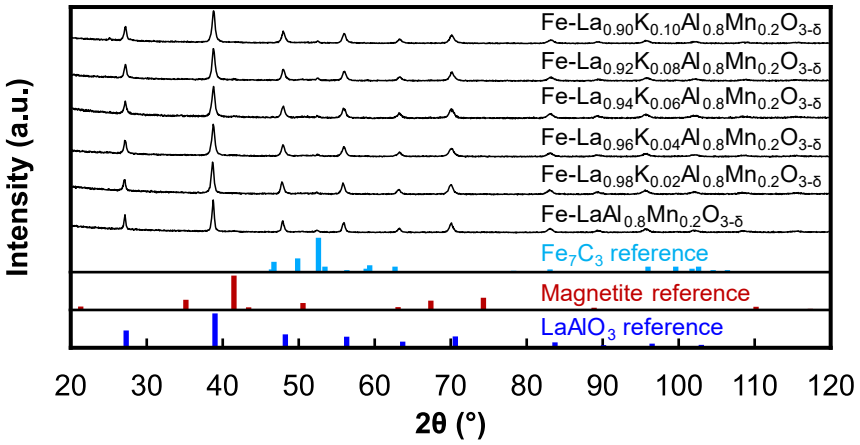

Figure 5. 15: XRD patterns of the Fe-$La_{1-x}K_xAl_{0.8}Mn_{0.2}O_{3-\delta}$ spent catalysts.

An elemental analysis of the spent catalysts was performed to determine if potassium had leached out of samples during FT synthesis. The mobility of the potassium promoter during FT synthesis poses a challenge as it creates a highly dynamic system, resulting in active sites blockage and consequently, catalyst deactivation. The results, presented in Table 5.9, suggest that no significant leaching of K ions occurred. Furthermore, by comparing the La/K ratios of the fresh and spent catalysts, it can be concluded that no leaching occurred (Table 4.5 in the Appendix).

Table 5. 9: Elemental composition analysis of the Fe-$La_{1-x}K_xAl_{0.8}Mn_{0.2}O_{3-\delta}$ spent catalysts.

	ICP-OES wt.%				
Catalyst	**La**	**K**	**Al**	**Mn**	**Fe**
Fe-$LaAl_{0.8}Mn_{0.2}O_3$	84.4	0.15	8.57	6.86	11.8
Fe-$La_{0.98}K_{0.02}Al_{0.8}Mn_{0.2}O_3$	81.8	0.47	10.9	6.85	9.80
Fe-$La_{0.96}K_{0.04}$ $Al_{0.8}Mn_{0.2}O_3$	82.9	0.70	9.49	6.84	10.7
Fe-$La_{0.94}K_{0.06}Al_{0.8}Mn_{0.2}O_3$	81.8	0.86	10.6	6.76	11.6
Fe-$La_{0.92}K_{0.08}Al_{0.8}Mn_{0.2}O_3$	82.1	1.13	9.62	7.12	11.6
Fe-$La_{0.9}K_{0.1}Al_{0.8}Mn_{0.2}O_3$	81.2	2.09	9.40	7.34	10.8

5.2.2 Fe-$La_{1-x}K_xTiO_{3-\delta}$ spent catalysts

Phase analysis on the recovered Fe-$La_{1-x}K_xTiO_{3-\delta}$ spent catalysts after 48-hours of FT synthesis showed that both the orthorhombic and cubic space group materials are stable under FT conditions (Figure 5.16). On the unpromoted catalyst, the reflexes at 2θ = 41° match that of the magnetite reference according to the database. The reflexes at 2θ = 52° match that of the Fe_7C_3 phase and they become more defined with an increase in K content in the perovskites. In these samples, the Fe_2C phase (PDF 00-036-1249) is also present as evident by the reflexes at 50°.

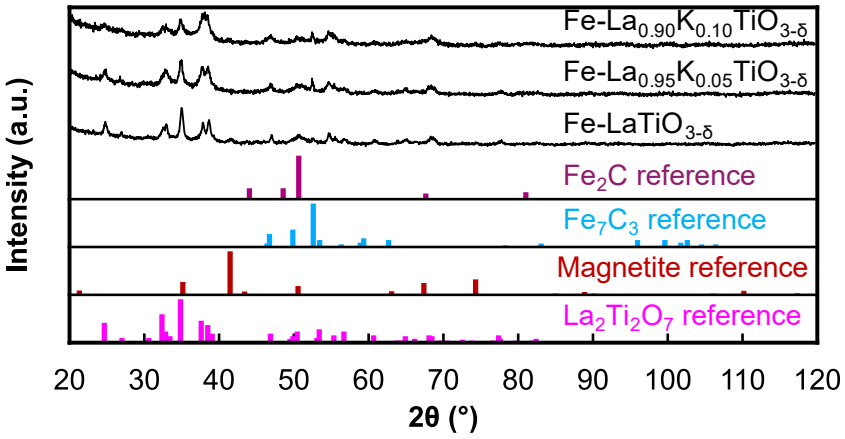

Figure 5. 16: XRD patterns of the low K content Fe-$La_{1-x}K_xTiO_{3-\delta}$ spent catalysts.

The presence of the Fe_3O_4 in the high K content catalysts is more pronounced compared to the low K content materials as evident by the more defined reflexes at 2θ = 41° (Figure 5.17). The presence of the Fe_2C carbides in these samples is lower than in the orthorhombic catalysts. The observed trend may be ascribed to the low FT activity in these catalysts.

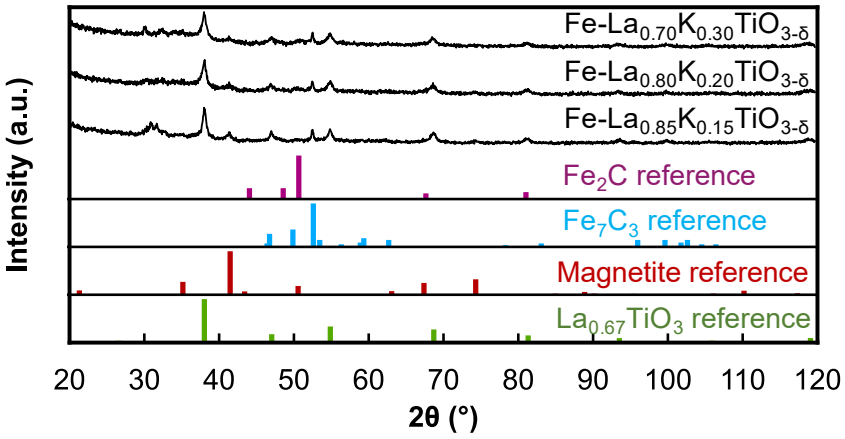

Figure 5. 17: XRD patterns of the high K content Fe-$La_{1-x}K_xTiO_{3-\delta}$ spent catalysts.

There was minimal K leaching as is evident in Table 5.10. CO conversion vs TOS results (Figure 5.28) also support this claim as there is no catalyst deactivation caused by the mobility of the K ions during the 48 hours FT experiment. The La/K ratio in the spent catalysts in comparison to the fresh catalysts further supports this claim (Table A.5 in the Appendix).

Table 5. 10: Elemental composition analysis of the Fe-$La_{1-x}K_xTiO_{3-\delta}$ spent catalysts.

	ICP- OES wt.%			
Catalyst	**La**	**K**	**Ti**	**Fe**
Fe-$LaTiO_{3-\delta}$	74.1	0.00	25.9	12.3
Fe-$La_{0.95}K_{0.05}TiO_{3-\delta}$	72.5	1.23	26.3	11.6
Fe-$La_{0.90}K_{0.10}TiO_{3-\delta}$	70.2	2.43	27.4	10.9
Fe-$La_{0.85}K_{0.15}TiO_{3-\delta}$	54.5	3.07	42.4	13.4
Fe-$La_{0.80}K_{0.20}TiO_{3-\delta}$	52.7	4.17	43.2	12.7
Fe-$La_{0.70}K_{0.30}TiO_{3-\delta}$	47.8	6.39	45.8	11.7

5.3 Effects of potassium promotion on Fe-based FT activity and selectivity

The effect of potassium as a promoter for iron-based FT has been widely explored in literature [101–104]. In this study, FT testing of K promoted iron-based catalysts was conducted at 240 °C, 15 bar and a synthesis gas ratio $H_2/CO = 2$ in a 0.6 L continuously stirred tank reactor. The permanent gases including methane were analyzed using the gas chromatograph (GC) equipped with a thermal conductivity detector (TCD), while the light hydrocarbons were sampled using the ampoule technique [189] and analyzed using a Varian GC 3900 gas chromatograph equipped with a flame ionization detector (FID).

5.3.1 Fe-$La_{1-x}K_xAl_{0.8}Mn_{0.2}O_{3-\delta}$ catalysts

It is generally accepted that K promotion on Fe based catalyst improves the dissociative adsorption of CO on the Fe surface and enhances the carburization of these catalysts. Zhang et al. [204] came to the conclusion that K promotion also increases the number of surface C species and increases the CO conversion in iron-based catalysts.

Potassium promoted catalysts show higher activities compared with the unpromoted catalyst. This is in line with reports on classic potassium promotion [97,98,192,205]. The CO conversions over

time on stream (TOS) are shown in Figure 5.18. All catalysts show an initial formation period approaching stability after around 10 hours TOS. The results show that the CO conversion continues to increase slightly from 24 to 48-hours of TOS. Apart from potassium promotion, a higher metallic Fe loading will also increase the number of active sites available for FT reaction, leading to a higher CO conversion. As such, it is assumed that the same CO conversions on the 2 and 4 atom-% K promoted catalysts are a result of the lower iron loading in the 4 atom-% K promoted catalyst (see Table 5.4). On the other hand, even though the 8 atom-% K promoted catalyst had a lower iron loading than the 6 atom-% K promoted catalyst, it is assumed that the higher CO conversion may have been compensated for by the higher potassium content. Additionally, these results indicate that the catalysts are still active and stable after 48 hours TOS.

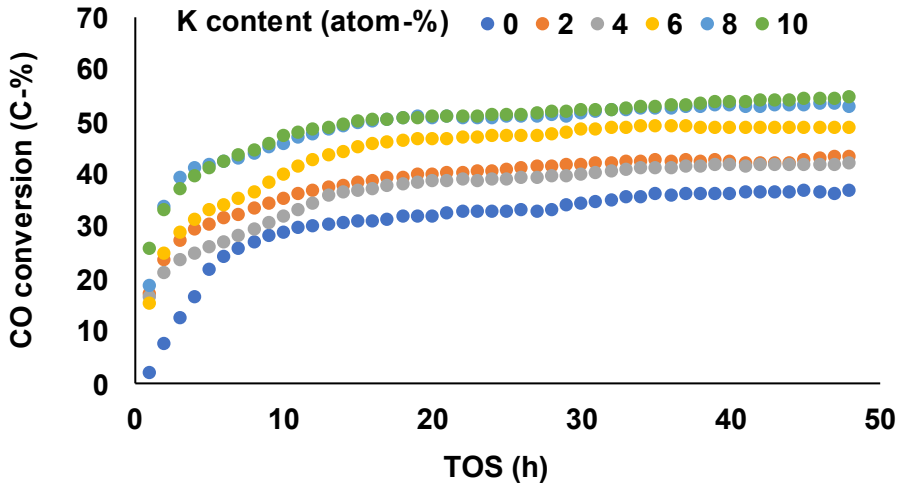

Figure 5. 18: CO conversion on Fe-$La_{1-x}K_xAl_{0.8}Mn_{0.2}O_{3-\delta}$ catalysts as a function of time on stream.

The conversion results were summarized into 24 and 48-hours of TOS (Figure 5.19). On the unpromoted catalyst, the CO conversion increases from 33 C-% to 37 C-%. The promoted catalysts, with varying K loadings, also exhibit an increase in CO conversion over the same time period. There is an increase CO conversion with an increase in K loading, with the highest conversion of 54 % after 48-hours of TOS, observed for the catalyst with 10 atom-% K loading. The conversion on the 10 atom-% potassium loading is similar to the conversion reported by Khasu [20], who reported a conversion of 39 C-% at the end of a 48-hours of FT synthesis. The observed higher activity on the potassium promoted catalyst can be linked to the enhanced formation of iron carbide phases in these catalysts, which have been widely reported in literature as the active phases for FT [88,90,99,206,207]. It is reported that potassium improves carburization of the iron catalysts through a donation of electron density from the potassium

metal to the iron phase, enhancing CO over H_2 adsorption and weakening the C-O bond, hence the increased CO conversion on promoted catalysts.

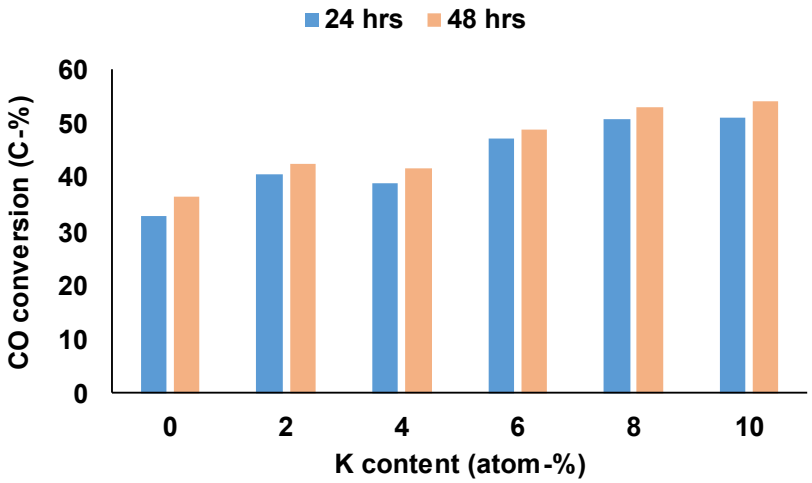

Figure 5. 19: CO conversion on Fe-$La_{1-x}K_xAl_{0.8}Mn_{0.2}O_{3-\delta}$ catalysts over 24 and 48-hours TOS.

In studying the role of potassium promotion in the reduction behavior of maghemite, Khasu [20] demonstrated using *in situ* XRD that the potassium promotion led to an increase in the reduction temperature from γ-Fe_2O_3 to Fe_3O_4 in comparison to a sample without a promoter. This increase was attributed to a weaker hydrogen chemisorption in the presence of Mn. However, he reported that the reduction of Fe_3O_4 to α-Fe was not affected. Under FT conditions, the rate of carburization was significantly enhanced, as evident by a complete conversion of metallic Fe to Hägg carbide in only 20 minutes, compared to the 40 minutes in the unpromoted catalyst.

Iron-based FT catalysts are well known to be active for the WGS reaction especially at low H/CO feed ratios [3,208,209]. Since the formation of CO_2 via the WGS activity occurs as a secondary reaction of FT, an increased formation of H_2O in the FT synthesis through higher conversions may increase the formation of CO_2 via the WGS reaction.

The WGS activity in the promoter free catalyst results in a CO_2 selectivity of about 38 C-% after 48-hours of FT reaction (Figure 5.20). At low levels of potassium promotion, 2 and 4 atom-% K, the CO_2 selectivity is reduced compared with the unpromoted catalyst. Specifically, the CO_2 selectivity decreases to 35 C-% after 48-hours of TOS for the 2 atom-% K promoted catalyst and 37 C-% on the 4 atom-% K promoted catalyst. However, with increasing potassium loading, up to 8 atom- %, the CO_2 selectivity increases surpassing that of the

unpromoted sample. For the sample with the highest K loading, the WGS activity seems to drop slightly. Currently no explanation is available for this behavior. Our results show higher CO_2 selectivity compared to those reported by Khasu [20]. In particular, the author reported a CO_2 selectivity of 9 C-% on the unpromoted catalysts, and 12 C-% on the 10 atom-% K promoted catalyst. This discrepancy in results may be due to variations in the nanoparticles preparation methods, or variations in the catalyst compositions or properties. Contrary to our 8 nm Fe_3O_4 nanoparticles, the author used a co-precipitation method to prepare Fe_2O_3 nanoparticles of around 22 nm. Smaller particle sizes lead to increased surface area and higher catalytic activity, hence our higher WGS activity.

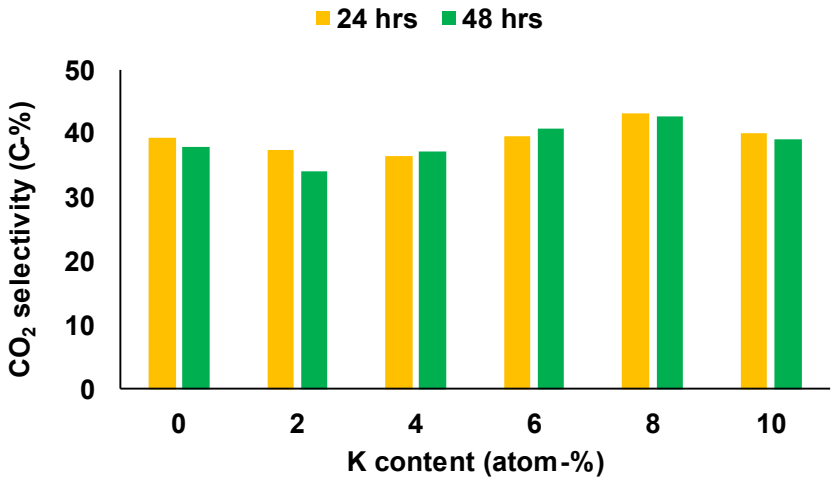

Figure 5. 20: CO_2 selectivity on Fe-$La_{1-x}K_xAl_{0.8}Mn_{0.2}O_{3-\delta}$ catalysts.

Even though methane is the thermodynamically most stable FT hydrocarbon product, it is industrially undesirable [193,210,211]. Methane is formed via the complete hydrogenation of surface C species [212]. Its selectivity is influenced by the water-gas shift activity and potassium promotion [208]. Potassium is known to promote the WGS activity on iron catalysts by increasing the adsorption and activation of reactants on the catalytic surface. It is reported that the increased WGS activity in turn results in an increased H_2/CO ratio enhancing hydrogenation.

Incorporation of potassium in these catalysts results in a significant decrease in methane selectivity from about 6 C-% for the unpromoted catalyst to around 3 C-% (Figure 5.21). These results are consistent with previous studies in literature. For example, Khasu [20] reported a decrease in CH_4 selectivity with potassium promotion in the catalysts. Steynberg et al. [213] also reported methane selectivity of 7 C-% in unpromoted catalyst, which decreased to 3 C-% in all the potassium promoted catalysts. While the differences with potassium loading are minor,

the observed trend, peaking at 8 atom-% K, matches the observed WGS activity and could therefore be a result of a localized increase in H/CO ratio.

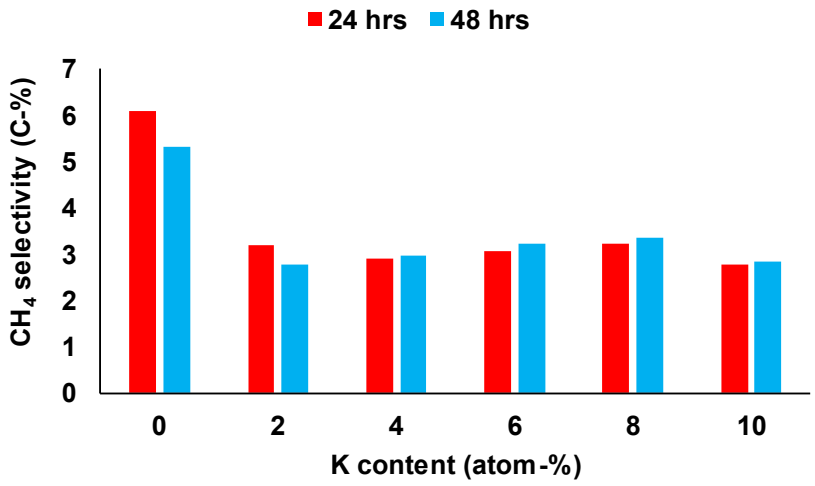

Figure 5. 21: Methane selectivity on Fe-$La_{1-x}K_xAl_{0.8}Mn_{0.2}O_{3-\delta}$ catalysts.

The minimal change of methane selectivity with changing K loading was also observed by Yang et al. [98] who report that the methane selectivity was similar for all promoted catalysts studied at low CO conversions (< 50 %) independent of the amount of K loading. On a potassium promoted precipitated iron-silica catalyst, Raje et al. [192] found that the methane selectivity was constant at 5 – 6 C-% for a low alpha catalyst and similar for all the catalysts studied at CO conversions of less than 50 %. However, at CO conversion above 50 C-%, as the amount of potassium in the catalyst increased, methane selectivity decreased.

Furthermore, research has shown that impregnation of K can suppress the formation of methane by blocking the fast formation channel and by establishing a new and slower reaction pathway [214]. The fast formation channels refer to the direct reaction between CO and H_2 to produce CH_4. Potassium is thought to block this process by adsorbing on the catalytic surface and inhibiting the reaction, resulting in a decreased methane formation. Graf et al. [214], concluded that this happens without changing the reaction pathway towards higher hydrocarbons.

The production of hydrocarbons can be used as performance indicator of the FT catalyst. It is widely accepted that K promotion on iron-based FT catalyst leads to suppression of H_2 adsorption which leads to a higher C/H ratio on the catalyst's surface and weakens the

hydrogenation capability of catalysts, thus promoting the chain growth reaction and formation of olefins [29,102,202,211].

In the present study, potassium promotion has a significant effect on the selectivity towards the different hydrocarbon products (Figure 5.22). On the unpromoted catalyst, the selectivity of the largely undesired $C_2 – C_4$ hydrocarbons is found to be 17 C-%, while that of the desired C_{5+} hydrocarbons are 37 C-% and oxygenates constituted 3 C-%. However, on the promoted catalysts, the selectivity of the $C_2 – C_4$ hydrocarbons decrease with K promotion, while the selectivity of C_{5+} hydrocarbons increase slightly. On the other hand, potassium promotion reduces the selectivity to oxygenates.

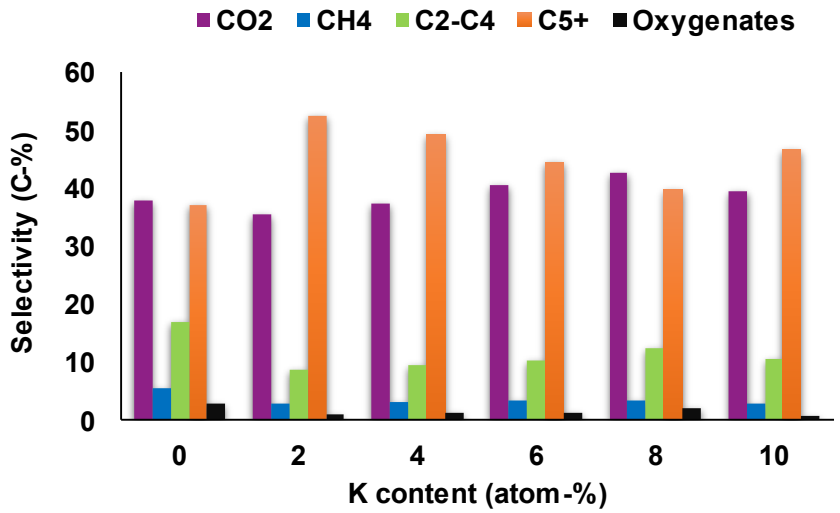

Figure 5. 22: Hydrocarbon selectivity after 48 hours under FT conditions on Fe-$La_{1-x}K_xAl_{0.8}Mn_{0.2}O_{3-\delta}$ catalysts.

To get a clearer picture of the performance of these catalysts eliminating the influence of CO_2, the selectivity to the hydrocarbons was normalized (Figure 5.23). While all promoted samples have a decreased $C_2 – C_4$ and oxygenate selectivity compared to the unpromoted reference, it is evident that the lowest concentration of potassium has the highest impact on the selectivity enhancing the formation of long-chained product. This is parallel to the previously described suppression of the WGS reaction. With increasing potassium loading the hydrocarbon composition approaches that of the unsupported sample, with the 10-atom% potassium sample again representing an outlier to this trend.

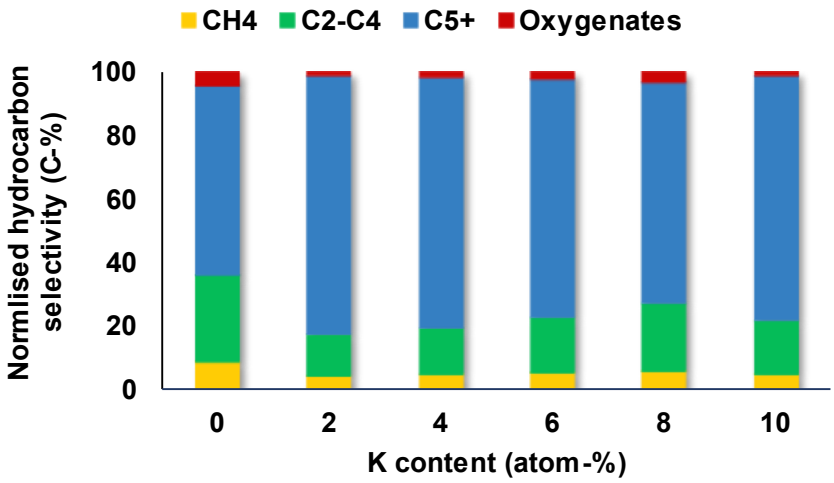

Figure 5. 23: Normalized selectivity to organic products for Fe-$La_{1-x}K_xAl_{0.8}Mn_{0.2}O_{3-\delta}$ catalysts.

The FT product distribution on iron catalysts were previously found to follow a modified ASF distribution with two chain growth probabilities [57,215,216]. This distribution is sometimes termed double α and it suggests that two independent chain growth mechanisms contribute to the overall product distribution with the second higher α from approximately C_{10} onwards. Gaube et al. [216] concluded that only a certain fraction of the active sites is influenced by the alkali promoter. They postulated that these sites are of a certain structure and support higher chain growth probability whereas the remaining sites lead to the same growth probability as those on unpromoted iron catalysts. Some authors have attributed the secondary chain growth probability to chain length-dependent solubility of olefins in the wax [54,56,59,60]. As the carbon number increases, the solubility of olefins in the wax also increases exponentially and is more strongly dependent in the carbon number. Schulz and Claeys [60] noted that the phase in which products leave the reactor shifted from gas to the liquid phase with an increase in carbon number. They proposed that the removal of large hydrocarbons in the wax leads to much longer residence times, reflecting the greater solubility of larger hydrocarbons. While the second chain growth probability was not directly measured in the present study, the carbon balance is only closed if such a secondary α is present.

A summary of the first chain growth probabilities (α1, for C_3 – C_7) for the different Fe- $La_{1-x}K_xAl_{0.8}Mn_{0.2}O_{3-\delta}$ catalysts is shown in Table 5.11 below. The results show that K promotion on the Fe-$La_{1-x}K_xAl_{0.8}Mn_{0.2}O_{3-\delta}$ has no effect on the alpha value which is about 0.60 in all cases. Due to the chosen technique of sample collection and analysis, the C_{7+} fraction underwent partial condensation in the glass ampoule before injection into the gas chromatograph. Therefore, a secondary higher alpha could not be recorded experimentally.

The calculated second alpha was 0.91 on the unpromoted catalyst and remained constant at an elevated 0.96 in the promoted catalyst. Figure A.4 in the Appendix shows ASF plots for $\alpha 1$ linear paraffins and olefins (C_3 – C_7) for these catalysts.

Table 5. 11: Chain growth probability of linear hydrocarbons on Fe-$La_{1-x}K_xAl_{0.8}Mn_{0.2}O_{3-\delta}$ catalysts.

Catalyst	α1 linear paraffins and olefins (C_3 – C_7)
Fe-$LaAl_{0.8}Mn_{0.2}O_{3-\delta}$	0.60
Fe-$La_{0.98}K_{0.02}Al_{0.8}Mn_{0.2}O_{3-\delta}$	0.60
Fe-$La_{0.96}K_{0.04}Al_{0.8}Mn_{0.2}O_{3-\delta}$	0.61
Fe-$La_{0.94}K_{0.06}Al_{0.8}Mn_{0.2}O_{3-\delta}$	0.56
Fe-$La_{0.92}K_{0.08}Al_{0.8}Mn_{0.2}O_{3-\delta}$	0.61
Fe-$La_{0.9}K_{0.1}Al_{0.8}Mn_{0.2}O_{3-\delta}$	0.62

It is reported that chain length affects the olefin/paraffin (O/P) ratio through differences in re-adsorption that, in turn, affect secondary reactions such as hydrogenation, isomerization and re-initiation of chain growth [54,106,217,218]. The O/P ratio is a measure of the proportion of olefinic to paraffinic hydrocarbons in sample of hydrocarbons. This ratio is often used to provide insight into the performance of the catalyst. For FT catalysts, a decrease in the O/P ratio with chain length is observed, except for the C_2 fraction [48]. Through the reduction of hydrogen concentration of the catalyst surface, potassium promotion is usually reported to increase the olefin content, suppressing secondary hydrogenation reactions.

The results presented herein show that the O/P ratios are lower on the unpromoted catalyst compared to the K promoted catalysts (Figure 5.24). The results show that the O/P ratio increases with increasing K content in the catalysts with the characteristic decrease with increasing carbon number within each set of data. This is because at higher C number, there is a slower removal of the α-olefins due to the decrease of diffusion coefficients with increasing chain length [33]. As the heavier molecules are less volatile than the lighter molecules, they are more likely to remain on the catalyst surface. This increased residence time enhances secondary reaction such as hydrogenation of primarily formed olefins to paraffins [217,219].

In the studied samples, an increase in K loading increases the O/P ratio in all carbon fractions. The effect of promotion is most prominent in the C_2 fraction. Usually associated with high activity and lowest O/P ratio, the C_2 O/P ratio of the promoted catalysts is about 0.74 compared to around 3 on the unpromoted samples.

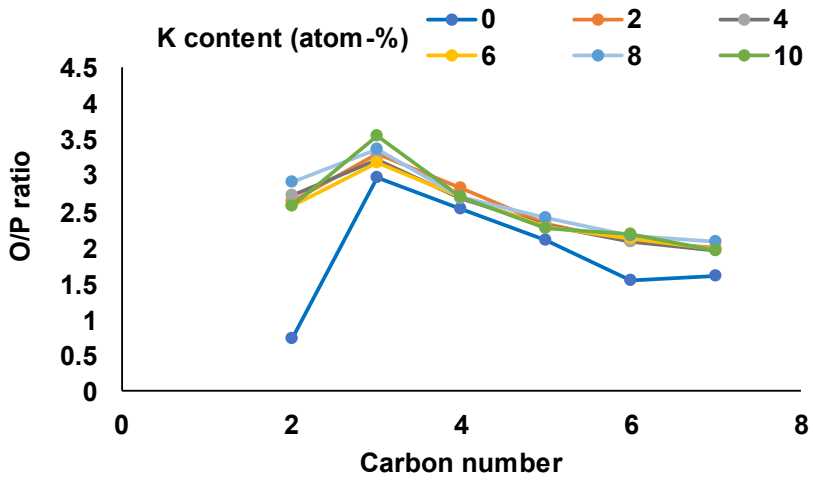

Figure 5. 24: Ratio of Olefins/Paraffins on Fe-$La_{1-x}K_xAl_{0.8}Mn_{0.2}O_{3-\delta}$ catalysts.

Of the observed olefins the vast majority are primary α-olefins. The potassium promotion seems to have suppressed most of the olefin isomerization activity evident in the unpromoted catalyst. (Figure 5.25). Within the promoted samples, there is no clear trend on how the potassium content suppresses the isomerization.

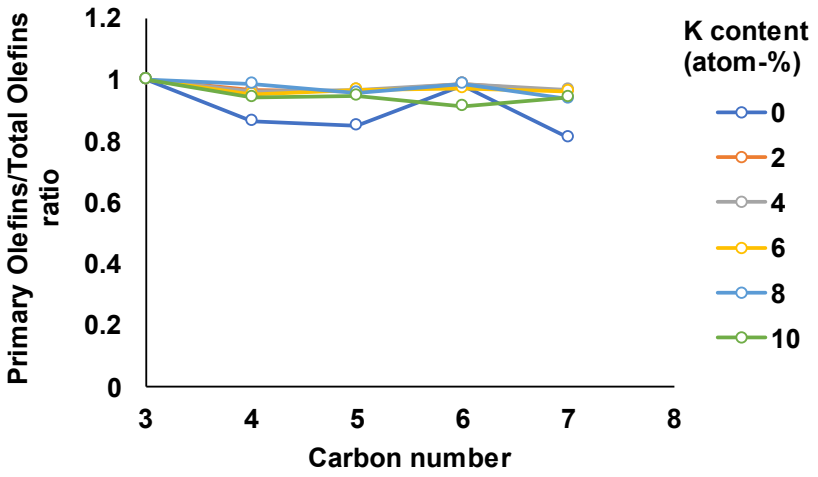

Figure 5. 25: Ratio of primary olefins/total olefins on Fe-$La_{1-x}K_xAl_{0.8}Mn_{0.2}O_{3-\delta}$ catalysts.

Despite the low selectivity of oxygenates compared to the other organic products, it was important to investigate how the specific oxygenate product classes changed with potassium promotion. Oxygenates are considered to be high-value products in the FT synthesis process due to their industrial applications but are formed in low concentrations [33].

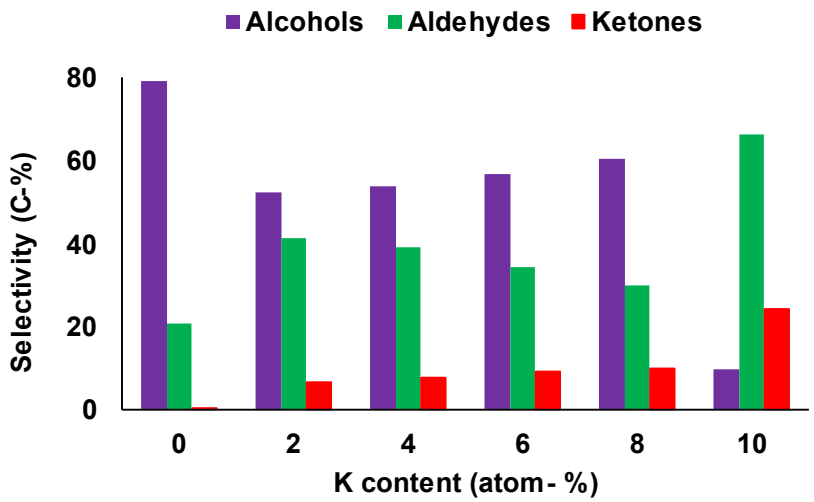

Figure 5. 26: Alcohol, aldehyde, and ketone selectivity within the oxygenate fraction on Fe-$La_{1-x}K_xAl_{0.8}Mn_{0.2}O_{3-\delta}$ catalysts.

The results show that the major group of oxygenates produced on both the unpromoted and promoted catalysts was alcohols. As illustrated in Figure 5.26 above, alcohol production is higher in the unpromoted catalyst and decreases significantly upon promotion. However, with increasing potassium levels, the selectivity to alcohol increases up to 8 atom- % K catalyst. Indeed, while deviations in CO_2, CH_4 and hydrocarbon selectivity have been described previously for this sample, the deviation in the oxygenate composition is the most prominent one, probably due to the overall low concentration of oxygenates in the product. Aldehydes show the reverse trend to the alcohol fraction. Promotion increases the aldehyde concentration overall, gradually decreasing with increasing potassium concentration. Promotion also increases the concentration of ketones, but for this product class the concentration keeps increasing with potassium content.

A close look at the oxygenate selectivity as a function of carbon number has revealed that in the absence of potassium, mostly C_3 – C_4 oxygenates are formed (Figure 5.27). Methanol formation decreased with potassium promotion and there is no clear trend within the potassium promoted catalysts. On the other hand, there is a shift in selectivity to C_2 oxygenates, with an increase in potassium loading. The C_2 selectivity peaked at 8 atom-% K loading.

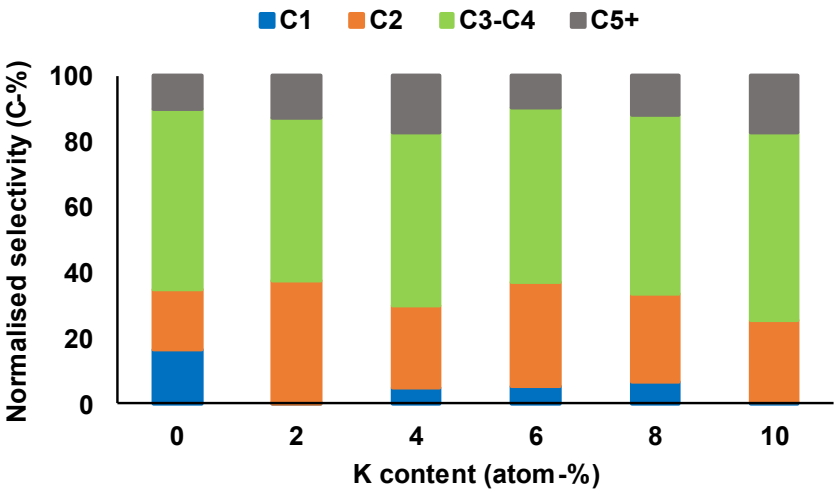

Figure 5. 27: Oxygenates selectivity as a function of carbon number on Fe-$La_{1-x}K_xAl_{0.8}Mn_{0.2}O_{3-\delta}$ catalysts.

The presented findings are on the effect of potassium promotion on the FT activity of supported iron catalyst on $La_{1-x}K_xAl_{0.8}Mn_{0.2}O_{3-\delta}$ perovskites where x = 0, 2, 4, 6, 8 and 10 atom-%. Potassium promotion on Fe-$La_{1-x}K_xAl_{0.8}Mn_{0.2}O_{3-\delta}$ improved the CO dissociation adsorption of the Fe surface, which enhanced the carburization of these catalysts. This in turn, resulted in higher activities in the potassium containing catalysts compared to the unpromoted catalyst. The CO conversion on the unpromoted catalyst after 48-hours TOS was 37 C-%. With an increase in potassium loading, the conversion increased and reached 54 C-% for the 10 atom-% potassium promoted catalyst. Potassium promotion enhanced the WGS activity as evident by the higher CO_2 formation in the promoted catalysts compared to the unpromoted catalyst. The CO_2 formation increased with increasing potassium concentration in the catalysts, peaking for the 8 atom-% promoted catalyst. Furthermore, incorporation of potassium in these catalysts resulted in a significant suppression of methane selectivity from about 6 C-% on the unpromoted catalyst to around 3 C-% on the promoted catalyst. However, hardly any difference was observed in varying the potassium loading.

Potassium promotion also has a significant effect on the selectivity of the different hydrocarbon products. The selectivity of the C_2 – C_4 hydrocarbons and oxygenates decreased with potassium promotion, while the selectivity to C_{5+} hydrocarbons increased. Additionally, an increase in K loading increased the O/P ratio in all carbon fractions. Of the observed olefins the vast majority are primary α-olefins. The potassium promotion seems to have suppressed most of the olefin isomerization activity evident in the unpromoted catalyst. While the overall selectivity to oxygenates decreased with potassium promotion, within the oxygenate fraction,

the alcohol selectivity increased with potassium concentration, and the aldehyde and ketone fractions decreased. The sample with the highest promotion levels again represents an exception to this trend.

5.3.2 Fe-$La_{1-x}K_xTiO_{3-\delta}$ catalysts

Potassium substituted lanthanum titanates were tested for FT activity and the CO conversion results are shown in Figure 5.28. The data presented illustrates the effect of TOS on the CO conversion for the different potassium loadings. The CO conversion increases rapidly in the initial 5 to 6 hours for all catalysts. After this period the unpromoted and the sample with 10 atom-% K promotion are the most active, followed by the 5 and 15 atom-% and the 20 and 30 atom-% samples. Following this initial formation period, the unpromoted sample remains mostly stable, while the promoted samples continue to show a steady increase in activity for the duration of the experiment. After 48-hours of TOS, all promoted catalysts outperform the unpromoted sample with the initial order of activity remaining unchanged. We found that the promoted samples remain stable after 90-hours of TOS (Figure A.1 in the Appendix). Within the orthorhombic structures (0, 5 and 10 atom-% potassium), the CO conversion after 48-hours of TOS increased with increasing potassium content in the samples. On the contrary, increase in potassium content resulted in a decrease in CO conversion within the cubic structures. The latter might be related to the previously observed pore blockage during iron oxide nanoparticle deposition on the cubic structures.

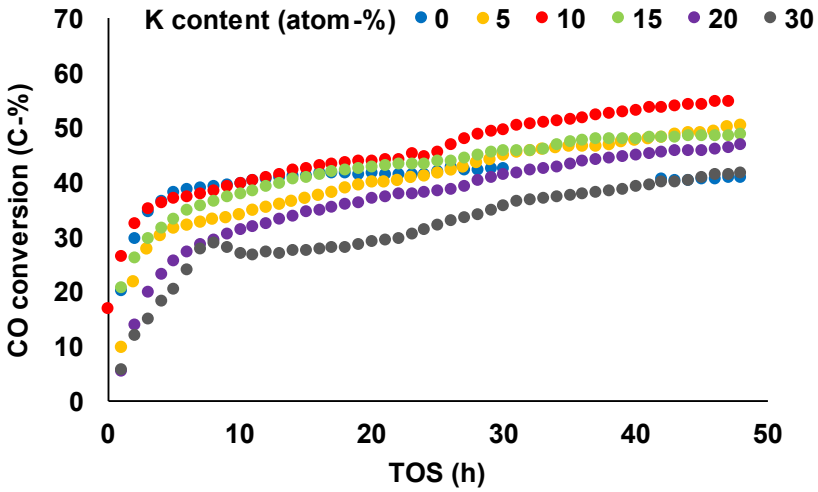

Figure 5. 28: CO conversion on Fe-$La_{1-x}K_xTiO_{3-\delta}$ catalysts as a function of time on stream.

The CO conversion results were summarized after 24 and 48-hours TOS (Figure 5.29). The CO conversion on the unpromoted sample is higher (41 C-%) in comparison with the lanthanum aluminate catalyst without potassium promotion. With potassium promotion, the CO conversion peaks at 55 C-% for the catalyst with 10 atom-% potassium which is comparable to the highest conversion in the Fe-$La_{1-x}K_xAl_{0.8}Mn_{0.2}O_{3-\delta}$ sample family. However, as the potassium content in the samples increases, the CO conversion decreases to 42 C-% at the highest potassium loading. Based on the results, it seems that the optimum potassium loading for the titanate materials is 10 atom-%, which forms an orthorhombic crystal phase.

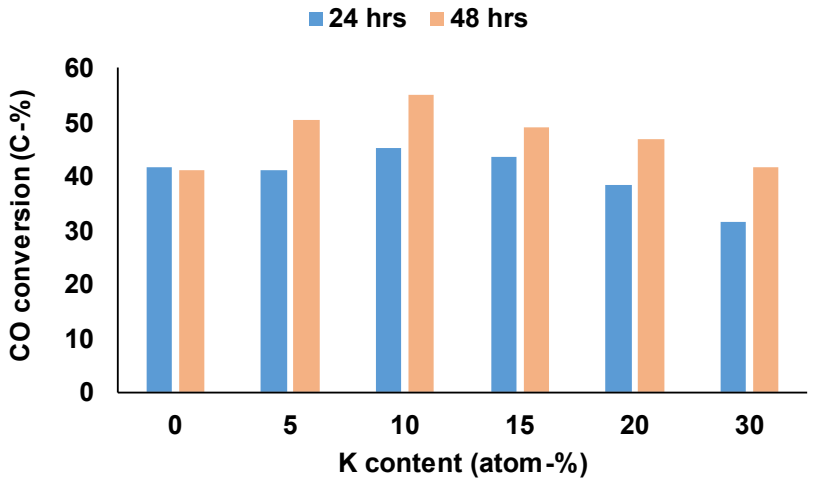

Figure 5. 29: CO conversion on Fe-$La_{1-x}K_xTiO_{3-\delta}$ catalysts over 24 and 48-hours FT time on stream.

The results seem to suggest that a maximum loading to potassium in the perovskite sample exists, above which no further activity increase is achieved. A similar trend has previously been observed on iron-based catalysts with classic potassium promotion [105,220]. Lohitharn and Goodwin [105] reported that promotion of iron catalyst with small amount of potassium improved their catalysts. However, as the amount of potassium loading increases beyond a certain point, the activity of the catalysts decreases which is associated with coverage effects either by the alkali itself or by carbon deposits.

The observed prolonged induction period on potassium-promoted catalysts is inconsistent to the findings in literature about the effect of potassium promotion. Potassium promotion is known to enhance formation of iron carbides, as such, it is expected that potassium promoted catalyst will reach stability much quicker than unpromoted samples [1,4,33].

To gain further insight into the reduction and formation of the iron oxide on the perovskite supports and to investigate the effect of potassium promotion, three of the catalysts (Fe- $LaTiO_{3-\delta}$, Fe-$La_{0.90}K_{0.10}TiO_{3-\delta}$ and Fe-$La_{0.80}K_{0.20}TiO_{3-\delta}$) were subjected to further analysis using *in situ* X-ray diffraction. This approach allowed for the characterization of the bulk structural changes that occur in the catalysts during reduction and under FT conditions. Experiments were conducted using an in-house designed *in situ* capillary XRD cell [186,187]. The catalyst reduction was performed simulating the offline catalyst reduction process (Section 4.4.6 in Chapter 4).

The process of reduction is facilitated by the presence of H_2 converting Fe_3O_4 to wüstite (FeO) and then to metallic Fe (Equation 5.1 and 5.2). On the unpromoted catalyst Fe_3O_4 starts to reduce to FeO at 308 °C (Figure 5.30A). The Fe_3O_4 coexists with the FeO until it is completely converted at 361 °C. The transformation from FeO to metallic Fe is quick and proceeds from 330 °C reaching conclusion at 450 °C (Figure 5.31).

$$Fe_3O_4 + H_2 \longrightarrow 3FeO + H_2O$$ *Equation 5. 1*

$$FeO + H_2 \longrightarrow Fe + H_2O$$ *Equation 5. 2*

The addition of potassium to the catalyst reduces the onset reduction temperature from Fe_3O_4 to FeO (Figure 5.30B & C). On the 10 atom-% K promoted catalyst, it is observed that Fe_3O_4 starts transforming to wüstite at 244 °C. These observations can be attributed to the high dispersion of potassium, hence the lowered reduction temperature. Literature has also attributed the reduced onset temperature in the presence of potassium under H_2 treatment, to the less pronounced interaction between the iron oxide and the support [5,221]. The coexistence of these two phases continues until the complete reduction of Fe_3O_4 at 298 °C. The presence of potassium retards the reduction to metallic Fe. However, it starts forming at 330 °C and the intermediate phase, wüstite, disappears at 446 °C. The transformation to metallic Fe is found to be a slow process, requiring approximately 5 hours after reaching 450 °C to reach completion (Figure 5.31). Similar results have been reported by Ndlela and Shanks [222].

In comparison, with further increasing the potassium content in the catalyst, 20 atom-% K, it is observed that the onset temperature for the reduction step from Fe_3O_4 to FeO is slightly higher, at 266 °C, in comparison to the 10 atom-% promoted catalyst (Figure 5.30C). Fe_3O_4 is fully reduced at 393 °C. The wüstite starts transforming to metallic Fe at 330 °C. The transformation to metallic Fe is even slower in this catalyst compared to the unpromoted and

10 atom-% potassium promoted catalysts. This phase requires approximately 8 hours after reaching 450 °C to reach completion (Figure 5.31). Metallic Fe was the sole identifiable phase after the reduction process. The slightly higher onset temperature can be ascribed to the strong interaction between potassium oxide and iron oxide, which is known to inhibit the adsorption of hydrogen on the catalyst surface, as a result, impede the reduction of iron oxide in the vicinity of the potassium promoter [198,199]. Additionally, Li et al. [193] have demonstrated that addition of potassium retarded the reduction of catalysts due to the strong interaction between potassium oxide and unreduced iron oxides. For conventionally impregnated catalysts, it has been reported that potassium increases the activation energy of the reaction by forming a protective K_2O layer [97,117].

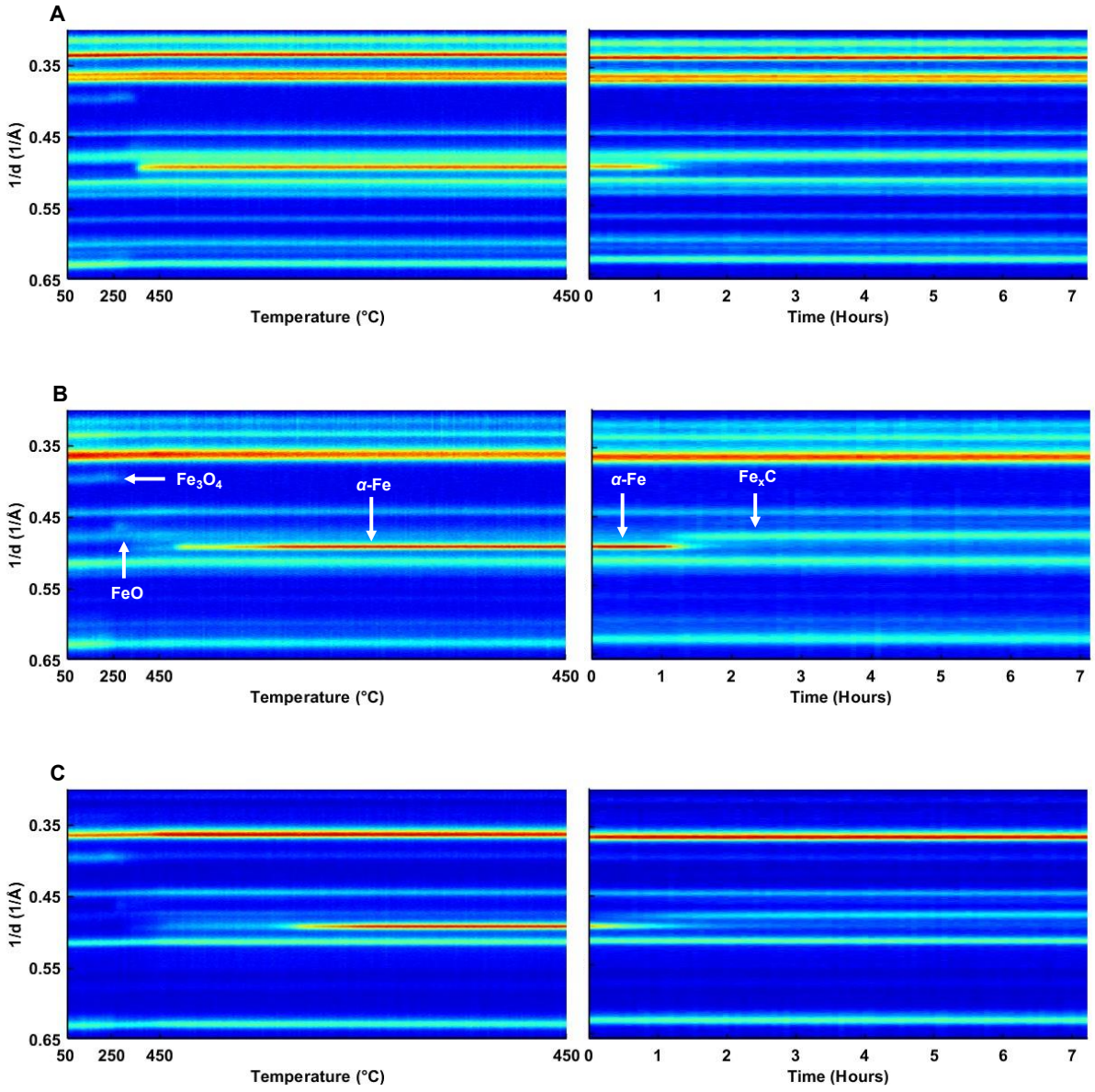

Figure 5. 30: In situ reduction (L) and FT experiment (R) on Fe-$LaTiO_{3-\delta}$ (A), Fe-$La_{0.90}K_{0.10}TiO_{3-\delta}$ (B) and Fe- $La_{0.80}K_{0.20}TiO_{3-\delta}$ (C).

Upon exposure of the reduced catalyst to FT conditions (see Section 4.5.3 in Chapter 4), all catalysts exhibit the transformation of metallic Fe into iron carbide (Figure 5.30A – C). The formation of the carbide is expected under these conditions. Even though potassium promotion retards the reduction to metallic Fe, it enhances the initial formation of carbides through its influence on CO and H_2 chemisorption. Potassium promotion inhibits chemisorption of H_2 onto the iron active phase through charge transfer to the surface, leading to a higher C/H ratio and faster carburization rates [101–104]. On the unpromoted catalyst, metallic Fe starts transforming to iron carbide after about 1 hour of time on stream, and it was fully carburized after 3 hours of TOS. Promotion of the catalyst with 20 atom-% potassium resulted in a sooner onset reduction time, however, the transformation to carbides is slower compared to the unpromoted and 10 atom-% potassium catalysts (Figure 5.31).

After about 1.5 hours of TOS, both the unpromoted and promoted catalysts seem to be equally carburized. These results are in good agreement with previous studies of potassium promoted iron catalysts [97,98,193]. While potassium promotion enhances the CO dissociation, high levels of potassium promotion might result in faster formation of iron carbides, and consequently inhibit CO conversion. This trend is mirrored by the CO conversion results over these catalysts (see Figure 5.29) where it's evident that further increase in potassium promotion has a negative impact on the CO conversion. The *ex-situ* XRD analysis of the spent catalysts are in agreement with these results as we do not see any metallic Fe on the XRD patterns, proof that it had completely carburized.

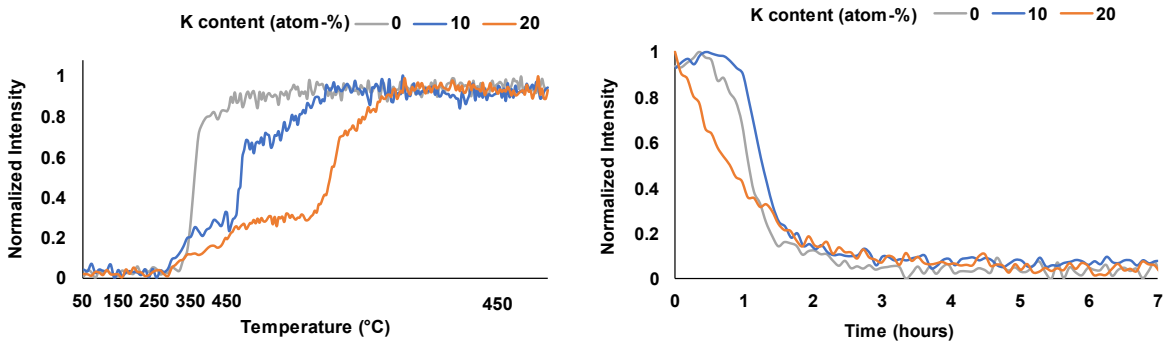

Figure 5. 31: Normalized intensities of the metallic Fe reflexes (0.49 1/Å, 1 1 0) on the reduction (L) and FT synthesis processes (R) on Fe-$La_{1-x}K_xTiO_{3-\delta}$.

In summary, the *in situ* XRD experiments show that the presence of H_2 facilitates the reduction of Fe_3O_4 to metallic Fe through the intermediate phase wüstite, FeO. The reduction temperature of Fe_3O_4 to FeO is lowered in the presence of potassium as a catalyst promoter, and the transformation from FeO to metallic Fe is slower in catalysts with higher potassium

content. The reduction temperature and the transformation rate are influenced by the interaction between potassium oxide and iron oxide. Upon exposure to FT conditions, all catalysts show the transformation of metallic Fe into iron carbide, with the 20 atom-% potassium promoted catalysts showing a faster onset time for the formation of carbides, but slower transformation rate compared to the 10 atom-% potassium promoted and the unpromoted catalysts. However, the degree of carburization levels off at the same time-on-stream.

More CO_2 is formed via the WGS reaction over the promoted catalysts, although no clear trend with promoter concentration could be identified. (Figure 5.32). Within the group of catalysts with an orthorhombic perovskite structure (0, 5 and 10 atom-% K), the WGS activity increases with an increase in potassium loading. Amongst the cubic perovskite structures, the 15 and 20 atom-% K samples display a slightly enhanced WGS activity compared to the unpromoted sample. The CO_2 selectivity of the catalyst with highest potassium content is comparable to the promoted samples based on an orthorhombic perovskite. Overall, CO_2 formation on these catalysts is lower than measured for the lanthanum aluminates.

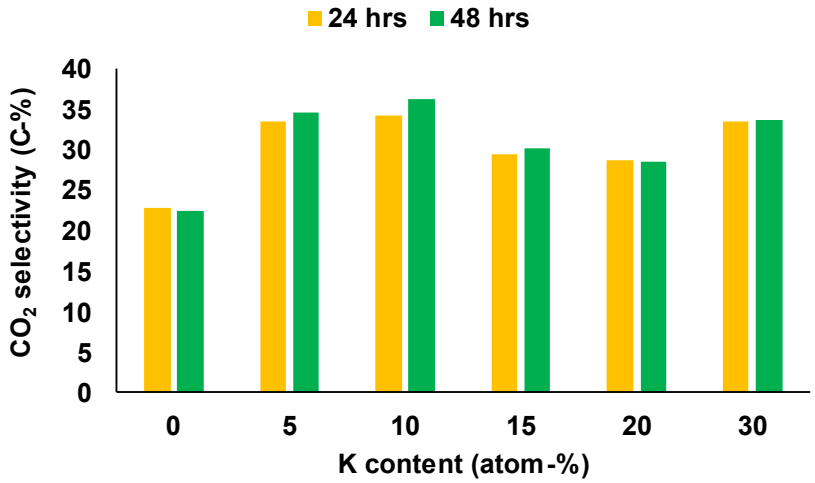

Figure 5. 32: CO_2 selectivity on Fe-$La_{1-x}K_xTiO_{3-\delta}$ catalysts.

Our results are consistent with literature. Several studies on the effect of potassium promotion on iron-based FT have shown an increased CO_2 selectivity on potassium promoted iron catalysts compared to unpromoted references at the same reaction conditions [58,193,223].

The methane selectivity is reduced significantly in the presence of potassium as expected (see Figure 5.33). Even though potassium promotion itself increases the C/H ratio on the catalyst surface through electronic promotion, the methane selectivity changes amongst the promoted

samples cannot be explained by the WGS, which inherently increases the H_2/CO ratio This is different to the Fe-$La_{1-x}K_xAl_{0.8}Mn_{0.2}O_{3-\delta}$ samples where, at lower promotion levels, the WGS activity was found to influence the methane selectivity.

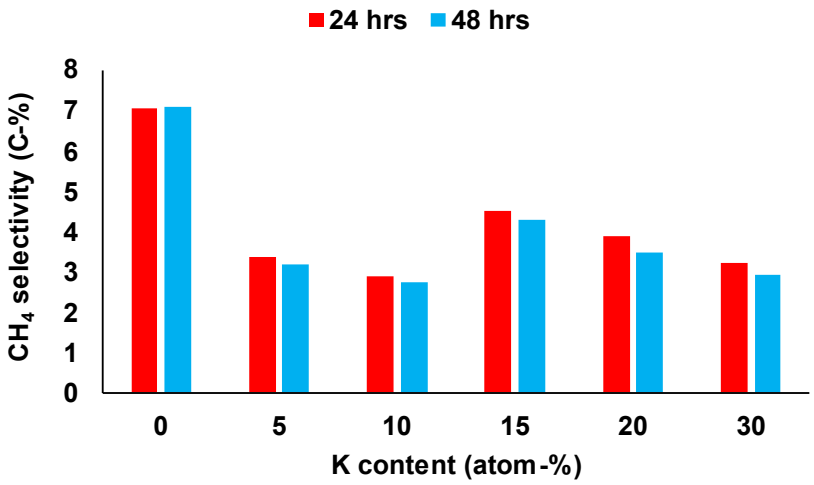

Figure 5. 33: Methane selectivity on Fe-$La_{1-x}K_xTiO_{3-\delta}$.

With increasing levels of potassium promotion, a decrease in the selectivity of C_2 – C_4 hydrocarbons and a slight increase in the selectivity of C_{5+} hydrocarbons is observed. On the unpromoted catalyst the selectivity of the C_2 – C_4 fraction is 22 C-% while that of the C_{5+} hydrocarbons are 44 C-%, slightly higher than the selectivity of the same organic classes in the unpromoted lanthanum aluminates (37 C-%). Potassium promotion results in a shift of the selectivity towards the C_{5+} fraction, while the C_2 – C_4 hydrocarbons decrease. The concentration of potassium has little influence on the degree of change (see Figures 5.34 and 5.35). Compared to the lanthanum aluminate samples, at lower potassium concentration, the selectivity to the short chain hydrocarbons on the titanates is higher and the selectivity to the long chain products is lower.

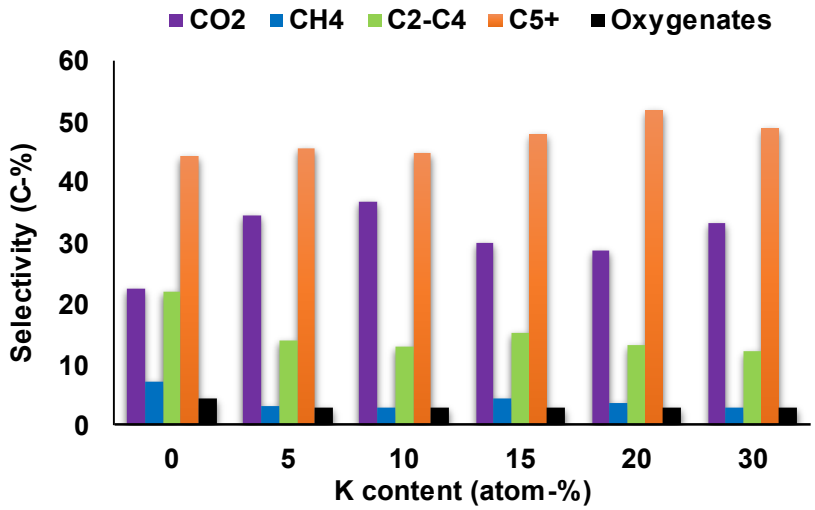

Figure 5. 34: Hydrocarbon selectivity on Fe-$La_{1-x}K_xTiO_{3-\delta}$ catalysts.

To better understand the catalytic performance, eliminating the influence of CO_2, the selectivity towards hydrocarbons was normalized (see Figure 5.35). Although the promoted samples show a decrease in the selectivity of C_2 – C_4 compared to the unpromoted catalyst, within the orthorhombic catalysts, potassium promotion shifts the selectivity towards C_{5+} hydrocarbons, apparently independent of the potassium concentration. This contrasts the effect of potassium promotion in the lanthanum aluminate samples, where the lowest concentration of potassium (2 atom-% K) results in the highest C_{5+} selectivity. If lower potassium concentrations in the titanate perovskites also show preferred chain growth is unknown at this stage. Amongst the cubic structures (15 to 30 atom-% K), increasing the potassium content slightly increases the formation of long-chained products.

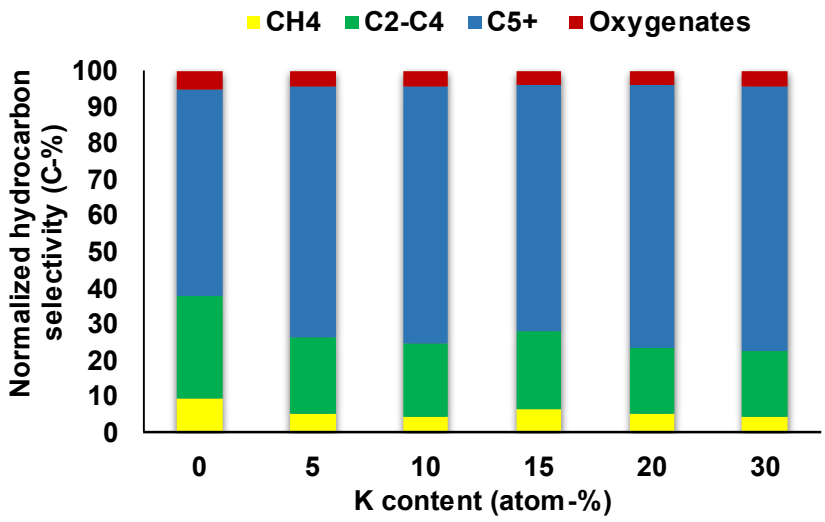

Figure 5. 35: Normalized hydrocarbon selectivity on Fe-$La_{1-x}K_xTiO_{3-\delta}$ catalysts.

In chain growth, CH_x species serve as the building blocks for the formation of hydrocarbon chains. The rate of chain growth is determined by the availability of monomers and the efficiency of the initiation and addition reactions. The presence of potassium as a promoter shifts the product distribution towards longer chain hydrocarbons and away from shorter chain hydrocarbons such as methane. Table 5.12 summarizes the first chain growth probability (C_3 – C_7) on these catalysts. The results indicate that the addition of potassium to these catalysts has no impact on $\alpha 1$, which remains constant at about 0.60 except for the highest potassium loadings which might show a modest increase. Similar to the lanthanum aluminates, the sample collection and analysis method resulted in the partial condensation of the C_{7+} hydrocarbons in the glass ampoule, preventing the recording of a higher secondary alpha. Our calculations show that the modelled secondary alpha for the C_{7+} fraction is approximately 0.87 on the unpromoted and 0.95 for the potassium promoted catalysts. Figure A.4 in the Appendix shows the ASF plot for $\alpha 1$ linear paraffins and olefins (C_3 – C_7).

Table 5. 12: Chain growth probability of linear hydrocarbons on Fe-$La_{1-x}K_xTiO_{3-\delta}$ catalysts

Catalyst	**α1 linear paraffins and olefins (C_3 – C_7)**
Fe-$LaTiO_{3-\delta}$	0.61
Fe-$La_{0.95}K_{0.05}TiO_{3-\delta}$	0.62
Fe-$La_{0.90}K_{0.10}TiO_{3-\delta}$	0.60
Fe-$La_{0.85}K_{0.15}TiO_{3-\delta}$	0.58
Fe-$La_{0.80}K_{0.20}TiO_{3-\delta}$	0.62
Fe-$La_{0.70}K_{0.30}TiO_{3-\delta}$	0.65

The O/P ratios are elevated in comparison to the unpromoted reference (Figure 5.38). There is no clear trend with increasing potassium loading. Similar to the results in the lanthanum aluminates, the impact of promotion is particularly noticeable in the C_2 fraction.

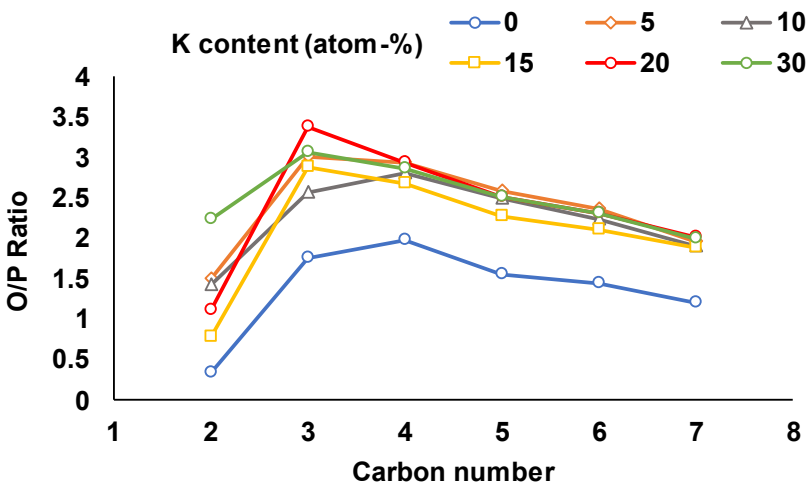

Figure 5. 36: Ratio of Olefins/Paraffins on Fe-$La_{1-x}K_xTiO_{3-\delta}$ catalysts.

The yield of internal olefins is much higher in the unpromoted titanate catalyst compared to the aluminate catalyst discussed earlier (Figure 5.39). K addition suppresses the double bond isomerization effectively. The samples with 15 and 20 atom-% K in the A site of the perovskite still show a significant fraction of internal olefins. This could be a trend amongst the cubic perovskite structures, decreasing isomerization with increasing potassium content, similar to the methane selectivity. However, at this stage the is no evidence for a causal relationship.

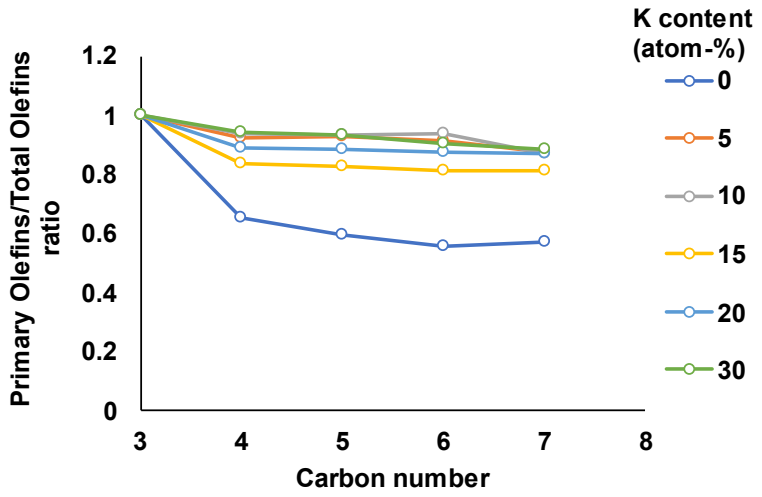

Figure 5. 37: Ratio of Primary Olefins/Total Olefins on Fe-$La_{1-x}K_xTiO_{3-\delta}$ catalysts.

Potassium promotion in the Fe-$La_{1-x}K_xTiO_{3-\delta}$ catalysts has only a little impact on the distribution of the oxygenate products (Figure 5.36), in contrast to the aluminate samples. A decrease in

the aldehyde selectivity for catalysts with higher potassium loading is observed, which is balanced by an increase in alcohol selectivity. The selectivity to ketones in these catalysts is less than 1 C-% of the total oxygenates.

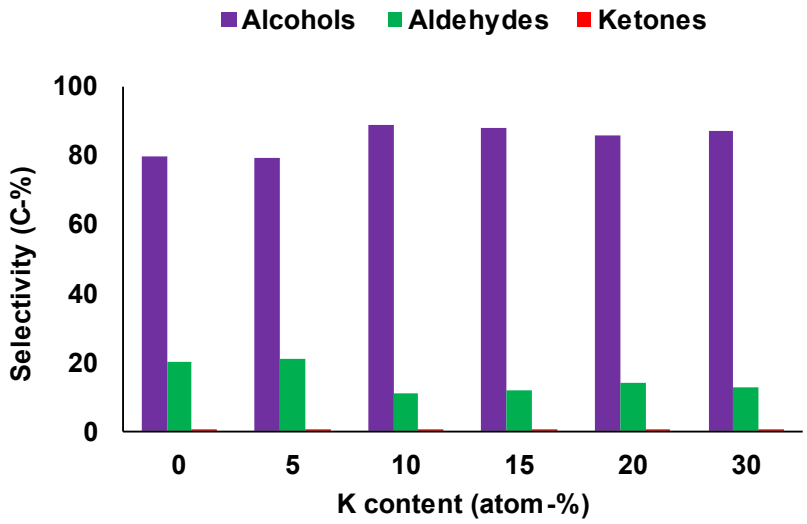

Figure 5. 38: Alcohol, aldehyde, and ketone selectivity within the oxygenate fraction on Fe-$La_{1-x}K_xTiO_{3-\delta}$ catalysts.

A further in-depth analysis of the selectivity of oxygenates as a function of carbon number showed that in the absence of potassium promotion, the major products formed are the C_3 – C_4 oxygenates, followed by C_2 oxygenates and methanol (Figure 5.37). Like the lanthanum aluminates, the addition of potassium reduced the formation of methanol with no clear trend with potassium content.

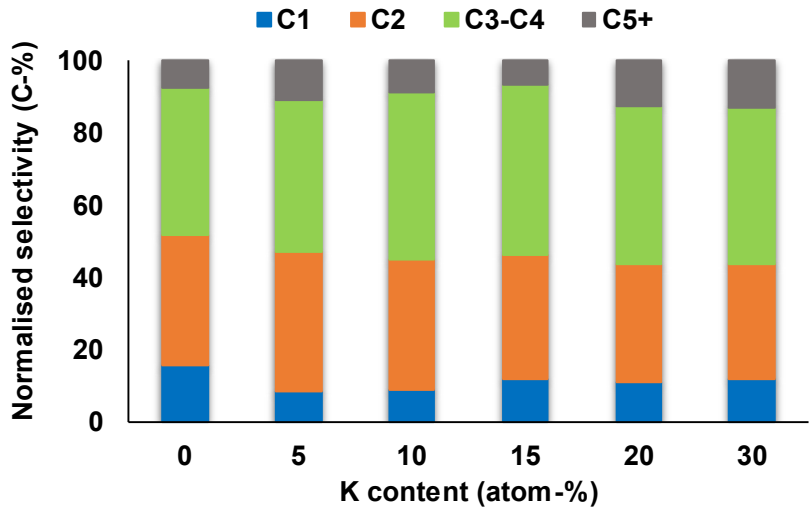

Figure 5. 39: Oxygenates selectivity as a function of carbon number on Fe-$La_{1-x}K_xTiO_{3-\delta}$ catalysts.

On investigating the effect of potassium promotion on iron supported on $La_{1-x}K_xTiO_{3-\delta}$, the results shows that potassium promotion in these catalysts increased the CO conversion from 41 C-% after 48-hours of TOS to a maximum of 54 C-% on the 10 atom-% potassium catalyst. Further addition of potassium decreased activity. The *in situ* XRD results revealed that potassium retards the reduction process and changes the temperatures at which different phases forms. The transformation from the Fe_3O_4 to metallic Fe proceeds quickly, but with addition of potassium, the process was slowed and retarded to higher temperatures. Nevertheless, potassium promotion did speed up the initial formation of carbides. Despite this observation, all potassium bearing samples showed an extended formation period in which the CO conversion increased up to 90-hours of TOS before stabilizing (Figure A.1 in Appendix). XRD could not provide a conclusive explanation of the surface processes influencing this behaviour.

The WGS activity was promoted by the addition of potassium to the catalysts, despite the lack of a clear trend in the effect of amount of potassium loading. On the other hand, methane formation was greatly suppressed. The changes in methane selectivity amongst the different potassium loadings, could not be linked with the WGS activity.

The results indicate that the addition of potassium to these catalysts has no impact on the first chain growth probability, which remains constant at about 60 %, while increasing the modelled chain growth probability for longer chain hydrocarbons. Potassium promotion shifts the selectivity towards C_{5+} hydrocarbons, while suppressing the production of C_2 – C_4 hydrocarbons. Additionally, potassium addition enhances the olefinicity suppressing secondary double bond shift isomerization.

CHAPTER 6: CONCLUSION

The aim of this work was to develop perovskite-based catalyst support materials with both physical properties similar to those of common catalyst supports and the ability to promote catalytic activity. The study focused on lanthanum-based perovskites, $LaAlO_{3-\delta}$ and $LaTiO_{3-\delta}$. The $LaAlO_{3-\delta}$ catalysts were substituted with potassium on the A site and with 20 atom-% Mn on the B site, while the $LaTiO_{3-\delta}$ catalysts were only substituted with K on the A site. Iron oxide nanoparticles were deposited onto these empowered supports to provide the active phase for the FT synthesis. Iron oxide nanoparticles were prepared via the co-precipitation method described by Fadlalla et al. [9]. XRD analysis confirmed the formation of Fe_3O_4 of about 8 nm average crystalline size.

The effect of potassium promotion on the properties and performance was then evaluated. Characterisation techniques including XRD, surface area measurements via N_2 adsorption, TEM, SEM-EDX mapping, ICP-OES, and *in situ* XRD, were used to study the materials as prepared, reduced and after exposure to reaction conditions.

$La_{1-x}K_xAl_{0.8}Mn_{0.2}O_{3-\delta}$, where x = 0, 2, 4, 6, 8, and 10 atom-%, was prepared via the citrate method [7]. XRD and elemental analysis confirmed the successful synthesis of these materials. The potassium substituted materials had a higher BET surface area compared to the material with no potassium. However, this increase does not appear to be linear but rather constant, within the error of the technique. The pore volume mirrors the trend of surface area.

The potassium substituted $La_{1-x}K_xTiO_{3-\delta}$ perovskites for x = 0, 5, 10, 15, 20, and 30 atom-% were prepared via a wet chemical technique [8]. XRD analysis on these perovskites showed a lattice structure transition from orthorhombic to cubic structure with increment in potassium content. BET surface area results of these materials showed an increase in surface area with increase in potassium loading. Notably, within the orthorhombic space group, the increase is small but seems to jump when shifted to cubic.

The prepared Fe_3O_4 nanoparticles were deposited onto the synthesized perovskites supports via a physical mixing procedure targeting a 20 wt.% iron loading [184]. XRD analysis on the reduced materials showed that the Fe_3O_4 phase had transitioned into metallic Fe phase in each of the catalysts.

Potassium promotion of Fe-$La_{1-x}K_xAl_{0.8}Mn_{0.2}O_{3-\delta}$ catalysts resulted in higher FT activities compared to the unpromoted catalyst. There was an increase in catalytic activity with an increase in potassium loading until a maximum of 8 atom.% potassium loading was reached. Potassium promotion is known to improve the CO dissociation adsorption on the Fe surface, which enhances the formation of iron carbides, hence the higher activity on the promoted catalysts [88,90,99,206,207]. The WGS activity increased with potassium promotion as evident by the elevated CO_2 selectivity on the promoted catalysts, increasing with increasing potassium content and reaching a maximum at 8 atom-% potassium. Methane selectivity decreased significantly with potassium promotion. While the differences amongst the potassium bearing catalyst are minor, the observed variations match the observed WGS activity and could therefore be a result of a localized increase in H_2/CO ratio. Similar results are reported by Botes et al. [224], where the authors reported that methane selectivity remained constant for potassium promoted iron catalyst. Incorporation of potassium resulted in a shift in the hydrocarbon product composition from $C_2 – C_4$ towards C_{5+} hydrocarbons. The highest C_{5+} selectivity was recorded for the lowest potassium levels. Furthermore, the O/P ratio was increased, and the double bond shift suppressed, with no clear trend with the amount of potassium

The addition of potassium to $La_{1-x}K_xTiO_{3-\delta}$ affects the reduction process and lowers the onset temperatures for the reduction of Fe_3O_4 to FeO. *In situ* XRD results revealed that while potassium promotion slows the reduction process to metallic Fe, it enhances the initial formation of carbides. This effect was evident by the increase in catalytic activity with potassium promotion until it reached a maximum at 10 atom-% K loading, after which more addition resulted in lower CO conversion. Similar trends have been reported in literature [220,105]. The WGS activity was higher on the K promoted catalysts even though there was no clear trend with the amount of K. Methane formation was suppressed in the presence of potassium. The observed trends in CH_4 selectivity were ascribed to the different lattice structures. Potassium promotion resulted in a decrease in $C_2 – C_4$ selectivity, and an increase in C_{5+} selectivity. The olefinicity was enhanced in promoted catalysts, while suppressing the secondary double bond shift isomerization. The catalysts based on perovskites with a cubic structure produced a significant fraction of internal olefin, decreasing with increasing potassium concentration.

After FT synthesis, the spent catalysts were recovered using the solvent extraction method. n-hexane was used as the solvent and the recovered particles were dried and characterized. XRD analysis on both the Fe-$La_{1-x}K_xAl_{0.8}Mn_{0.2}O_{3-\delta}$ and Fe-$La_{1-x}K_xTiO_{3-\delta}$ spent catalysts showed

the presence of the perovskite structure, iron carbides, and Fe_3O_4. The oxidation is likely the effect of increased activity and therefore increased water partial pressure [203]. Elemental analysis on the spent catalysts using ICP-OES technique confirmed that no K ions leached out of the perovskites during FT synthesis.

In conclusion, our results showed that potassium incorporation into the perovskite structures influences the FT activity and selectivity. We could demonstrate that the promoting effect of potassium extends to the sub 10 atom-% concentration in the $La_{1-x}K_xAl_{0.8}Mn_{0.2}O_{3-\delta}$ samples. Indeed, the lowest potassium concentration did show the greatest enhancement of chain growth although only at a modest increase in conversion. This demonstrates the need for further optimization of compositions to find an optimum in selectivity and conversion. Through the titanate samples, we could show that by replacing the Al^{3+} with titanium cation, which can exist in different oxidation states, a stable perovskite with high potassium concentrations can be synthesized and utilized as catalyst support under reaction conditions. The potassium in the titanate structure acts as promoter in the FT synthesis, however no clear relationship between performance and potassium concentration was discernable. A change in perovskite allotrope, with increasing alkali content, has a potential influence on activity and selectivity trends observed. Further studies are required to manifest this relationship.

CHAPTER 7: RECOMMENDATION AND FUTURE WORK

The effect of potassium as a promoter for iron-based FT has been widely explored in literature. Over the years, researchers have investigated the promotional effect of potassium on perovskites supported iron catalysts. However, the perovskites structures were used as precursors and exsolution facilitators of the iron catalyst integrated into La-based perovskites. This catalyst doping rendered the perovskite structures less stable during reduction. The study presented herein focused on incorporating the potassium promoter into the perovskites structure to restrain its mobility during FT and investigate its promotional effect on the catalytic activity and selectivity of the materials.

Amongst the lanthanum aluminate-based catalyst, the lowest concentration of potassium showed the biggest enhancement of chain growth. While this was paralleled with the lowest enhancement in activity, selectivity control is probably of more importance in an industrial application. Varying the Mn concentration would be of great interest. This has previously only been done with higher Mn concentrations. It was also noted that the results obtained in the present study are not an exact reproduction of the results previously produced on similar samples in our laboratories. The main difference being the synthesis technique and crystallite size of the iron precursor. As the crystallite size can be expected to influence the interaction of empowered support and FT active phase, systemic changes of this interface area should be studied.

Especially for the lanthanum titanate catalysts, more work is required to fully understand the working principles of the catalyst. While the fundamental approach to exchange aluminum with titanium cations in the B site to allow for the stabilization of higher potassium concentrations was successful, the observed extended activation process under FT conditions remains surprising and the applied techniques could not provide an explanation. Most changes in selectivity also died not scale with potassium content which in part could be due to the different perovskite allotrope. A synthesis project aimed at extending the range of potassium promotion (to lower levels) while retaining the allotrope structure would be of great interest.

The use of high surface area perovskite structures prepared through templating techniques could be an avenue for further investigation into the effects of these structures on catalytic activity. Soft-templating techniques involve the use of a template or mold to guide the growth of the material, resulting in the formation of highly porous structures with high surface areas.

These structures have the potential to enhance catalytic activity due to their large number of active sites and increased accessibility for reactant molecules.

An alternative technique for supporting iron oxide nanoparticles, such as impregnation, could be explored to investigate the effect on FT activity of the catalysts. The method of catalyst loading onto the catalyst support can influence the catalytic activity, as it affects the distribution and dispersion of the active phase. It would be of interest to compare the FT activity of catalyst loaded using impregnation to those loaded using the physical mixing procedure.

Due to their demonstrated stability at higher temperatures, these materials may also be suitable for use in other catalytic processes such as the reverse water-gas-shift reaction. The RWGS reaction involves the conversion of CO_2 and H_2O into CO and H_2 and potassium promotions has been discussed in relevant catalyst systems. It would be of interest to investigate the performance of these materials in the RWGS reaction and other conversion reactions to determine their potential utility in this context.

REFERENCES

1. Fischer, F. and Tropsch, H. Process for the production of paraffin-hydrocarbons with more than one Carbon atom. *United States Patent Office* (1930) doi:10.1145/178951.178972.
2. Dry, M. E. & Hoogendoorn, J. C. Technology of the Fischer-Tropsch Process. *Catal. Rev.* **23**, 265–278 (1981).
3. Dry, M. E. FT catalysts. *Stud. Surf. Sci. Catal.* **152**, 533–600 (2004).
4. Jifan, Xiaofan C., Chenghua Z., Jue W., Wensheng D., Yong Y., Yongwang L., L. Alkalis in iron-based Fischer-Tropsch synthesis catalysts: distribution, migration and promotion. *J. Chem. Technol. Biotechnol.* **92**, 1472–1480 (2017).
5. Pendyala, V. R. R., Graham, U. M., Jacobs, G., Hamdeh, H. H. & Davis, B. H. Fischer-Tropsch synthesis: Deactivation as a function of potassium promoter loading for precipitated iron catalyst. *Catal. Letters* **144**, 1704–1716 (2014).
6. Connor, G. P. & Holland, P. L. Coordination chemistry insights into the role of alkali metal promoters in dinitrogen reduction. *Catal. today* **286**, 21–40 (2017).
7. Megha, U., Shijina, K. & Varghese, G. Auto Combustion Method. 87–92 (2014).
8. Bradha, M., Hussain, S., Chakravarty, S., Amarendra, G. & Ashok, A. Synthesis, structure and total conductivity of A-site doped $LaTiO_{3-\delta}$ perovskites. *Journal of Alloys and Compounds* vol. 626 245–251 (2015).
9. Fadlalla, M. I. *et al.* Enhanced oxygenates formation in the Fischer−Tropsch synthesis over Co- and/or Ni-containing Fe alloys: Characterization and 2D gas chromatographic product analysis. *ACS Catal.* **10**, 14661–14677 (2020).
10. Akinbami, O. M., Oke, S. R. & Bodunrin, M. O. The state of renewable energy development in South Africa: An overview. *Alexandria Eng. J.* **60**, 5077–5093 (2021).
11. IEA. Africa Energy Outlook 2019 - Analysis and key findings. A report by the International Energy Agency. 288 (2019).
12. Perner, J. & Bothe, D. *International aspects of a power-to-X roadmap*. (2018).
13. Dieterich, V., Buttler, A., Hanel, A., Spliethoff, H. & Fendt, S. Power-to-liquid via synthesis of methanol, DME or Fischer–Tropsch-fuels: a review. *Energy Environ. Sci.* **13**, 3207–3252 (2020).
14. Züttel, A., Remhof, A., Borgschulte, A. & Friedrichs, O. Hydrogen: The future energy carrier. *Philos. Trans. R. Soc. A Math. Phys. Eng. Sci.* **368**, 3329–3342 (2010).
15. Daza, Y. A. & Kuhn, J. N. CO_2 conversion by reverse water gas shift catalysis: Comparison of catalysts, mechanisms and their consequences for CO_2 conversion to

liquid fuels. *RSC Adv.* **6**, 49675–49691 (2016).

16. Niemantsverdriet, J. W. & van der Kraan, A. M. On the time-dependent behavior of iron catalysts in Fischer-Tropsch synthesis. *J. Catal.* **72**, 385–388 (1981).
17. Lappas, A. & Heracleous, E. *Production of biofuels via Fischer-Tropsch synthesis: Biomass-to-liquids*. *Handbook of Biofuels Production: Processes and Technologies* (Woodhead Publishing Limited, 2011). doi:10.1533/9780857090492.3.493.
18. Schulz, H. Selforganization in Fischer-Tropsch synthesis with iron- and cobalt catalysts. *Catal. Today* **228**, 113–122 (2014).
19. Subramanian, V., Cheng, K. & Wang, Y. *Fundamentally understanding fischer-tropsch synthesis*. *Encyclopedia of Interfacial Chemistry: Surface Science and Electrochemistry* (Elsevier, 2018). doi:10.1016/B978-0-12-409547-2.13530-9.
20. Khasu, M. The Perovskites as New Support Materials for Synthesis Iron Based Fischer-Tropsch Synthesis. (University of Cape Town, 2022).
21. Stranges, A. A History of the Fischer-Tropsch Synthesis in Germany 1926–45. *Stud. Surf. Sci. Catal.* **163**, 1–27 (2007).
22. Bowen, B. H., Irwin, M. W. & Canchi, D. Coal-To-Liquids (CTL) & Fischer-Tropsch Processing (FT). (2007).
23. Sasol. Product Data Sheet: Sasolwax H1. https://sasoldcproducts.blob.core.windows.net/documents/Product Datasheets/472e0e90-c87f_ZA_Sasolwax H1_EN-ZA.pdf (2019).
24. Krylova, A. Y. Products of the Fischer-Tropsch synthesis (A Review). *Solid Fuel Chem.* **48**, 22–35 (2014).
25. Dry, M. E. The Fischer-Tropsch synthesis. *Catal. Sci. Technol.* **1**, 159–255 (1981).
26. van der Laan, G. P. & Beenackers, A. A. C. M. Kinetics and Selectivity of the Fischer – Tropsch Synthesis : A Literature Review Kinetics and Selectivity of the Fischer – Tropsch Synthesis : A Literature. **4940**, 37–41 (2016).
27. James, O., Chowdhury, B., Mesubi, M. & Maity, S. Reflections on the chemistry of the Fischer–Tropsch synthesis. *RSC Adv.* **2**, 7347–7366 (2012).
28. Mahmoudi, H. *et al.* A review of Fischer Tropsch synthesis process, mechanism, surface chemistry and catalyst formulation. *Biofuels Eng.* **2**, 11–31 (2017).
29. Shafer, W. D. *et al.* Fischer-tropsch: Product selectivity-the fingerprint of synthetic fuels. *Catalysts* **9**, (2019).
30. Xu, J., Yang, Y. & Li, Y. W. Fischer-Tropsch synthesis process development: Steps from fundamentals to industrial practices. *Curr. Opin. Chem. Eng.* **2**, 354–362 (2013).
31. Dry, M. E. Present and future applications of the Fischer-Tropsch process. *Appl. Catal. A Gen.* **276**, 1–3 (2004).

32. Davis, B. H. Fischer-Tropsch synthesis: Current mechanism and futuristic needs. *Fuel Process. Technol.* **71**, 157–166 (2001).
33. Claeys, M. & van Steen, E. *Basic studies*. *Studies in Surface Science and Catalysis* vol. 152 (Elsevier B.V., 2004).
34. Mabaso, E. I. Nanosized iron crystallites for Fischer-Tropsch Synthesis. *Univeristy of Cape Town* (2005).
35. Maitlis, P. M., Quyoum, R., Long, H. C. & Turner, M. L. Towards a chemical understanding of the Fischer-Tropsch reaction: Alkene formation. *Appl. Catal. A Gen.* **186**, 363–374 (1999).
36. Anderson, R. B., Shultz, J. F., Hofer, L. J. E. & Storch, H. H. Physical Chemistry of the Fischer-Tropsch Synthesis. *Bulletin 580 Bureau of Mines* 1–25 (1947).
37. Sternberg, H. W. & Wender, I. International Conference on Coordination Chemistry, London 1959. *Chem. Soc.(London) Spec. Publ* **13**, 35 (1959).
38. Pichler, H. & Schulz, H. Recent insights into the synthesis of hydrocarbons from CO and H_2. *Chem. Eng. Technol.* **42**, 1162–1174 (1970).
39. George, R., Andersen, J. M. & Moss, J. R. A comparison of the rates of alkyl migration in the complexes [CpM(CO) 2R] (M = Fe, Ru, Os; Cp = r/5-CsHs). **505**, 131–133 (1995).
40. Anderson, R. B., Friedel, R. A. & Storch, H. H. Fischer-tropsch reaction mechanism involving stepwise growth of carbon chain. *J. Chem. Phys.* **19**, 313–319 (1951).
41. Iglesia, E. Design, synthesis, and use of cobalt-based Fischer-Tropsch synthesis catalysts. *Appl. Catal. A Gen.* **161**, 59–78 (1997).
42. Tau, L. M., Dabbagh, H. A., Chawla, B. & Davis, B. H. Fischer-Tropsch synthesis with an iron catalyst: Incorporation of ethene into higher carbon number alkanes. *Catal. Letters* **7**, 141–149 (1990).
43. M. Claeys, E. van Steen, F. Roessner, A. R. A process for the production of hydrocarbons including olefins from synthesis gas. (2009).
44. Claeys, M. & Schulz, H. Effects of internal mass transfer on activity and selectivity in iron based Fischer-Tropsch synthesis. *Prepr. Chem. Soc. Div. Pet. Chem.* **49**, 195–199 (2004).
45. Tau, L. M., Robinson, R., Ross, R. D. & Davis, B. H. Oxygenates formed from ethanol during Fischer-Tropsch synthesis. *J. Catal.* **105**, 335–341 (1987).
46. Dry, M. E. Catalytic aspects of industrial Fischer-Tropsch synthesis. *J. Mol. Catal.* **17**, 133–144 (1982).
47. Weber, D. *et al.* Recent advances in the mitigation of the catalyst deactivation of co2 hydrogenation to light olefins. *Catalysts* **11**, (2021).
48. Kuipers, E. W., Vinkenburg, I. H. & Oosterbeek, H. Chain Length Dependence of α-

Olefin Readsorption in Fischer-Tropsch Synthesis. *J. Catal.* **152**, 137–146 (1995).

49. Wojciechowski, B. W. The Kinetics of the Fischer-Tropsch Synthesis. *Catal. Rev.* **30**, 629–702 (1988).
50. Sarup, B. & Wojciechowski, B. W. Studies of the Fischer-Tropsch synthesis on a cobalt catalyst i. evaluation of product distribution parameters from experimental data. *Can. J. Chem. Eng.* **66**, 831–842 (1988).
51. Novak, S., Madon, R. J. & Suhl, H. Secondary effects in the Fischer-Tropsch synthesis. *J. Catal.* **77**, 141–151 (1982).
52. Komaya, T. & Bell, A. T. Estimates of rate coefficients for elementary processes occurring during Fischer-Tropsch synthesis over RuTiO2. *J. Catal.* **146**, 237–248 (1994).
53. Jordan, D. S. & Bell, A. T. Influence of ethylene on the hydrogenation of CO over ruthenium. *J. Phys. Chem.* **90**, 4797–4805 (1986).
54. Iglesia, E., Reyes, S. C. & Madon, R. J. Transport-enhanced α-olefin readsorption pathways in Ru-catalyzed hydrocarbon synthesis. *J. Catal.* **129**, 238–256 (1991).
55. Glebov, L. S. & Kliger, G. A. The molecular weight distribution of the products of the Fischer-Tropsch synthesis. *Russ. Chem. Rev.* **63**, 185–195 (1994).
56. Iglesia, E., Reyes, S. C., Madon, R. J. & Soled, S. L. Selectivity Control and Catalyst Design in the Fischer-Tropsch Synthesis: Sites, Pellets, and Reactors. *Adv. Catal.* **39**, 221–302 (1993).
57. Huff, G. A. & Satterfield, C. N. Evidence for two chain growth probabilities on iron catalysts in the Fischer-Tropsch synthesis. *J. Catal.* **85**, 370–379 (1984).
58. Dictor, R. A. & Bell, A. T. Fischer-Tropsch synthesis over reduced and unreduced iron oxide catalysts. *J. Catal.* **97**, 121–136 (1986).
59. Madon, R. J., Reyes, S. C. & Iglesia, E. Primary and secondary reaction pathways in ruthenium-catalyzed hydrocarbon synthesis. *J. Phys. Chem.* **95**, 7795–7804 (1991).
60. Schulz, H. & Claeys, M. Kinetic modelling of Fischer-Tropsch product distributions. *Appl. Catal. A Gen.* **186**, 91–107 (1999).
61. Todić, B., Ordomsky, V. V., Nikačević, N. M., Khodakov, A. Y. & Bukur, D. B. Opportunities for intensification of Fischer-Tropsch synthesis through reduced formation of methane over cobalt catalysts in microreactors. *Catal. Sci. Technol.* **5**, 1400–1411 (2015).
62. Bendale, Prakash., Anand, P. *Comparison of slurry versus fixed-bed reactor costs for indirect liquefaction applications*. (1991).
63. Hawkins., B. G. *Process Engineering Guide : Reactor and Catalyst Design Choice of Support*.

64. Avci, A. K. & önsan, Z. I. *Catalysts*. *Comprehensive Energy Systems* vols 2–5 (2018).
65. National Energy Technology Laboratory. Fischer-Tropsch synthesis. https://netl.doe.gov/.
66. Andre Steynberg, M. D. *Fischer-Tropsch Technology*. (2004).
67. Henrici-Olive, G. *et al.* Methanol from CO + H_2. in *The Chemistry of the Catalyzed Hydrogenation of Carbon Monoxide* (1984).
68. Lappas, A. & Heracleous, E. Production of biofuels via Fischer–Tropsch synthesis: Biomass-to-liquids. in 549–593 (Woodhead Publishing, 2016). doi:https://doi.org/10.1016/B978-0-08-100455-5.00018-7.
69. Iglesia, E., Reyes, S. C., Madon, R. J. & Soled, S. L. Selectivity control and catalyst design in the Fischer-Tropsch synthesis: sites, pellets, and reactors. in *Advances in catalysis* vol. 39 221–302 (Elsevier, 1993).
70. Jacobs, G. *et al.* Fischer–Tropsch synthesis: support, loading, and promoter effects on the reducibility of cobalt catalysts. *Appl. Catal. A Gen.* **233**, 263–281 (2002).
71. Sie, S. T., Senden, M. M. G. & Van Wechem, H. M. H. Conversion of natural gas to transportation fuels via the shell middle distillate synthesis process (SMDS). *Catal. Today* **8**, 371–394 (1991).
72. Selvatico, D., Lanzini, A. & Santarelli, M. Low Temperature Fischer-Tropsch fuels from syngas: Kinetic modeling and process simulation of different plant configurations. *Fuel* **186**, 544–560 (2016).
73. Steynberg, A. P., Dry, M. E., Davis, B. H. & Breman, B. B. *Fischer-Tropsch reactors*. *Studies in Surface Science and Catalysis* vol. 152 (2004).
74. Saeidi, S. *et al.* Recent advances in reactors for low-temperature Fischer-Tropsch synthesis: Process intensification perspective. *Rev. Chem. Eng.* **31**, 209–238 (2015).
75. Bandara, J. C., Thapa, R., Nielsen, H. K., Moldestad, B. M. E. & Eikeland, M. S. Circulating fluidized bed reactors–part 01: analyzing the effect of particle modelling parameters in computational particle fluid dynamic (CPFD) simulation with experimental validation. *Part. Sci. Technol.* **39**, 223–236 (2021).
76. Knowlton, T. M. Fluidized bed reactor design and scale-up. in *Fluidized Bed Technologies for Near-Zero Emission Combustion and Gasification* 481–523 (2013). doi:https://doi.org/10.1533/9780857098801.2.481.
77. Dry, M. E. High quality diesel via the Fischer-Tropsch process - A review. *J. Chem. Technol. Biotechnol.* **77**, 43–50 (2002).
78. Basu, P. Production of synthetic fuels and chemicals from biomass. in *Biomass Gasification, Pyrolysis and Torrefaction: Practical Design and Theory* 415–443 (Elsevier, 2018). doi:10.1016/B978-0-12-812992-0.00012-1.

79. Becker, H., Güttel, R. & Turek, T. Performance of diffusion-optimised Fischer-Tropsch catalyst layers in microchannel reactors at integral operation. *Catal. Sci. Technol.* **9**, 2180–2195 (2019).
80. Almeida, L. C., Sanz, O., D'Olhaberriague, J., Yunes, S. & Montes, M. Microchannel reactor for Fischer-Tropsch synthesis: Adaptation of a commercial unit for testing microchannel blocks. *Fuel* **110**, 171–177 (2013).
81. Botes, F. G. *et al.* Middle distillate fuel production from synthesis gas via the Fischer–Tropsch process. in *Advances in Clean Hydrocarbon Fuel Processing: Science and Technology* 329–362 (2011). doi:https://doi.org/10.1533/9780857093783.4.329.
82. Sikarwar, V. S., Zhao, M., Fennell, P. S., Shah, N. & Anthony, E. J. Progress in biofuel production from gasification. *Prog. Energy Combust. Sci.* **61**, 189–248 (2017).
83. Sinnott, R. & Towler, G. Design of Reactors and Mixers. in *Chemical Engineering Design* 1039–1146 (2020). doi:https://doi.org/10.1016/B978-0-08-102599-4.00015-1.
84. Espinoza, R. L., Steynberg, A. P., Jager, B. & Vosloo, A. C. Low temperature Fischer-Tropsch synthesis from a Sasol perspective. *Appl. Catal. A Gen.* **186**, 13–26 (1999).
85. Avila, P., Montes, M. & Miró, E. E. Monolithic reactors for environmental applications: A review on preparation technologies. *Chem. Eng. J.* **109**, 11–36 (2005).
86. De Smit, E. & Weckhuysen, B. M. The renaissance of iron-based Fischer-Tropsch synthesis: On the multifaceted catalyst deactivation behaviour. *Chem. Soc. Rev.* **37**, 2758–2781 (2008).
87. Nørskov, J. K., Bligaard, T., Rossmeisl, J. & Christensen, C. H. Towards the computational design of solid catalysts. *Nat. Chem.* **1**, 37–46 (2009).
88. Liu, J. X., Wang, P., Xu, W. & Hensen, E. J. M. Particle Size and Crystal Phase Effects in Fischer-Tropsch Catalysts. *Engineering* **3**, 467–476 (2017).
89. Nakhaei Pour, A., Housaindokht, M. R., Irani, M. & Kamali Shahri, S. M. Size-dependent studies of Fischer-Tropsch synthesis on iron based catalyst: New kinetic model. *Fuel* **116**, 787–793 (2014).
90. Mabaso, E. I., van Steen, E. & Claeys, M. Fischer-Tropsch synthesis on supported iron crystallites of different size. *DGMK Tagungsbericht* 93–100 (2006).
91. Park, J. Y. *et al.* Alumina-supported iron oxide nanoparticles as Fischer-Tropsch catalysts: Effect of particle size of iron oxide. *J. Mol. Catal. A Chem.* **323**, 84–90 (2010).
92. Liu, Y., Chen, J. & Zhang, Y. The effect of pore size or iron particle size on formation of light olefins in Fischer–Tropsch synthesis. *RSC Adv.* **5**, (2015).
93. Torres Galvis, H. M. *et al.* Iron particle size effects for direct production of lower olefins from synthesis gas. *J. Am. Chem. Soc.* **134**, 16207–16215 (2012).
94. Xie, J. *et al.* Size and promoter effects on stability of carbon-nanofiber-supported iron-

based Fischer-Tropsch catalysts. *ACS Catal.* **6**, 4017–4024 (2016).

95. Jones, V. K., Neubauer, L. R. & Bartholomew, C. H. Effects of crystallite size and support on the carbon monoxide hydrogenation activity/selectivity properties of iron/carbon. *J. Phys. Chem.* **90**, 4832–4839 (1986).
96. Nakhaei Pour, A., Housaindokht, M. R., Zarkesh, J. & Tayyari, S. F. Studies of carbonaceous species in alkali promoted iron catalysts during Fischer-Tropsch synthesis. *J. Ind. Eng. Chem.* **16**, 1025–1032 (2010).
97. Farias, F. E. M., Neto, R. C. R., Baldanza, M. A. S., Schmal, M. & Fernandes, F. A. N. Effect of K promoter on the structure and catalytic behavior of supported iron-based catalysts in Fischer-Tropsch synthesis. *Brazilian J. Chem. Eng.* **28**, 495–504 (2011).
98. Yang, Y., Xiang, H. W., Xu, Y. Y., Bai, L. & Li, Y. W. Effect of potassium promoter on precipitated iron-manganese catalyst for Fischer-Tropsch synthesis. *Appl. Catal. A Gen.* **266**, 181–194 (2004).
99. Tao, Z. *et al.* Effect of manganese on a potassium-promoted iron-based Fischer-Tropsch synthesis catalyst. *Catal. Letters* **114**, 161–168 (2007).
100. Kölbel, H. Kalium als strucktureller und Energetischer Promotor in Eisenkatalysatoren. in *Actes du Deuxieme Congress International de Catalyse* vol. 2 2075 (Tchnip Paris, 1960).
101. Anderson, R. B., Seligman, B., Shultz, J. F., Kelly, R. & Elliott, M. A. Fischer-Tropsch synthesis. Some important variables of the synthesis of iron catalysts. *Ind. Eng. Chem.* **44**, 391–397 (1952).
102. Arakawa, H. & Bell, A. T. Effects of potassium promotion on the activity and selectivity of iron Fischer-Tropsch catalysts. *Ind. Eng. Chem. Process Des. Dev.* **22**, 97–103 (1983).
103. Benziger, J. & Madix, R. J. The effects of carbon, oxygen, sulfur and potassium adlayers on CO and H2 adsorption on Fe (100). *Surf. Sci.* **94**, 119–153 (1980).
104. Dry, M. E., Shingles, T., Boshoff, L. J. & Oosthuizen, G. J. Heats of chemisorption on promoted iron surfaces and the role of alkali in Fischer-Tropsch synthesis. *J. Catal.* **15**, 190–199 (1969).
105. Lohitharn, N. & Goodwin, J. G. Effect of K promotion of Fe and FeMn Fischer-Tropsch synthesis catalysts: Analysis at the site level using SSITKA. *J. Catal.* **260**, 7–16 (2008).
106. Zhang, C. H. *et al.* Study of an iron-manganese Fischer-Tropsch synthesis catalyst promoted with copper. *J. Catal.* **237**, 405–415 (2006).
107. Li, T. *et al.* Effect of manganese on an iron-based Fischer-Tropsch synthesis catalyst prepared from ferrous sulfate. *Fuel* **86**, 921–928 (2007).
108. Bukur, D. B. *et al.* Binder/Support Effects on the Activity and Selectivity of Iron Catalysts

in the Fischer-Tropsch Synthesis. *Ind. Eng. Chem. Res.* **29**, 1588–1599 (1990).

109. Rofer-DePoorter, C. K. A comprehensive mechanism for the Fischer-Tropsch synthesis. *Chem. Rev.* **81**, 447–474 (1981).
110. Arsalanfar, M., Mirzaei, A. A., Bozorgzadeh, H. R., Samimi, A. & Ghobadi, R. Effect of support and promoter on the catalytic performance and structural properties of the Fe-Co-Mn catalysts for Fischer-Tropsch synthesis. *J. Ind. Eng. Chem.* **20**, 1313–1323 (2014).
111. Torres Galvis, H. M. *et al.* Supported iron nanoparticles as catalysts for sustainable production of lower olefins. *Science (80-.).* **335**, 835–838 (2012).
112. Bukur, D. B. & Sivaraj, C. Supported iron catalysts for slurry phase Fischer–Tropsch synthesis. *Appl. Catal. A Gen.* **231**, 201–214 (2002).
113. Peña, D. *et al.* The Effect of Copper Loading on Iron Carbide Formation and Surface Species in Iron-Based Fischer–Tropsch Synthesis Catalysts. *ChemCatChem* **10**, 1300–1312 (2018).
114. Herranz, T. *et al.* Genesis of iron carbides and their role in the synthesis of hydrocarbons from synthesis gas. *J. Catal.* **243**, 199–211 (2006).
115. Sarkar, A. *et al.* Fischer-Tropsch synthesis: Morphology, phase transformation and particle size growth of nano-scale particles. *Catal. Letters* **117**, 1–17 (2007).
116. O'Brien, R. J., Xu, L., Spicer, R. L. & Davis, B. H. Activation study of precipitated iron Fischer-Tropsch catalysts. *Energy and Fuels* **10**, 921–926 (1996).
117. Bukur, D. B. *et al.* Activation Studies with a Promoted Precipitated Iron Fischer-Tropsch Catalyst. *Ind. Eng. Chem. Res.* **28**, 1130–1140 (1989).
118. Pendyala, V. R. R. *et al.* Fischer-tropsch synthesis: Effect of activation gas after varying Cu promoter loading over K-promoted Fe-based catalyst. *Catal. Letters* **144**, 1624–1635 (2014).
119. Ding, M. *et al.* Study on reduction and carburization behaviors of iron phases for iron-based Fischer–Tropsch synthesis catalyst. *Appl. Energy* **160**, 982–989 (2015).
120. O'Brien, R. J. *et al.* Activity and selectivity of precipitated iron Fischer-Tropsch catalysts. *Catal. Today* **36**, 325–334 (1997).
121. Argyle, M. D. & Bartholomew, C. H. Heterogeneous catalyst deactivation and regeneration: A review. *Catalysts* **5**, 145–269 (2015).
122. Bartholomew, C. H. Mechanisms of catalyst deactivation. *Appl. Catal. A Gen.* **212**, 17–60 (2001).
123. Bukur, D. B., Koranne, M., Lang, X., Rao, K. R. P. M. & Huffman, G. P. Pretreatment effect studies with a precipitated iron Fischer-Tropsch catalyst. *Appl. Catal. A, Gen.* **126**, 85–113 (1995).

124. Gormley, R. J., Zarochak, M. F., Deffenbaugh, P. W. & Rao, K. R. P. M. Effect of initial wax medium on the Fischer-Tropsch slurry reaction. *Appl. Catal. A Gen.* **161**, 263–279 (1997).
125. Jahangiri, H., Bennett, J., Mahjoubi, P., Wilson, K. & Gu, S. A review of advanced catalyst development for Fischer-Tropsch synthesis of hydrocarbons from biomass derived syn-gas. *Catal. Sci. Technol.* **4**, 2210–2229 (2014).
126. Niemantsverdriet, J. W., Van Der Kraan, A. M., Van Dijk, W. L. & Van Der Baan, H. S. Behavior of metallic iron catalysts during Fischer-Tropsch synthesis studied with Mössbauer spectroscopy, X-ray diffraction, carbon content determination, and reaction kinetic measurements. *J. Phys. Chem.* **84**, 3363–3370 (1980).
127. Dai, Y., Lu, P., Cao, Z., Campbell, C. T. & Xia, Y. The physical chemistry and materials science behind sinter-resistant catalysts. *Chem. Soc. Rev.* **47**, 4314–4331 (2018).
128. Karn, F. S., Shultz, J. F., Kelly, R. E. & Anderson, R. B. Studies of the Fischer-Tropsch synthesis. Poisoning of iron catalysts by H2S in synthesis gas. *Preprints* **7**, 43–47 (1962).
129. Wu, B. *et al.* An active iron catalyst containing sulfur for Fischer-Tropsch synthesis. *Fuel* **83**, 205–212 (2004).
130. R.J. MADON, W. F. T. Fischer-Tropsch Synthesis on a Precipitated. **43**, 32–43 (1981).
131. Chaffee, A. L., Campbell, I. A. N. & Valentine, N. Sulfur Poisoning of Fischer-Tropsch Synthesis Catalysts in a Fixed-Bed Reactor. **47**, 253–276 (1989).
132. Voorhoeve, R. J., Johnson, D. W. J., Remeika, J. P. & Gallagher, P. K. Perovskite oxides: materials science in catalysis. *Science* **195**, 827–833 (1977).
133. Carrier, X., Royer, S. & Marceau, E. Synthesis of metal oxide catalysts. in *Metal Oxides in Heterogeneous Catalysis* 43–103 (2018). doi:10.1016/B978-0-12-811631-9.00002-8.
134. Zhao, J. First-principles study of ferroelectricity in oxide superlattices. (University de Bordeaux I, 2015).
135. Francis, A. *ABO3 Type Perovskites*. *Dielectric Materials for Wireless Communication* (2008).
136. Peña, M. A. & Fierro, J. L. G. Chemical structures and performance of perovskite oxides. *Chem. Rev.* **101**, 1981–2017 (2001).
137. Ponce, S., Peña, M. A. & Fierro, J. L. G. Surface properties and catalytic performance in methane combustion of Sr-substituted lanthanum manganites. *Appl. Catal. B Environ.* **24**, 193–205 (2000).
138. Yang, W. *et al.* Activity of perovskite-type mixed oxides for the low-temperature CO oxidation: Evidence of oxygen species participation from the solid. *J. Catal.* **295**, 45–58

(2012).
139. Johnsson, M. & Lemmens, P. Perovskites and thin films - Crystallography and chemistry. *J. Phys. Condens. Matter* **20**, (2008).
140. Cox, E., G. Structural inorganic chemistry. *Nature* (1951).
141. Muller, U. Description of chemical structures. in *Inorganic Structural Chemistry* vol. 2 2–11 (2006).
142. Goodenough, J. B. Jahn-Teller phenomena in solids. *Annu. Rev. Mater. Sci.* **28**, 1–27 (1998).
143. Armiento, R., Kozinsky, B., Hautier, G., Fornari, M. & Ceder, G. High-throughput screening of perovskite alloys for piezoelectric performance and thermodynamic stability. *Phys. Rev. B - Condens. Matter Mater. Phys.* **89**, 1–10 (2014).
144. Rizwan, M. *et al.* A review on perovskite lanthanum aluminate ($LaAlO_3$), its properties and applications. *Mater. Res. Express* **6**, (2019).
145. Shen, J. X., Schleife, A., Janotti, A. & Van De Walle, C. G. Effects of La 5d and 4f states on the electronic and optical properties of $LaAlO_3$. *Phys. Rev. B* **94**, 1–7 (2016).
146. Muñoz, H. J., Korili, S. A. & Gil, A. Progress and Recent Strategies in the Synthesis and Catalytic Applications of Perovskites Based on Lanthanum and Aluminum. *Materials (Basel).* **15**, (2022).
147. Cimino, S., Lisi, L., De Rossi, S., Faticanti, M. & Porta, P. Methane combustion and CO oxidation on $LaAl_{1-x}Mn_xO_3$ perovskite-type oxide solid solutions. *Appl. Catal. B Environ.* **43**, 397–406 (2003).
148. Ma, Y. *et al.* A Novel $LaAlO_3$ Perovskite with Large Surface Area Supported Ni-Based Catalyst for Methane Dry Reforming. *Catal. Letters* **152**, 2993–3003 (2022).
149. Sim, Y., Yang, I., Kwon, D., Ha, J. M. & Jung, J. C. Preparation of $LaAlO_3$ perovskite catalysts by simple solid-state method for oxidative coupling of methane. *Catal. Today* **352**, 134–139 (2020).
150. Silveira, I. S., Ferreira, N. S. & Souza, D. N. Structural, morphological and vibrational properties of $LaAlO_3$ nanocrystals produced by four different methods. *Ceram. Int.* **47**, 27748–27758 (2021).
151. Mozhegorov, A. A. *et al.* Structure and the electronic and magnetic properties of $LaTiO_3$. *Phys. Solid State* **50**, 1795–1798 (2008).
152. Lichtenberg, F., Widmer, D., Bednorz, J. G., Williams, T. & Reller, A. Phase diagram of $LaTiO_x$: from 2D layered ferroelectric insulator to 3D weak ferromagnetic semiconductor. *Zeitschrift für Phys. B Condens. Matter* **82**, 211–216 (1991).
153. Lippmaa, M. Transport properties of embedded $LaTiO_3$ layers. *Nature* (2010).
154. Ohtomo, A., Muller, D. A., Grazul, J. L. & Hwang, H. Y. Epitaxial growth and electronic

structure of $LaTiO_x$ films. *Appl. Phys. Lett.* **80**, 3922–3924 (2002).

155. Scheiderer, P. *et al.* Tailoring Materials for Mottronics: Excess Oxygen Doping of a Prototypical Mott Insulator. *Adv. Mater.* **30**, 1–7 (2018).
156. Ruiz, A. I., Lopez, M. L., Pico, C. & Veiga, M. L. New $La_{2/3}TiO_3$ derivatives: Structure and impedance spectroscopy. *J. Solid State Chem.* **163**, 472–478 (2002).
157. Suvorov, D., Valant, M., Škapin, S. & Kolar, D. Microwave dielectric properties of ceramics with compositions along the $La_{2/3}TiO_3$(STAB)-$LaAlO_3$ tie line. *J. Mater. Sci.* **33**, 85–89 (1998).
158. Kawai, H. & Kuwano, J. Lithium Ion Conductivity of A-Site Deficient Perovskite Solid Solution $La_{0.67-x}Li_{3x}TiO_3$. *J. Electrochem. Soc.* **141**, L78 (1994).
159. Fourquet, J. L., Duroy, H. & Crosnier-Lopez, M. P. Structural and Microstructural Studies of the Series $La_{2/3-x}Li_{3x\square 1/3-2x}TiO_3$. *J. Solid State Chem.* **127**, 283–294 (1996).
160. León, C. *et al.* Non-Arrhenius conductivity in the fast ionic conductor Reconciling spin-lattice and electrical-conductivity relaxations. *Phys. Rev. B* **56**, 5302–5305 (1997).
161. Ruiz, A. I., López, M. L., Veiga, M. L. & Pico, C. Electrical properties of $La_{1.33-x}Li_{3x}Ti_2O_6$ ($0.1<x<0.3$). *Solid State Ionics* **112**, 291–297 (1998).
162. Ruiz, A. I., López, M. L., Veiga, M. L. & Pico, C. Electrical behaviour of $La_{1.33-x}M_{3x}Ti_2O_6$ perovskites (M=Li, Na and K). *Int. J. Inorg. Mater.* **1**, 193–200 (1999).
163. Miao, J.-P. *et al.* Structure characteristics and valence state study for $La_{1-x}K_xTiO_3$ synthesized under high-pressure and high-temperature. *J. Alloys Compd.* **387**, 287–291 (2005).
164. Yamamoto, H., Tahara, T., Sugahara, Y., Kuroda, K. & Kato, C. Synthesis of $La_{1-x}M_xTiO_3$ (M = Na, K; $0 \leq x \leq 0.4$) and the electrical properties. *Phase Transitions* **41**, 137–141 (1993).
165. Roger, A. C. & Kiennemann, A. Perovskites as Catalyst Precursors for Fischer-Tropsch Synthesis. *Perovskites Relat. Mix. Oxides Concepts Appl.* 631–658 (2015) doi:10.1002/9783527686605.ch28.
166. Bedel, L., Roger, A. C., Rehspringer, J. L. & Kiennemann, A. Structure-controlled La-Co-Fe perovskite precursors for higher C_2-C_4 olefins selectivity in Fischer-Tropsch synthesis. in *Natural Gas Conversion VII* (eds. Bao, X. & Xu, Y. B. T.-S. in S. S. and C.) vol. 147 319–324 (Elsevier, 2004).
167. Bedel, L., Roger, A. C., Rehspringer, J. L., Zimmermann, Y. & Kiennemann, A. $La_{(1-y)}Co_{0.4}Fe_{0.6}O_{3-\delta}$ perovskite oxides as catalysts for Fischer-Tropsch synthesis. *J. Catal.* **235**, 279–294 (2005).
168. Escalona, N., Fuentealba, S. & Pecchi, G. Fischer-Tropsch synthesis over $LaFe_{1-x}Co_xO_3$ perovskites from a simulated biosyngas feed. *Appl. Catal. A Gen.* **381**, 253–260

(2010).

169. Liu, G. *et al.* Bi-metal Cu-Co from $LaCo_{1-X}Cu_xO_3$ perovskite supported on zirconia for the synthesis of higher alcohols. *Fuel Process. Technol.* **128**, 289–296 (2014).
170. Liu, G., Niu, T., Pan, D., Liu, F. & Liu, Y. Preparation of bimetal Cu-Co nanoparticles supported on meso-macroporous SiO_2 and their application to higher alcohols synthesis from syngas. *Appl. Catal. A Gen.* **483**, 10–18 (2014).
171. Liu, G. L. *et al.* The deactivation of Cu-Co alloy nanoparticles supported on ZrO_2 for higher alcohols synthesis from syngas. *Fuel* **176**, 1–10 (2016).
172. Goldwasser, M. R. *et al.* Modified iron perovskites as catalysts precursors for the conversion of syngas to low molecular weight alkenes. *J. Mol. Catal. A Chem.* **193**, 227–236 (2003).
173. Utsis, N., Vidruk-Nehemya, R., Landau, M. V. & Herskowitz, M. Novel bifunctional catalysts based on crystalline multi-oxide matrices containing iron ions for CO_2 hydrogenation to liquid fuels and chemicals. *Faraday Discuss.* **188**, 545–563 (2016).
174. Meier, P. F. Preparation of a perovskite-like Fischer-Tropsch catalyst composition for the manufacture of C_2–C_4. *United States - Patent Application Publication* vol. 1 2002–2005 (2004).
175. Reynhout, M. J. Fischer-Tropsch catalyst support and catalyst. (2008).
176. Yuan, Li, J., Zhang, S., Zhang, X., Yin, Z., Liu, Q., C. Low carbon dioxide selectivity Fischer-Tropsch catalyst and preparation method and application. (2014).
177. Yuan, Li, J., Zhang, S., Zhang, X., Yin, Z., Liu, Q., C. Method for preparing liquid hydrocarbons by iron-based Fischer-Tropsch synthesis catalyst system. (2014).
178. Gui, Jiang, R., X. Fischer-Tropsch synthesis method. (2014).
179. Li, Zhang, S., Ni, X., Yin, Z. & Liu, Q., J. Cobalt-based catalyst for synthesizing liquid hydrocarbons and its preparation method and application. (2014).
180. Ni, Zhang, S., Yin, Z., Li, J. & Chen, N., X. High-activity Fischer-Tropsch catalyst and preparation and application of the same. (2014).
181. Ni, Zhang, X., Zhang, S. & Li, J., X. Fischer-Tropsch catalyst and preparation and application of the same. (2014).
182. Pendyala, V. R. R. *et al.* Selectivity control of Cu promoted iron-based Fischer-Tropsch catalyst by tuning the oxidation state of Cu to mimic K. *Appl. Catal. A Gen.* **495**, 45–53 (2015).
183. Sutka, A. & Mezinskis, G. Sol-gel auto-combustion synthesis of spinel-type ferrite nanomaterials. *Front. Mater. Sci.* **6**, 128–141 (2012).
184. Fischer, N., van Steen, E. & Claeys, M. Preparation of supported nano-sized cobalt oxide and fcc cobalt crystallites. *Catal. Today* **171**, 174–179 (2011).

185. Farrauto, R. J. & Hobson, M. C. Catalyst Characterization. in (ed. Meyers, R. A. B. T.-E. of P. S. and T. (Third E.) 501–526 (Academic Press, 2003). doi:https://doi.org/10.1016/B0-12-227410-5/00087-9.
186. Fischer, N., Clapham, B., Feltes, T., van Steen, E. & Claeys, M. Size-dependent phase transformation of catalytically active nanoparticles captured in situ. *Angew. Chemie - Int. Ed.* **53**, 1342–1345 (2014).
187. Fischer, N. & Claeys, M. Phase changes studied under in situ conditions—A novel cell. *Catal. Today* **275**, 149–154 (2016).
188. Sasol. Product Data Sheet: Sasolwax H1. https://sasoldcproducts.blob.core.windows.net/documents/Product Datasheets/472e0e90-c87f_ZA_Sasolwax H1_EN-ZA.pdf (2019).
189. Schulz, H., Böhringer, W., Kohl, C. P., Rahman, N. M. & Will, A. Development and Application of Capillary GC Total Stream Sampling Technique for Gas/Vapour Multicomponent Mixtures. *Ger. Soc. Pet. Coal Chem.* (1984).
190. G. Guiochon, C. L. G. Quantitative analysis by gas chromatography: Response Factors. Determination. Accuracy and Precision. in *Quantitative Gas Chromatography for Laboratory Analyses and On-Line Process Control* vol. 42 587–627 (1988).
191. Kováts, E. Gas-chromatographische Charakterisierung organischer Verbindungen. Teil 1: Retentionsindices aliphatischer Halogenide, Alkohole, Aldehyde und Ketone. *Helv. Chim. Acta* **41**, 1915–1932 (1958).
192. Raje, A. P., O'Brien, R. J. & Davis, B. H. Effect of potassium promotion on iron-based catalysts for Fischer-Tropsch synthesis. *J. Catal.* **180**, 36–43 (1998).
193. Li, S., Krishnamoorthy, S., Li, A., Meitzner, G. D. & Iglesia, E. Promoted iron-based catalysts for the Fischer-Tropsch synthesis: Design, synthesis, site densities, and catalytic properties. *J. Catal.* **206**, 202–217 (2002).
194. Zieliński, J., Zglinicka, I., Znak, L. & Kaszkur, Z. Reduction of Fe_2O_3 with hydrogen. *Appl. Catal. A Gen.* **381**, 191–196 (2010).
195. Abu Tahari, M. N. *et al.* Influence of hydrogen and various carbon monoxide concentrations on reduction behavior of iron oxide at low temperature. *Int. J. Hydrogen Energy* **44**, 20751–20759 (2019).
196. Richard, M. A., Soled, S. L., Fiato, R. A. & DeRites, B. A. The behavior of iron oxides in reducing atmospheres. *Mater. Res. Bull.* **18**, 829–833 (1983).
197. Jozwiak, W. K., Kaczmarek, E., Maniecki, T. P., Ignaczak, W. & Maniukiewicz, W. Reduction behavior of iron oxides in hydrogen and carbon monoxide atmospheres. *Appl. Catal. A Gen.* **326**, 17–27 (2007).
198. Lund, C. R. F. & Dumesic, J. A. Strong oxide-oxide interactions in silica-supported

magnetite catalysts. IV. Catalytic consequences of the interaction in water-gas shift. *J. Catal.* **76**, 93–100 (1982).

199. Rankin, J. L. & Bartholomew, C. H. Effects of potassium and calcination pretreatment on the adsorption and chemical/physical properties of $FeSiO_2$. *J. Catal.* **100**, 533–540 (1986).
200. Herrera, G., Jiménez-Mier, J. & Chavira, E. Layered-structural monoclinic-orthorhombic perovskite $La_2Ti_2O_7$ to orthorhombic $LaTiO_3$ phase transition and their microstructure characterization. *Mater. Charact.* **89**, 13–22 (2014).
201. Shannon, R. D. Revised Effective Ionic Radii and Systematic Studies of Interatomie Distances in Halides and Chaleogenides. *Acta Crystallogr. Sect. A* **10**, (1993).
202. Bian, G., Oonuki, A., Koizumi, N., Nomoto, H. & Yamada, M. Studies with a precipitated iron Fischer-Tropsch catalyst reduced by H_2 or CO. *J. Mol. Catal. A Chem.* **186**, 203–213 (2002).
203. van Steen, E. & Claeys, M. Fischer-Tropsch catalysts for the biomass-to-liquid process. *Chem. Eng. Technol.* **31**, 655–666 (2008).
204. Zhang, C. *et al.* Effects of Cu and K on Co-precipitated FeMn/SiO2 Catalysts for Fischer-Tropsch Synthesis. *Acta Phys. - Chim. Sin.* **22**, 1310–1316 (2006).
205. An, S., Cho, J., Kwon, D. & Jung, J. C. Alkali-added catalysts based on LaAlO3 perovskite for the oxidative coupling of methane. *ChemEngineering* **5**, (2021).
206. Barrios, A. J. *et al.* Identification of efficient promoters and selectivity trends in high temperature Fischer-Tropsch synthesis over supported iron catalysts. *Appl. Catal. B Environ.* **273**, 1–32 (2020).
207. Tian, Z., Wang, C., Yue, J., Zhang, X. & Ma, L. Effect of a potassium promoter on the Fischer-Tropsch synthesis of light olefins over iron carbide catalysts encapsulated in graphene-like carbon. *Catal. Sci. Technol.* **9**, 2728–2741 (2019).
208. Yang, J., Ma, W., Chen, D., Holmen, A. & Davis, B. H. Fischer-Tropsch synthesis: A review of the effect of CO conversion on methane selectivity. *Appl. Catal. A Gen.* **470**, 250–260 (2014).
209. Ma, W. *et al.* Quantitative comparison of iron and cobalt based catalysts for the Fischer-Tropsch synthesis under clean and poisoning conditions. *Catalysis Today* vol. 343 125–136 (2020).
210. Schulz, H., Claeys, M. & Harms, S. Effect of water partial pressure on steady state Fischer-Tropsch activity and selectivity of a promoted cobalt catalyst. *Stud. Surf. Sci. Catal.* **107**, 193–200 (1997).
211. Schulz, H., van Steen, E. & Claeys, M. Selectivity and mechanism of Fischer-Tropsch synthesis with iron and cobalt catalysts. *Stud. Surf. Sci. Catal.* **81**, 455–460 (1994).

212. Erley, W., McBreen, P. H. & Ibach, H. Evidence for CHx surface species after the hydrogenation of CO over an Fe(110) single crystal surface. *J. Catal.* **84**, 229–234 (1983).
213. Steynberg, A. P., Espinoza, R. L., Jager, B. & Vosloo, A. C. High temperature Fischer-Tropsch synthesis in commercial practice. *Appl. Catal. A Gen.* **186**, 41–54 (1999).
214. Graf, B., Schulte, H. & Muhler, M. The formation of methane over iron catalysts applied in Fischer-Tropsch synthesis: A transient and steady state kinetic study. *J. Catal.* **276**, 66–75 (2010).
215. Egiebor, N. O., Cooper, W. C. & Wojciechowski, B. W. Carbon number distribution of fischer — Tropsch CO-hydrogenation products from precipitated iron catalysts. *Can. J. Chem. Eng.* **63**, 826–834 (1985).
216. Gaube, J. & Technologie, C. The Influence of the Promotor $KzCO_3$ in Iron Catalysts. **73**, 68–73 (1985).
217. Shi, B. & Davis, B. H. Fischer-Tropsch synthesis: Evidence for chain initiation by ethene and ethanol for an iron catalyst. *Top. Catal.* **26**, 157–161 (2003).
218. Shi, B., Wu, L., Liao, Y., Jin, C. & Montavon, A. Explanations of the formation of branched hydrocarbons during fischer-tropsch synthesis by alkylidene mechanism. *Top. Catal.* **57**, 451–459 (2014).
219. Masuku, C. M., Hildebrandt, D., Glasser, D. & Davis, B. H. Steady-state attainment period for fischer-tropsch products. *Top. Catal.* **57**, 582–587 (2014).
220. Ma, W., Jacobs, G., Graham, U. M. & Davis, B. H. Fischer-tropsch synthesis: Effect of K loading on the water-gas shift reaction and liquid hydrocarbon formation rate over precipitated iron catalysts. *Top. Catal.* **57**, 561–571 (2014).
221. Lin, H.-Y., Chen, Y.-W. & Li, C. The mechanism of reduction of iron oxide by hydrogen. *Thermochim. Acta* **400**, 61–67 (2003).
222. Ndlela, S. C. & Shanks, B. H. Reduction behavior of potassium-promoted iron oxide under mixed steam/hydrogen atmospheres. *Ind. Eng. Chem. Res.* **45**, 7427–7434 (2006).
223. Donnelly, T. J. & Satterfield, C. N. Product distributions of the Fischer-Tropsch synthesis on precipitated iron catalysts. *Appl. Catal.* **52**, 93–114 (1989).
224. Botes, F. G., Niemantsverdriet, J. W. & Van De Loosdrecht, J. A comparison of cobalt and iron based slurry phase Fischer-Tropsch synthesis. *Catal. Today* **215**, 112–120 (2013).
225. Jacobs, G. *et al.* Fischer–Tropsch Synthesis: XANES Spectra of Potassium in Promoted Precipitated Iron Catalysts as a Function of Time On-stream. *Catal. Letters* **147**, 1861–1870 (2017).

226. Bukur, D. B., Mukesh, D. & Pate, S. A. Promoter Effects on Precipitated Iron Catalysts for Fischer-Tropsch Synthesis. *Ind. Eng. Chem. Res.* **29**, 194–204 (1990).

227. Kokuun, R., Sanders, E., Models, K., van Steen, E. & Schulz, H. Kinetic Studies of Fischer-Tropsch Synthesis on Suspended Fe/K Catalyst-Rate Inhibition by CO_2 and H20. *Appl. Catal. A Gen.* **186**, 309–320 (1986).

APPENDIX

Appendix A: GC-TCD

Table A. 1: GC-TCD calibration.

Gas	Conc. %	I1	I2	I3	I4	I5	Average	f(N_2)
N_2	5.56	293.72	293.52	294.00	293.11	292.84	293.47	1.000
H_2	39.31	18339.11	18301.66	18303.96	18314.95	18299.52	18316.47	8.829
CO_2	10.04	670.53	669.86	670.06	670.34	668.96	670.17	1.265
CH_4	15.32	2939.75	2935.57	2935.53	2934.34	2931.21	2935.63	3.630
CO	19.78	1014.26	1015.09	1013.34	1014.88	1011.16	1013.35	0.971

Table A. 2: GC-TCD operating conditions.

Model: Agilent Technologies 7820A

Detector		**Thermal Conductivity Detector (TCD)**	
Detector Temperature		250 °C	
Filament		25 µV	
Column			
Column pressure		2.41 bar	
Reference gas		15 ml/min	
Makeup gas	N_2	3 ml/min	
Flow		14.46 ml/min	
Temperature program		**Hold Time (min)**	**Run Time (min)**
Oven Temperature	70 °C	10	10
Valves			
Heaters	100 °C		
Total time			**10 min**

Appendix B: GC-FID

Table A. 3: GC-FID operation conditions.

Model: GC-Model Varian 3900			
Detector		Flame Ionisation Detector (FID)	
Detector Temperature		280 °C	
Split ratio		7	
Column			
Column pressure		1.72 bar	
Flame gas	H_2	30 ml/min	
Makeup gas	N_2	25 ml/min	
Air flow		300 ml/min	
Temperature program	Ramp (°C/min)	Step (°C)	Time (min)
	0	-55	1.5
	10	0	8
	5	100	29
	2	120	40
	5	180	54
	5	200	61
	10	240	70
	20	310	83.5
Total time			83.5 min
Coolant			Liquid CO_2

Appendix C: Catalyst characterization

Iron Oxide nanoparticles

Calculation of the specific surface area, $S_{BET,}$ of the iron oxide nanoparticles:

$$\text{Specific surface area} = \frac{Area}{Volume \times Density}$$

$$\text{Area of a sphere} = 4.\pi.r^2$$

$$\text{Volume of a sphere} = \frac{4}{3}.\pi.r^3$$

$$\text{Specific surface area} = \frac{4.\pi.r^2}{\frac{4}{3}.\pi.r^3 \times Density}$$

Table A. 4: Specific surface area of the Fe_3O_4 nanoparticles.

BET surface area of the iron oxide nanoparticles	
Crystalline size (diameter) nm	7.67
Crystalline size (radius) nm	3.84
Crystalline size (radius) m	3.84E-09
Area (m^2)	1.85E-16
Volume (m^3)	2.36E-25
SA (m^2/g)	151
S_{BET} (m^2/g)	174

Table A. 5: Calculated maximum BET surface area of the supported $La_{1-x}K_{0x}Al_{0.8}Mn_{0.2}O_{3-\delta}$ catalysts

Catalyst	Catalyst loading (wt-%)	Maximum BET surface area (m^2/g)
Fe-$LaAl_{0.8}Mn_{0.2}O_{3-\delta}$	11	31
Fe-$La_{0.98}K_{0.02}Al_{0.8}Mn_{0.2}O_{3-\delta}$	13	47
Fe-$La_{0.96}K_{0.04}Al_{0.8}Mn_{0.2}O_{3-\delta}$	12	49
Fe-$La_{0.94}K_{0.06}Al_{0.8}Mn_{0.2}O_{3-\delta}$	14	56
Fe-$La_{0.92}K_{0.08}Al_{0.8}Mn_{0.2}O_{3-\delta}$	11	46
Fe-$La_{0.90}K_{0.10}Al_{0.8}Mn_{0.2}O_{3-\delta}$	12	47

$La_{1-x}K_xAl_{0.8}Mn_{0.2}O_{3-\delta}$ perovskites

Table A. 6: Comparison of La/K ratios in the fresh and spent Fe-$La_{1-x}K_xAl_{0.8}Mn_{0.2}O_{3-\delta}$ catalysts.

	Fresh catalyst		Spent catalyst	
Sample	La	K	La	K
Fe-$LaAl_{0.8}Mn_{0.2}O_{3-\delta}$	0.99	0.01	0.99	0.01
Fe-$La_{0.98}K_{0.02}Al_{0.8}Mn_{0.2}O_{3-\delta}$	0.97	0.03	0.98	0.02
Fe-$La_{0.96}K_{0.04}$ $Al_{0.8}Mn_{0.2}O_{3-\delta}$	0.96	0.04	0.97	0.03
Fe-$La_{0.94}K_{0.06}Al_{0.8}Mn_{0.2}O_{3-\delta}$	0.94	0.06	0.96	0.04
Fe-$La_{0.92}K_{0.08}Al_{0.8}Mn_{0.2}O_{3-\delta}$	0.92	0.08	0.95	0.05
Fe-$La_{0.9}K_{0.1}Al_{0.8}Mn_{0.2}O_{3-\delta}$	0.90	0.10	0.92	0.08

$La_{1-x}K_xTiO_{3-\delta}$ perovskites

Table A. 7: Comparison of La/K ratios in the fresh and spent Fe- $La_{1-x}K_xTiO_{3-\delta}$ catalysts.

Sample	Fresh catalyst		Spent catalyst	
	La	K	La	K
Fe-$LaTiO_{3-\delta}$	1.00	0.00	1.00	0.00
Fe-$La_{0.95}K_{0.05}TiO_{3-\delta}$	0.94	0.04	0.94	0.03
Fe-$La_{0.90}K_{0.10}TiO_{3-\delta}$	0.88	0.08	0.89	0.07
Fe-$La_{0.85}K_{0.15}TiO_{3-\delta}$	0.83	0.12	0.83	0.09
Fe-$La_{0.80}K_{0.20}TiO_{3-\delta}$	0.78	0.17	0.78	0.14
Fe-$La_{0.70}K_{0.30}TiO_{3-\delta}$	0.67	0.32	0.68	0.24

Appendix D: FT activity and product selectivity

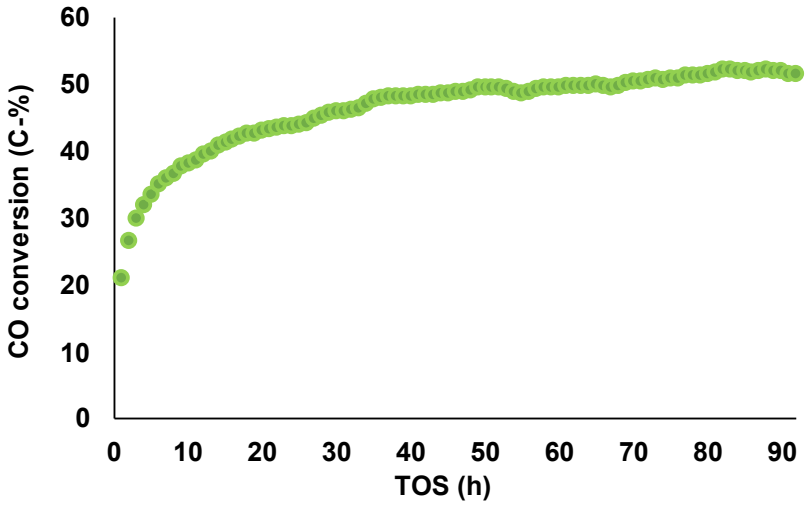

Figure A. 1: CO conversion on Fe-$La_{0.85}K_{0.15}TiO_{3-\delta}$ catalyst as a function of time on stream.

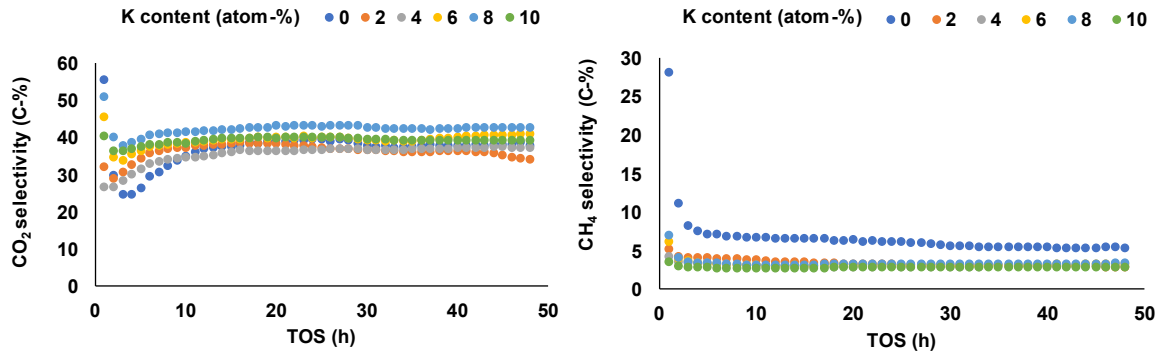

Figure A. 2: CO_2 and methane selectivity on Fe-$La_{1-x}K_xAl_{0.8}Mn_{0.2}O_{3-\delta}$ catalysts as function of time on stream.

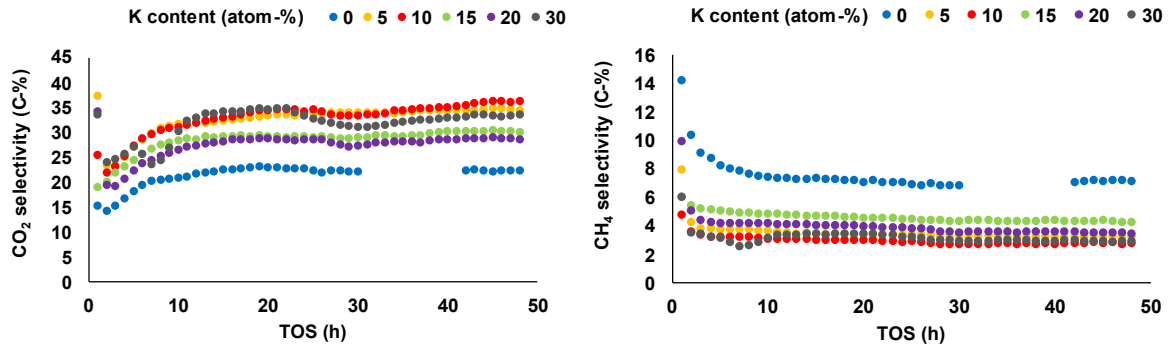

Figure A. 3: CO_2 and methane selectivity on Fe-$La_{1-x}K_xTiO_{3-\delta}$ catalysts as function of time on stream.

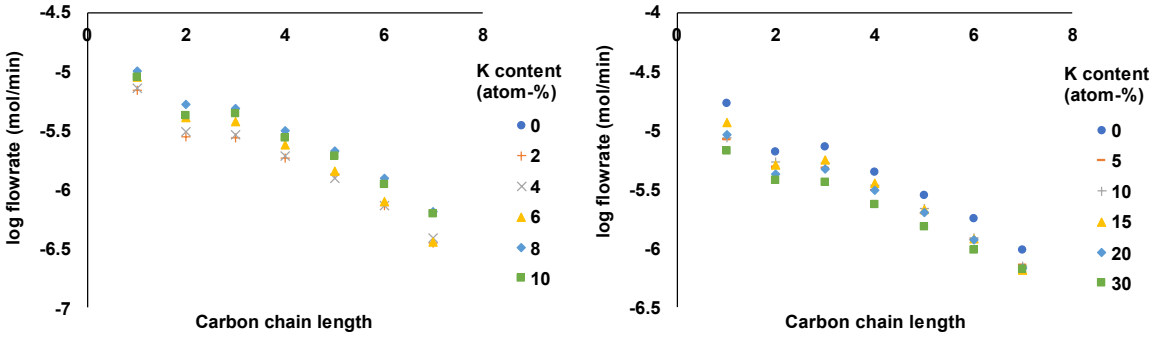

Figure A. 4: ASF plots for Fe-$La_{1-x}K_xAl_{0.8}Mn_{0.2}O_{3-\delta}$ (L) and Fe- $La_{1-x}K_xTiO_{3-\delta}$ catalysts (R).